UNIVERSITÉ DE FRIBOURG SUISSE
UNIVERSITÄT FREIBURG SCHWEIZ

UNIVERSITAS
FRIBURGENSIS

Département de Physique

Université de Fribourg (Suisse)

L-subshell Coster-Kronig rates of Pd and Xe, electron-induced L_3M double ionization of Pd, and *KMM* RAE of Ca investigated by means of high-resolution x-ray spectroscopy

THÈSE

Présentée à la Faculté des Sciences de l'Université de Fribourg (Suisse)

pour l'obtention du grade de

Doctor rerum naturalium

Wei CAO （曹伟）

de la

Chine

Numéro de la thèse: 1696

Imprimerie Saint-Paul, Fribourg

(2010)

Acceptée par la Faculté des Sciences de l'Université de Fribourg (Suisse) sur la proposition de:

Prof. Dr. Christian Bernhard, Université de Fribourg, Président de Jury,
Prof. Dr. Jean-Claude Dousse, Université de Fribourg, Directeur de thèse,
Prof. Dr. John L. (Iain) Campbell, University of Guelph (Canada), Rapporteur,
Dr. Joanna Hoszowska, Université de Fribourg, Rapporteure.

Fribourg, 25 Novembre 2010

Le Directeur de thèse: Le Doyen:

Prof. Dr. Jean-Claude Dousse   Prof. Dr. Rolf Ingold

Contents

Resumé

La présente thèse de doctorat comprend quatre projets de recherche dans le domaine de la physique des couches atomiques profondes. Les deux premiers projets sont consacrés à la détermination expérimentale des coefficients de Coster-Kronig des sous-couches L pour le palladium et le xénon. Dans le troisième projet, nous avons étudié la double ionisation L_3M d'une cible de palladium bombardée par des électrons. Quant au quatrième projet, il concerne les transitions radiatives Auger KMM du calcium. Les quatre projets ont été réalisées en utilisant la méthode de spectroscopie X de haute résolution.

Partie 1. Détermination des coefficients de Coster-Kronig des sous-couches L du palladium en utilisant la spectroscopie X de haute résolution et le rayonnement synchrotron

Les coefficients de Coster-Kronig (CK) des sous-couches L du palladium ont été déterminés en mesurant en haute résolution les raies X $L\alpha_{1,2}$ ($L_3 - M_{4,5}$) et $L\beta_1$ ($L_2 - M_4$). Les spectres de rayons X L ont été collectés au moyen de spectromètres à cristaux courbés. Pour produire la fluorescence de la cible de palladium, un faisceau de rayonnement synchrotron d'énergie variable a été utilisé. Les coefficients CK ont été déterminés à partir des sauts d'intensité des raies X L apparaissant aux bords d'absorption. Pour déterminer la grandeur des sauts, la variation de l'intensité des raies L en fonction de l'énergie du faisceau de rayonnement synchrotron a été ajustée sur celle des sections efficaces d'absorption. Les intensités des raies X L ont été corrigées au préalable pour tenir compte des effets de corps solide. Ces derniers ont été déterminés en comparant les spectres d'absorption expérimentaux et théoriques. Grâce à la haute-résolution des spectromètres à cristaux utilisés, les coefficients CK partiels $f_{13}^{L_1L_3M}$ ont pu être également déterminés à partir des intensités relatives des transitions satellites résolues $L\alpha M$. Pour les coefficients f_{23}, f_{12} et f_{13}, des valeurs de 0.164 ± 0.033, 0.047 ± 0.001 et 0.730 ± 0.039 ont été trouvées. Pour les coefficients partiels $f_{13}^{L_1L_3M}$ et $f_{13}^{L_1L_3N}$, des résultats de 0.406 ± 0.023 et 0.324 ± 0.032 ont été obtenus.

Ce travail a été publié dans la revue Physical Review A **80**, 012512 (2009).

Partie 2. Réexamen des coefficients de Coster-Kronig des sous-couches L du xénon par spectroscopie X de haute résolution

Les valeurs des coefficients CK des sous-couches L du xénon ont été réexaminées par des mesures de haute résolution des transitions radiatives $L\alpha_{1,2}$ $(L_3 - M_{4,5})$ et $L\beta_1$ $(L_2 - M_4)$. Les mesures ont été réalisées en utilisant un spectromètre à cristal incurvé de type Johansson et des faisceaux monochromatiques de rayonnement synchrotron d'énergie variable. Comme dans le projet précédent, les coefficients CK ont été déduits des sauts d'intensité des rayons X L apparaissant aux bords d'absorption. La dépendance en énergie de l'intensité des raies de fluorescence a été calquée sur celle des sections efficaces de photoabsorption L. Ces dernières ont été obtenues à partir du spectre d'absorption L du xenon, lequel a été préalablement mesuré. Des valeurs de 0.118 ± 0.029, 0.383 ± 0.037 et 0.096 ± 0.016 ont été trouvées pour les coefficients CK f_{23}, f_{13} et f_{12}. Le facteur de fluorescence de la sous-couche L_1 a également été déterminé à partir du rapport d'intensité des transitions $L\beta_4$ $(L_1 - M_2)$ et $L\beta_1$ $(L_2 - M_4)$. Ces transitions, très proches en énergie, ont pu être résolues grâce à la haute résolution du spectromètre à cristal. Une valeur de 0.059 ± 0.002 a été obtenue.

Ce travail a été publié dans Physical Review A **81**, 012501 (2010).

Partie 3. Double ionisation L_3M du Pd produite par bombardement d'électrons d'énergie moyenne

Les sections efficaces de double ionisation L_3M induite dans le Pd par bombardement d'électrons ont été déterminées pour des énergies d'électrons comprises entre le seuil de double ionisation et 18 keV. Les sections efficaces ont été déterminées à partir des intensités relatives des raies satellites $L\alpha M$ par rapport aux raies diagrammes parentes $L\alpha$. L'échantillon a été bombardé par des électrons monoénergétiques produits par un canon à électrons de 20 kV. Les raies diagrammes et les satellites M ont été mesurés en haute résolution avec un spectromètre à cristal courbé von Hamos. Les sections efficaces partielles TS ont été déterminées en soustrayant les contributions de 'shake' et des transitions CK $L_1 - L_3M_{4,5}$ des sections efficaces totales. Malgré l'utilisation d'une cible épaisse, la variation des sections efficaces TS en fonction de l'énergie des électrons a pu être déterminée grâce à une nouvelle méthode de décomposition virtuelle de la cible en tranches d'épaisseur variable. Nous avons

pu démontrer que la dépendance en énergie des sections efficaces partielles TS était bien reproduite par le modèle semi-empirique de Pattard-Rost.

Ce travail a été soumis récemment à Physical Review A.

Partie 4. Spectres de haute résolution des transitions radiatives Auger KMM du calcium induites par rayonnement synchrotron

Les transitions radiatives Auger (RA) KMM du calcium solide induites par irradiation avec du rayonnement synchrotron ont été mesurées par la méthode de la spectroscopie X de haute résolution avec un spectromètre à cristal courbé von Hamos. Deux énergies différentes d'irradiation ont été utilisées, l'une juste au-dessus du seuil d'ionisation K et l'autre clairement au-delà du bord d'absorption K. L'analyse des données a montré que la structure spectrale et l'intensité relative des transitions RA KMM par rapport à la raie diagramme $K\beta_{1,3}$ $(K - M_{3,2})$ ne dépendaient pas de l'énergie du rayonnement synchrotron. La structure RA observée ressemble à la densité des états externes s, p et d inoccupés. Toutefois, à cause d'effets de corps solide, les transitions RA associées aux processus de 'shakeup' n'ont pas pu être mises en évidence. Une valeur de 0.053(3) a été trouvée pour l'intensité relative totale des transitions RA KMM par rapport à l'intensité de la raie diagramme $K\beta_{1,3}$. Le résultat obtenu est comparé aux prévisions théoriques existantes ainsi qu'à des valeurs expérimentales déterminées en utilisant divers types de projectiles pour l'excitation de la cible.

Ce dernier travail sera soumis prochainement à Physical Review A.

Abstract

The present Ph.D. thesis includes four research projects related to the field of inner-shell atomic physics. The first two are devoted to the experimental determination the L-subshell Coster-Kronig yields of xenon and palladium. In the third one, the electron induced two-step L_3M double ionization cross sections for Pd were investigated. The fourth project concerns the photon induced KMM radiative Auger x-ray transitions of calcium. For all projects the high-resolution emission x-ray spectroscopy technique was employed.

Part 1. L-subshell Coster-Kronig yields of palladium determined via synchrotron-radiation-based high-resolution x-ray spectroscopy

The experimental determination of the palladium L-subshell Coster-Kronig (CK) transition yields via high-resolution measurements of the $L\alpha_{1,2}$ ($L_3-M_{4,5}$) and $L\beta_1$ (L_2-M_4) x-ray emission lines is presented. The L x-ray spectra were recorded by means of curved crystal spectrometers employing energy-tunable synchrotron radiation for fluorescence production. The CK yields were derived from the relative L x-ray intensity jumps at the L-edges by fitting the fluorescence intensities as a function of the photon energy to the photoionization cross sections. The L x-ray intensities were corrected for solid-state effects which were estimated from the comparison of the measured and theoretical Pd L-edge x-ray absorption spectrum. Thanks to high-resolution, the partial CK yield $f_{13}^{L_1L_3M}$ could be extracted from the intensities of the resolved $L\alpha M$ satellite transitions. For f_{23}, f_{12} and f_{13} CK rates, values of 0.164 ± 0.033, 0.047 ± 0.001 and 0.730 ± 0.039 were found, respectively. For the partial CK yields $f_{13}^{L_1L_3M}$ and $f_{13}^{L_1L_3N}$, results of 0.406 ± 0.023 and 0.324 ± 0.032, respectively, were obtained.

This work was published in Physical Review A **80**, 012512 (2009).

Part 2. Synchrotron-radiation-based determination of Xe L-subshell Coster-Kronig yields: A re-examination via high-resolution x-ray spectroscopy

The xenon L-subshell Coster-Kronig (CK) transition yields were revisited via high-resolution measurements of the $L\alpha_{1,2}$ ($L_3 - M_{4,5}$) and $L\beta_1$ ($L_2 - M_4$) x-ray emission lines. The L x-ray spectra were measured employing a Johansson-type curved crystal spectrometer

and energy-tunable synchrotron radiation. The CK yields were derived from the relative L x-ray intensity jumps at the L edges by fitting the fluorescence intensities as a function of the photon energy to the L-subshell photoionization cross sections. The latter were obtained from the measured L-edge photoabsorption spectrum. Values of 0.118 ± 0.029, 0.383 ± 0.037 and 0.096 ± 0.016 were found for the f_{23}, f_{13} and f_{12} CK yields, respectively. Thanks to high resolution, the L_1 fluorescence yield of 0.059 ± 0.002 was also determined from intensity ratios of the well resolved $L\beta_4$ $(L_1 - M_2)$ and $L\beta_1$ $(L_2 - M_4)$ lines.

This work was published in Physical Review A **81**, 012501 (2010).

Part 3. Double L_3M ionization of Pd induced by impact with medium-energy electrons

The electron-induced L_3M two-step double ionization cross sections of metallic Pd were determined experimentally for incident electron beam energies ranging from the double ionization threshold up to 18 keV. The double L_3M ionization cross sections were derived from the intensity ratios $(I_{L\alpha M} : I_{L\alpha})$ of the resolved M-satellites to the parent diagram lines. The sample was bombarded with monoenergetic electrons from an energy tunable 20 kV electron gun. The diagram and M satellite x-ray lines were measured by means of high-resolution x-ray spectroscopy, using a reflection-type von Hamos bent crystal spectrometer. The two-step partial cross sections were determined by subtracting from the measured total double ionization cross sections the contributions due to the shake process and $L_1 - L_3M_{4,5}$ Coster-Kronig transitions. Despite the thick target employed in the present study, the dependence of the two-step cross sections on the incoming electron energy could be derived using a novel target slice decomposition method. It is shown that the obtained energy dependence can be well reproduced by the semiempirical parametrization model of Pattard-Rost.

This work was submitted to Physical Review A.

Part 4. High-resolution KMM radiative Auger spectra of calcium induced by synchrotron radiation

The KMM radiative Auger (RA) x-ray spectra of solid Ca were induced by monochromatic synchrotron radiation and measured with a high-resolution von Hamos spectrometer. Two excitation energies were employed, one in the near K threshold region and the second well above the K absorption edge. The RA spectral structure as well as the KMM RA intensity with respect to the diagram $K\beta_{1,3}$ $(K - M_{3,2})$ line are found to be independent of the excitation energy. The overall RA structure resembles the density of unoccupied outer s-, p- and d- states. Due to solid state effects, however, spectral features resulting from the major discrete shake-up transitions could not be resolved. The obtained total KMM RA yield relative to the $K\beta_{1,3}$ yield of 0.053(3) is compared to theoretical predictions and available experimental data from various types of target excitation.

This work will be submitted to Physical Review A.

Introduction

When W. C. Röntgen discovered x-rays in 1895 [1], he must have expected his exciting observation to cause a stir among the scientific community. However, he probably did not realize how important this new type of radiation would be for basic and applied science. In the years following their discovery, x-rays have indeed played a major role in physics, chemistry, biology, medicine, cristallography and other natural sciences [2]. Furthermore, with the advent in the last two decades of third generation synchrotron radiation (SR) facilities, intense, monochromatic and energy-tunable x-ray beams have become available, which have brought a new boost to the domain. In atomic physics, x-rays are of prime importance to probe the inner- and outer-shell structure of atoms because their wavelengths are of the same order of magnitude as the atomic dimensions.

I. X-RAY ABSORPTION AND EMISSION

When interacting with matter, x-rays can either be absorbed or scattered by the atoms. The photoabsorption leads to an attenuation of the x-ray beam intensity because, as a result of the photoelectric effect, the photons disappear, their whole energy being transferred to bound atomic electrons, named photoelectrons, that are ejected into the contin-

uum. The kinetic energy of the photoelectron is equal to the difference between the energy of the incident photon and the binding energy of the atomic subshell from which the photoelectron originates. Thus, in photoionization the photon vanishes, a photoelectron is emitted and a vacancy state is created in the corresponding atom. If the photon energy is close to but smaller than the binding energy of the electron, the latter cannot escape from the atom, but it can be promoted into an outer incompletely filled level. This process is called photoexcitation.

Scattering processes may occur with or without energy losses of the scattered photons. In the first case, called inelastic scattering, a part of the photon energy is used to promote a bound electron into an outer incompletely occupied bound state or to eject it into the continuum. After an inelastic scattering process, the atom is left in an excited or ionized state and the energy and direction of the scattered photon have changed. In an elastic scattering only the photon direction is modified, the energy of the particle remaining unchanged. Thus, in both the elastic and inelastic scattering processes, there is no photon disappearance. Nevertheless, for collimated x-ray beams, scattering processes result also into a diminution of the incoming x-ray beam intensity because the deflected x-rays are removed from the collimated beam.

The elastic scattering cross sections decrease with growing energy. At low energies they are bigger than the inelastic scattering cross sections, but as the latter increase with the photon energy, both cross sections intersect at given energies that are specific to the elements. For instance, for Al (Z=13) the elastic and inelastic cross sections curves cross at about 25 keV, whereas for Pd (Z=46) the crossing point lies at 85 keV. Above the K-edge, i.e., the binding energy of the K-shell electrons, the photoionization cross sections diminish with the photon energy. For energies below about 100 keV, they are 1-2 orders of magnitude bigger than the scattering cross sections.

The method of measuring the intensity attenuation of a collimated x-ray beam by a given absorbing medium as a function of the energy of the incoming x-rays is called x-ray absorption spectroscopy (XAS). Depending on the energy region of interest, close to the absorption edge or far above it, XAS is usually subdivided into XANES (x-ray absorption near edge structure) and EXAFS (extended x-ray absorption fine structure). The absorption spectra can be also computed within the independent particle approximation model (IPA) using relativistic Hartree-Slater (RHS) calculations. However, these calculations cannot reproduce the oscillations observed in the experimental XANES and EXAFS spectra [3]. A good understanding of these spectral fine structures which are beyond the IPA predictions is, however, mandatory for a correct interpretation of the experimental x-ray absorption spectra and a reliable and precise determination of the photoionization cross sections. Due to the fact that XANES permits to probe both the atomic core levels and the outer unoccupied electron states, unique signatures of a given material can be obtained from this technique. XANES spectra also depend on the detailed atomic structure of the sample as well as on the electronic and vibrational properties of the latter [4]. EXAFS is commonly understood in terms of high-order multiple-scattering processes. Based on the Fermi's 'golden rule' and the electric dipole transition approximation, an unified theory for XANES and EXAFS was elaborated which is based on the 'standard quasi-particle theory' [5, 6].

Within the independent electron picture, a single-photon absorption accompanied by the simultaneous ejection of several bound electrons cannot be explained by photoionization. In the photoeffect, a single photon interacts indeed with a single bound electron. Other indirect effects such as the shakeoff (SO) and knock-out (KO) processes based on electron-electron interactions are thus needed to explain the multiple ionization resulting from single photon impact. In the shake pro-

cess [7], the second electron is ionized due to the sudden change of the effective nuclear charge resulting from the creation via the photoeffect of the first inner-shell vacancy. In the case of KO, the outgoing photoelectron knocks out the second electron, leaving the atom in a doubly-ionized state.

In contrast to photoionization, direct multiple ionization can be produced by impact with charged particles because in this case, several bound electrons of the target atom can feel simultaneously the Coulomb potential of the charged projectile. The direct multiple ionization induced by impact with charged particles is particularly important in the case of heavy ions because the corresponding cross section grows with the squared charge of the incoming projectile. It is worth noting here that the shake process does not depend on the first ionization mechanism. Thus, SO does also exist in particle-induced ionization and its contribution to the multiple ionization is the same as in photoionization. This is, however, not true for the KO process because the momenta of the first ionized electrons are in general smaller in collisions involving charged particles than in the case of photoionization. For instance the contribution of KO to the double K-shell ionization of Al was found to be about 3 times smaller in the case of electron impact than in photoionization, although similar electron and photon beam energies were used [8].

XAS measurements can be performed in the transmission mode or in the fluorescence mode. In the first case, the intensities of the incoming and transmitted x-ray beams are measured simultaneously by two similar detectors, e.g. ionization chambers, as a function of the photon energy. The absorption spectrum can be then obtained in a straightforward way by dividing the measured transmitted intensity by the incoming one. In general, however, for practical reasons, the inverse of the absorption spectrum is preferably determined, i.e., the intensity of the incoming beam is divided by the one of the transmitted beam. Around the K-edge or L-edges, an abrupt increase of the absorption is observed, which is due to the opening of the K-shell or L-subshells photoionization channels. Precise energies for the absorption edges can be obtained by calculating the first derivative of the inverse absorption spectrum, the edge energy corresponding indeed to the energy for which the first derivative is maximum. In the inverse absorption spectrum a strong peak is usually observed just above the K-edge (white line). The latter is due to the presence of unoccupied discrete states close to the Fermi level.

In the fluorescence mode, the fluorescence x-ray emission spectrum of the absorbing sample is measured, using in most cases a

semiconductor detector. Information similar to that provided by the transmission mode can be obtained but there is no restriction on the thickness of the sample. In addition, some features related to inelastic scattering processes are observed in the fluorescence spectra but not in the corresponding absorption spectra. As an alternative to the fluorescence mode, the photoelectron spectrum of the sample can also be measured, provided that very thin samples are employed.

Due to the strong absorption of the incoming beam above the K-edge, the transmitted intensity is very weak. Intense x-ray sources and thin targets are thus needed to get reliable results in XAS measurements performed in the transmission mode. In this respect, the performance of XAS has been drastically improved by using synchrotron radiation as the x-ray source. The improvements concern mainly the precision and reliability of the results and the rapidity of the measurements. For these reasons, XAS has become nowadays a standard technique for the chemical characterization of materials.

The lifetimes of inner-shell vacancies are very small (e.g., 10^{-15}-10^{-17} s, depending on the element, for the K-shell). During these extremely short times, the core-holes are filled by outer shell electrons, bringing the ion to a lower more stable energy state. The energy ΔE released by the electron tran-

sition may lead to the emission of a photon having the energy h$\nu = \Delta$E. As in this process named radiative transition, a photon having an angular momentum of $1\hbar$ is created, the orbital quantum numbers of the two atomic levels involved in the transition should differ by $|\Delta l| = 1$. Radiative transitions satisfying this condition are called electric-dipole (E1) transitions. Electric-quadrupole (E2) and magnetic-dipole (M1) transitions which violate the $|\Delta l| = 1$ selection rule are strongly hindered and the intensities of the corresponding x-rays are therefore very weak. It is interesting to note that the radiative decay corresponds to the time-reversal of the photoexcitation process.

The transition energy ΔE may also be transferred to another bound electron which can then escape from the ion provided that the transition energy is bigger than the binding energy of that electron. This alternative atomic decay mode is called radiationless or Auger transition. Auger transitions are autoionizing transitions since the number of vacancies in the final atomic state is increased by one with respect to the initial state. Thus the creation of an atomic core-level vacancy results into cascades of radiative (fluorescence) and non-radiative (Auger) transitions. As a consequence, one can investigate the atomic relaxation by measuring either the emitted x-rays or the Auger

electrons. The method based on the observation of the x-ray fluorescence is called x-ray fluorescence spectroscopy (XFS) and the one based on the measurement of Auger electrons Auger electron spectroscopy (AES). There is a further atomic decay channel, named radiative-Auger effect (RAE), which is much less probable than the two others but of interest in this thesis (see Part 4). In this exotic decay mode, the transition energy is shared between a photon and an Auger electron which are emitted simultaneously [9, 10].

Diagram x-ray lines correspond to radiative transitions in which there is a single vacancy in the initial and final atomic states. In inner-shell photoionization, however, diagram lines may be accompanied by satellite x-ray lines. The latter result from additional inner-shell vacancies that are present in the atom during the transition but are not directly involved in it. For this reason these additional holes are called spectator vacancies. These holes, although inactive in the transition, reduce the electronic screening of the nuclear charge. As the effect of the screening change decreases with the principal quantum number n, satellite x-ray lines are shifted towards higher energy with respect to their parent diagram lines. As a rule of thumb, one can say that the energy shift of a satellite decreases with the principal quantum number of the shell in which the spectator vacancy is located and increases with the principal quantum number of the shell from which the transition electron originates. For these reasons, energy shifts of M-satellites (spectator vacancy in the M-shell) are smaller than those of L-satellites and energy shifts of satellites of $K\beta$ transitions are bigger than those of $K\alpha$ transitions. However, these energy shifts remain small (a few eV only for light elements), so that high-resolution x-ray detectors are needed to resolve them from their parent diagram lines.

Depending on the specific aims of the measurements, XFS can be performed using energy-dispersive detectors or wavelength-dispersive spectrometers. Energy-dispersive detectors are used preferably when high collection efficiency is needed and a moderate energy resolution is acceptable. With wavelength-dispersive instruments whose working principle is based on the Bragg law [11], more precise energies can be obtained and the resolving power is 10-100 times better but the price to pay is a poor efficiency as compared to energy-dispersive detectors. The poor efficiency of wavelength-dispersive spectrometers is due mainly to their small solid angle. The latter can be improved significantly by using cylindrically or spherically curved crystals but, even in this case, the solid angle remains small (10^{-3}-10^{-4} sr), which leads to longer acquisition times.

Despite this drawback, the use of crystal spectrometers is nevertheless mandatory whenever an energy resolution of a few eV is required.

II.   THE PROJECTS

The present thesis belongs to the domain of atomic inner-shell physics. It is an experimental work which contains four different projects. The first two projects concern the L-subshell Coster-Kronig yields of Pd and Xe, the third one the L_3M double ionization of Pd induced by impact with medium-energy electrons, and the fourth one the KMM radiative Auger effect in Ca. The first two and the fourth projects were carried out using synchrotron radiation for the production of the sample fluorescence, whereas the measurements of the third project were performed at the University of Fribourg using an electron gun. All four projects were carried out by means of high-resolution x-ray spectroscopy, employing either a Johansson (first two projects) or von Hamos (projects 3 and 4) curved crystal spectrometer.

A. L-subshell Coster-Kronig yields of Pd and Xe

L_iL_jX Coster-Kronig (CK) transitions [12] are fast radiationless transitions, in which a vacancy "bubbles up" from the subshell i to the higher subshell j and an Auger electron is ejected from the outer shell X. The transition is energetically allowed only if the difference between the binding energies of the i and j subshells is bigger or equal to the binding energy of the electron in the subshell X. The vacancy transfer probability from the subshell i to the subshell j is called the CK yield f_{ij}. CK yields depend on the initial- and final-state wave functions and are very sensitive to electron binding energies and solid-state effects [13, 14].

In general, L-subshell CK rates vary smoothly with the atomic number Z [15]. Exceptions are observed when the binding energy of the X electron becomes suddenly bigger than the difference between the binding energies of the i- and j-subshells. Particularly interesting is the region around $Z = 48$ where a cutoff of the $L_1 - L_3$ CK rate f_{13} appears due to the closure of the $L_1 - L_3M_{4,5}$ CK transition which becomes abruptly energetically forbidden. The large discrepancies observed between theoretical CK yields [14, 16] and existing experimental values [17, 18] point out the need for new sets of reliable and accurate experimental data. However, the experimental determination of L-shell CK yields presents sizeable difficulties. For this reason, data are scarce and suffer often from large uncertainties [19].

To date, to determine the f_{23} CK yields, mostly the $K\alpha$-$L\alpha$ x-ray coincidence technique [19, 20] was used. The method is based on the fact that a L_3 hole is formed after the emission of a $K\alpha_1$ x-ray ($K - L_3$ transition). This hole can then decay via a $L_3 - M_{4,5}$ transition with the emission of a $L\alpha_{1,2}$ x-ray. Similarly, the decay of a L_2 hole resulting from the emission of a $K\alpha_2$ x-ray ($K - L_2$ transition) may lead to the emission of a $L\alpha_{1,2}$ x-ray provided that the L_2 hole is transferred beforehand to the L_3-subshell by a L_2L_3X CK transition. In this method, the CK rate f_{23} is thus determined by multiplying the ($K\alpha_2 - L\alpha_{1,2}$) to ($K\alpha_1 - L\alpha_{1,2}$) coincidence rate ratio by the known $K\alpha_1$ to $K\alpha_2$ intensity ratio. However, this ingenious method fails in the case of the L_1-subshell CK yields because several transitions (e.g., the $K - L_1$ and $L_1 - M_{4,5}$) that should be measured in coincidence are forbidden by the above-mentioned $|\Delta l| = 1$ selection rule. For this reason, most available experimental data concerning the f_{12} and f_{13} CK yields were obtained from an alternative photoionization method employing $\gamma-$rays from intense radionuclide sources to produce the primary ionization [21].

By combining the advantages of energy-tunable monochromatic SR beams with the XAS and XFS techniques, a subshell-selective photoionization can be achieved which in turn can be used to determine all L-subshell CK yields [22]. By measuring a chosen fluorescence x-ray line at two beam energies tuned just below and just above a given absorption edge, a jump in the intensity of the fluorescence line is observed from which the CK yield can be deduced. For instance, measuring the $L\alpha$ x-ray line at a SR beam energy tuned above the L_3 edge but below the L_2 one, an intensity proportional to the cross section of the L_3-subshell photoionization is found. Now, when the beam energy is tuned above the L_2-edge but below the L_1 one, a step-like increase in the intensity of the $L\alpha$ x-ray line is observed which is due to the fact that part of the photoinduced L_2 holes were transferred to the L_3-subshell by L_2L_3X CK transitions. The excess of intensity found for the fluorescence line with respect to the previous measurement is simply proportional to the L_2-subshell photoionization cross section multiplied by the CK yield f_{23}. Similarly, by tuning the beam energy above the L_1-edge, a new intensity jump is observed from which the f_{13} CK yield can be determined, provided the f_{12} rate is known. The latter, however, can be determined by means of the same method, choosing a L_2 x-ray line such as the $L\beta_1$ ($L_2 - M_4$ transition) and tuning the SR beam energy below and above the L_1 edge.

The above method requires a precise knowledge of the L_i- and L_j- subshell pho-

toionization cross sections. Theoretical values do exist but results from different IPA calculations are found to scatter up to 2% [23]. In addition, due to the hybridization of outer orbitals as a result of solid state effects, for solid samples in the Z region of interest large discrepancies are observed between the IPA predictions and the measured XANES spectra [24]. Furthermore, as for gaseous samples, for which the free atom picture should apply, some oscillations are also observed in the XANES spectra, the discrepancies between experiment and theory cannot be explained entirely by solid state and crystal effects. In fact the observed deviations are not completely understood and different explanations are still under debate [25]. Hence precise measurements of the L-subshell photoionization cross sections were needed in our project.

In principle the fluorescence lines chosen as references for the determination of the CK yields can be measured by means of energy-dispersive detectors. However, as in L x-ray spectra of heavy elements many lines are overlapping, it is preferable to employ high-resolution crystal spectrometers to get reliable results. In addition, high-resolution spectroscopy offers the possibility to resolve the $M-$satellites from their parent diagram lines, which allows, as shown below, to distinguish the $L_1L_3 - M_{4,5}$ CK transitions from the $L_1L_3 - N$ ones.

In these two projects the Coster-Kronig transition yields were determined for metallic Pd ($Z = 46$) and gaseous Xe ($Z = 54$) by means of the above-mentioned synchrotron-radiation-based high-resolution photoionization technique. The measurements were performed at the XAFS beamline of the Italian Synchrotron Radiation Source Elettra, in Trieste, Italy, using the Johansson bent crystal spectrometer of Ljubljana [26]. Complementary measurements were performed later at the European Synchrotron Radiation Facility (ESRF), in Grenoble, France, with the von Hamos curved crystal spectrometer of Fribourg [27].

The x-ray absorption spectra of both samples were measured over energy intervals covering the L-subshell absorption edges and compared to the theoretical spectra obtained from IPA calculations. As discussed before, some significant deviations between the experimental and theoretical XAS spectra were observed. In particular, the XANES oscillations observed in the experimental spectra were not reproduced by the calculations. For this reason, the measured L-subshell photoionization cross sections were employed for the determination of the CK yields. The variation of the photoionization cross section of a given subshell beyond the edge(s) corresponding to the next subshell(s) was deter-

mined by means of power-law extrapolations. For the determination of the parameters entering the power-law functions, the theoretical IPA results were employed. The f_{23} and f_{13} CK yields were derived from the $L\alpha_{1,2}$ ($L_3 - M_{4,5}$) relative intensity jumps at the L edges and the f_{12} CK yield from the $L\beta_1$ ($L_2 - M_4$) intensity jump at the L_1 edge.

Thanks to high-resolution, the $L\alpha M$ satellite of Pd could be separated from its parent diagram line. This allowed us to determine the partial $L_1 - L_3 M_{4,5}$ CK yield from the satellite-to-diagram line yield ratio. For Xe, the fluorescence yield ω_1 of the L_1-subshell could also be determined from the intensity ratio of the resolved $L\beta_4$ ($L_1 - M_2$) and $L\beta_1$ lines, which would not have been possible in low-resolution XRF measurements, the two lines being separated by 30 eV only.

B.   Double L_3M ionization of Pd induced by impact with medium-energy electrons

For Pd, the intensity of the resolved $L\alpha M$ satellite is due mainly to the $L_1 L_3 - M_{4,5}$ CK transition. In fact, this assumption was made in the CK project to determine the partial CK yield $f_{13}^{L_1 L_3 M_{4,5}}$. However, smaller contributions to the satellite intensity may also arise from the SO and KO processes. With the aim of probing the contributions to the M-satellite yield of other double ionization

processes, a new project was undertaken in which the metallic Pd sample was bombarded with monoenergetic electrons of different energies. The $L\alpha_{1,2}$ x-ray spectra were measured at the University of Fribourg, using a 20 kV electron gun and the von Hamos crystal spectrometer [27]. The relative intensities of the $L\alpha_{1,2}M$ satellite x-ray lines were found to be different from those observed in the synchrotron radiation experiment. This is, however, not really surprising because, as mentioned before, the KO probabilities are not the same in electron-induced and photoinduced ionization. In addition, in the case of electrons, an additional process contributes to the L_3M double ionization (DI), namely the so-called two-step-two (TS2) process [28]. The TS2 mechanism corresponds to the knock-out of two bound electrons from the same atom by a single incoming electron. Note that in the standard KO process, named also two-step-one (TS1) process, the second electron is knocked out by the first ionized electron. In photoionization, the TS1 process does also exist, the first ionized electron being the photoelectron, but the TS2 process does not exist, the incoming photon being annihilated by the photoelectric effect.

The electron-induced TS process can be considered as a $(e, 3e)$ collision, with a doubly ionized atom and three outgoing electrons in the exit channel. It corresponds to a three

body break-up process in the framework of the four-body Coulomb scattering, and permits to investigate the electron correlation effects [29]. A powerful experimental method to study $(e, 3e)$ processes consists of performing inclusive coincidence measurements in which the momentum vectors of all outgoing particles are determined [30–33]. Such multicoincidence measurements, however, result in very low coincidence rates, which makes the experiment difficult and time consuming. In addition for solid samples, extremely thin foils are needed.

An alternative experimental approach consists of observing by means of high-resolution x-ray spectroscopy the radiative decay of the doubly ionized atoms. This method was used for instance in the works reported in [34] and [8]. In these studies the double KL and double KK ionization induced in several light atoms by low-energy electrons were determined as a function of the incident electron energy. The energy dependent double ionization cross sections (DICSs) were derived from the measured intensity ratios of the resolved L satellite- or K hypersatellite-to-parent diagram x-ray lines, using available experimental values for the electron-induced single K-shell ionization cross sections. A similar experimental approach was employed in the present project concerning the electron-induced double $L_3 M$ ionization of Pd. The measured relative intensities of the $L\alpha M$ satellite reflecting the total DICSs, the partial TS cross sections were determined by subtracting from the measured satellite intensities the Coster-Kronig and shake contributions.

For Pd the average energy shift of the $L\alpha M$ satellite components with respect to the parent diagram line is ~ 10 eV [35]. This energy separation is too small to be resolved by an energy-dispersive detector, but using the von Hamos crystal spectrometer the two x-ray lines can easily be separated. The project was nevertheless challenging for the following three reasons: first, experimental data for electron-induced L-subshell single ionization cross sections are scarce and existing data suffer from large uncertainties [36]. Analytical expressions [37] based on the distorted-wave Born approximation (DWBA) [38] provide values that are in satisfactory agreement with available experimental data but the predictions are poorly reliable in the near edge regions [39]. Secondly, the double LM ionization is more complicated than the double KL or KK ionization due to the L-subshell structures and the contribution to the measured DI of the LLM Coster-Kronig transitions. Last but not least, due to the low efficiency of crystal spectrometers, very thin targets cannot be used in high-resolution x-ray spectroscopy. Thin foils are also more

easily damaged when bombarded by intense medium-energy electron beams due to the resulting heat load. A relatively thick (about 100 μm) Pd foil was thus employed in our project. As a consequence, all employed electron beams were stopped in the target and the measured diagram and satellite x-rays reflected the single and double ionization induced by impact with electrons whose energies varied in the sample from the nominal beam energy down to zero. This made the investigation of the TS process as a function of the electron energy more difficult.

The above mentioned difficulties, however, could be circumvented and the project could be achieved successfully. In particular, the energy dependence problem was solved by using a novel method based on the decomposition of the thick target into slices of variable thicknesses. The measurements were performed for 15 different electron beam energies ranging from 4 keV to 18 keV. From the observed intensity ratios of the resolved $L\alpha M$ satellites to the parent $L\alpha_{1,2}$ diagram lines, the partial ratios corresponding to the TS process were determined as a function of the nominal electron energy, the contributions to the double $L_3 M$ ionization of the $L_1 - L_3 M_{4,5}$ CK transitions [40] and shake-off process having been subtracted beforehand. It was found that the variation of the TS cross sections as a function of the incoming electron energy was well reproduced by using the cross section energy dependencies proposed by Campos [37] and Pattard-Rost [41–43] for the parametrization of $(e, 3e)$ collisions. On the other hand, the experimental TS cross sections could be also determined directly from the measured cross-section-integrals, using the novel slice decomposition method.

C.   Ca KMM radiative Auger effect

The radiative Auger effect (RAE) is an exotic atomic decay channel in which both an x-ray photon and an Auger electron are emitted. In this process, the electron can also be promoted into an unfilled outer discrete level. The RAE, named sometimes 'semi-Auger' process [44], represents thus an intermediate or hybrid decay mode between a purely radiative and purely radiationless de-excitation. In the RAE, the transition energy is shared between the emitted photon and the Auger electron. The energy range of the emitted photon extends thus from zero (if the whole transition energy is transferred to the Auger electron) to a maximum energy called onset energy which is equal to the transition energy minus the binding energy of the subshell from which the Auger electron comes from. In the latter case, which is also the most probable one [45], the Auger electron

is emitted with a vanishing small kinetic energy. As a consequence, the x-ray spectrum corresponding to the RAE is continuous with a sharp edge at the onset energy and a long decreasing tail on the low-energy side extending theoretically down to zero. However, if the electron is not ejected from the atom but promoted to an outer discrete level, the energy conservation implies that the photon is emitted with a well-defined energy equal to the transition energy minus the energy difference between the initial and final levels of the excited electron. For this reason, RAE x-ray spectra may exhibit discrete structures above the onset energy.

Four electron levels are involved in a Radiative Auger (RA) transition, namely the level corresponding to the initial core hole, the level from which the transition electron originates and the initial and final levels of the Auger electron. The last level may correspond to a bound state or a state in the continuum. Thus, RA transitions are usually denoted $(nl, n'l')n_A l_A, n'_A l'_A$ if the Auger electron is excited in an outer bound level or $(nl, n'l')n_A l_A, \epsilon_A l'_A$ if the Auger electron is ejected into the continuum. In the last case, a simpler three electron notation is often found in the literature, the two last quantum numbers being omitted.

The RAE was predicted theoretically by F. Bloch and his coworker already in 1935 [9, 10] but the first RAE observation was done more than 30 years later by T. Åberg and J. Utriainen during a careful examination of the the low-energy tails of $K\alpha$ x-ray lines ($K - L$ transitions) of several light elements [46]. These RA transitions were called KLL RA transitions because they correspond to a $K - L$ radiative transition with the simultaneous emission or excitation of an Auger electron from the L shell. The RAE was explained by Åberg as resulting from the shake-off (SO) or shakeup (SU) process following the change of the average atomic potential during the x-ray hole transfer [47]. This interpretation has led to the terms RA SO and RA SU transitions, depending on the final state of the Auger electron (a continuum state or a bound state). Åberg's calculations of the RA transition probabilities were thus derived within the Sudden Approximation (SA) model using the same wavefunction overlap integrals as those employed in the calculations of the SO and SU probabilities. Other models of calculations were proposed later, e.g, configuration interaction calculations (CI) [48] and radiative field calculations performed within the framework of the second order many body perturbation expansion [49, 50].

The influence of the outer unoccupied subshells on the RA transitions, i.e., the sensitivity of the RAE to chemical and solid state

effects, was discussed already in the early seventies [44]. It was noticed later by J. Kawai that the $KL_{2,3}L_{2,3}$ RA spectrum resembles the K XANES or K EXAFS ones [51]. For this reason, Kawai re-named the RA structure occurring on the low-energy tail of the diagram lines 'extended x-ray emission fine structure' (EXEFS) to emphasize the analogy between the structures observed in the absorption spectrum (EXAFS) and the emission one (EXEFS). Since then, the novel EX-EFS technique has proven to be a simple but powerful tool to analyze the chemical states of elements in compounds [52, 53]. In addition, the EXEFS method does not need SR radiation and can thus be applied in in-house measurements using x-ray tubes.

Besides its use in the EXEFS method, the RA x-ray emission may also provide important information for the study of the many-particle interaction in atomic systems. Theoretically, the influence of the RAE on the atomic transition rates was taken into consideration in Scofield's relativistic Hartree-Fock calculations [54]. Several experimental works [55, 56] also pointed out the importance of considering the RA transitions in the fits of x-ray spectra to get reliable transition rates in PIXE (particle-induced x-ray emission) or XRF (x-ray induced fluorescence) measurements. Furthermore, structures observed in EXEFS measurements [57] showed that some

RA transitions which are forbidden by the selection rules in the standard Auger process are allowed within the configurational interaction model.

In principle the RAE can be investigated by x-ray emission spectroscopy (XES) or Auger emission spectroscopy (AES). In the case of RA SU transitions, however, AES cannot be employed since no electron is emitted. Thus, in order to get all RA transitions in a single measurement, XES is generally preferred to AES. To get a reliable RA x-ray spectrum, a precise and detailed knowledge of the background is needed. The latter originates mainly from the low-energy Lorentzian tails of the close lying diagram lines, from satellite x-ray lines and other inelastic scattering events. As mentioned before, satellite x-ray lines lie in most cases on the high-energy side of the parent diagram lines but their intensity should be fitted properly to get a correct value of the background. Wrong background values on the high energy sides of the diagram lines may indeed lead to backgrounds that are also incorrect in the RA region. On the other hand, due to the fact that the spectator vacancies can be located in different subshells and because of the numerous possibilities for the coupling of the vacancy angular momenta, satellite x-ray lines consist of many different transitions that scatter over a broad energy domain. Some of

these components may even be located on the low-energy side of the parent diagram transition. Such low-energy satellites were for instance observed in 3d transition elements [58, 59], for which the outer-shell p and d electron orbitals are widely overlapping [60]. Inelastic x-ray scattering processes in which bound electrons are promoted into outer empty states just above the Fermi level may also result in the appearance of x-ray structures on the low-energy side of the diagram lines. In general inelastic x-ray processes are weak except for incoming photons having an energy close to the absorption edge but just below it. In this case, the intensity of the x-ray spectrum corresponding to the inelastic x-ray scattering is resonantly enhanced [61] and contributes thus significantly to the low-energy side background. For the K shell, this resonant inelastic x-ray scattering process (RIXS), named also x-ray resonant Raman scattering (XRRS), was observed recently and the corresponding cross section determined for Al, Si and their oxides [62, 63]. The background enhancement due to RIXS processes can, however, be avoided by tuning the energy of the incoming photons just above the K edge. In this case the intensity of the satellites due to SO and KO processes is also minimized since the photon energy is smaller than the threshold energy for DI or, at least, smaller than the energies at which

the variation of the SO and KO processes as a function of the photon energy evinces a rapid increase [64]. This background optimization is, however, hardly feasible in RAE measurements employing conventional x-ray sources like x-ray tubes [65, 66] or charged particle beams [56, 67].

The onset energies of RA spectra lying close below the $K\alpha$ or $K\beta$ x-ray diagram lines, measurements of the RAE by means of low-resolution x-ray spectroscopy using solid state detectors [68] or gas detectors [69], are difficult to perform and need very careful and sophisticated methods of analysis. Although such detectors present the advantage to permit the measurement of the whole diagram plus RA x-ray spectrum at once, they cannot resolve the RA transitions which are covered by the strong low-energy tails of the diagram lines. Therefore, to collect a clean RA x-ray spectrum a high instrumental resolution of the order of a few eV is needed. The instrument should also permit to cover a wide energy range since the RA spectrum extends in principle down to vanishingly small energies. As mentioned before, the background can be minimized by using energy tunable monochromatic x-ray beams tuned just above the threshold energy for single K-shell ionization. Such conditions are fulfilled at best by using SR for the production of the target fluorescence and crystal spectrometers for the

measurement of the RA x-rays.

In the fourth project of the present Ph.D. thesis, the KMM RA x-ray spectrum of calcium ($Z = 20$) was measured. For the above mentioned reasons, SR and high-resolution x-ray spectroscopy were employed. The measurements were performed at the ID21 beamline of the ESRF, using the von Hamos curved crystal spectrometer of Fribourg [27]. At first the absorption spectrum of Ca was measured around the K edge in the fluorescence mode. This allowed us to choose the best beam energy for the RAE measurements. The latter were performed using SR beam energies lying 50 eV and 1455 eV above the K edge. The aim of the measurement at the higher beam energy was to probe the dependence of the RAE effect and background on the energy of the incoming photons. The main KMM RA structures occurring between the $K\alpha_{1,2}$ and $K\beta_{1,3}$ x-ray lines, 4 CCD positions were needed to cover the energy domain of interest. The measured spectra were normalized by the beam intensity and corrected for the self-absorption in the target. Corrections for the solid angle of the spectrometer, CCD quantum efficiency and crystal reflectivity were also considered. The RA x-ray spectra were constructed by subtracting from the experimental spectra the Voigtians corresponding to the $K\alpha$ and $K\beta$ diagram lines and $K\alpha L$ and $K\beta L$ satellites.

Numerical integrations of the residuals were applied to calculate the KMM RA yields. The low-energy tails of the RA transitions were fitted with exponential functions. The obtained KMM RA-to-$K\beta_{1,3}$ intensity ratio was found to be in good agreement with the theoretical value reported by Scofield [54].

III.   THESIS ARRANGEMENT

The thesis contains four main parts which correspond each to a separate publication.

The first two parts concern the L-subshell Coster-Kronig yields of Pd and Xe which were determined by means of synchrotron-radiation-based high-resolution x-ray spectroscopy. The experiments were carried out separately at ELETTRA using in both cases the Johansson bent crystal spectrometer of IJS Ljubljana. Besides the CK rates f_{12}, f_{13} and f_{23} that represented the main objective of the two experiments, the partial $L_1 - L_3 M_{4,5}$ CK yield of Pd and the L_1-subshell fluorescence yield of Xe could also be deduced from the measurements thanks to the high resolution of the employed crystal spectrometer. Both studies were already published as regular articles, the first one in Physical Review A 80, 012512 (2009) and the second one in Physical Review A 81, 012501 (2010).

The third part of the thesis concerns an

in-house experiment devoted to the investigation of the L_3M double ionization (DI) induced in Pd by impact with medium-energy electrons. The particular aim of this study was to determine the contribution of the Two-Step (TS) process to the DI as a function of the energy of the incoming electrons. The measurements were performed with the von Hamos curved crystal spectrometer of Fribourg. The corresponding article was submitted recently to Physical Review A.

The fourth and last part is related to the radiative Auger effect (RAE), a hybrid decay channel of atomic inner-shell vacancies in which both a photon and an Auger electron are emitted. This study represents a continuation of former RAE investigations performed by the Atomic and X-Ray Physics (AXP) group of Fribourg. In these former experiments, the KLM and KMM RAE probabilities were determined for 4d transition elements, using x-ray tubes and a Laue-type DuMond bent crystal spectrometer. In the present project, the KMM RA emission of Ca was measured, using the Bragg-type von Hamos crystal spectrometer and synchrotron radiation for the production of the sample fluorescence. The measurements were performed at the ESRF. The corresponding paper is near completion and will be submitted soon to Physical Review A.

The curriculum vitae and list of publications of the author as well as the acknowledgements are enclosed at the end of the thesis.

[1] W. C. Röntgen, Sitzungsberichte der Physik.-med. Gesellschaft zu Würzburg.1895. **S**, 132 (1896).

[2] C. N. Brown, Eng. Sci. Educ. J. **5**, 105 (1996).

[3] D. C. Koningsberger and R. Prins, eds., *X-ray Absorption : Principles, Applications, Techniques of EXAFS, SEXAFS and XANES* (Wiley, New York, 1988).

[4] A. Föhlischa, J. Hasselström, O. Karis, P. Väterlein, N. Mårtensson, A. Nilsson, C. Heske, M. Stichler, C. Keller, W. Wurth, et al., Chem. Phys. Lett. **315**, 194 (1999).

[5] J. J. Rehr and R. C. Albers, Rev. Mod. Phys. **70**, 621 (2000).

[6] J. J. Rehr, Coord. Chem. Rev. **249**, 131 (2005).

[7] T. Åberg, Phys. Rev. **156**, 35 (1967).

[8] K. Fennane, J.-Cl. Dousse, J. Hoszowska, M. Berset, W. Cao, Y.-P. Maillard, J. Szlachetko, M. Szlachetko, and M. Kavčič, Phys. Rev. A **79**, 032708 (2009).

[9] F. Bloch and P. A. Ross, Phys. Rev. **47**, 884 (1935).

[10] F. Bloch, Phys. Rev. **48**, 187 (1935).

[11] W. L. Bragg, Nature **90**, 410 (1912).

[12] D. Coster and R. de L. Kronig, Physica **2**, 13 (1932).

[13] W. Bambynek, B. Crasemann, R. W. Fink, H.-U. Freund, H. Mark, C. D. Swift, R. E. Price, and P. V. Rao, Rev. Mod. Phys **44**, 716 (1972).

[14] M. H. Chen, B. Crasemann, and H. Mark, Phys. Rev. A **24**, 177 (1981).

[15] M. O. Krause, J. Phys. Chem. Ref. Data **8**, 307 (1979).

[16] S. Puri, D. Mehtad, B. Chand, N. Singh, and P. N. Trehan, X-ray Spectrom. **22**, 358 (1993).

[17] B. L. Doyle and S. M. Shafroft, Phys. Rev. A **19**, 1433 (1979).

[18] E. Rosato, Nucl. Instrum. Methods Phys. Res. B **15**, 591 (1986).

[19] J. L. Campbell, At. Data Nucl. Data Tab. **85**, 291 (2003).

[20] R. W. Dunford, E. P. Kanter, B. Krässig, S. H. Southworth, L. Young, P. H. Moklerand, T. Stöhlker, S. Cheng, A. G. Kochur, and I. D. Petrov, Phys. Rev. A **74**, 062502 (2006).

[21] J. L. Campbell, At. Data Nucl. Data Tab. **95**, 115 (2009).

[22] W. Jitschin, G. Materlik, U. Werner, and P. Funke, J. Phys. B **18**, 1139 (1985).

[23] J. H. Hubbell, Phys. Med. Biol. **51**, R245 (2006).

[24] T. K. Sham, Phys. Rev. B **31**, 1888 (1985).

[25] S. Botti, A. Schindlmayr, R. D. Sole, and L. Reining, Rep. Prog. Phys. **70**, 375 (2007).

[26] M. Kavčič, A. G. Karydas, and C. Zarkadas, Nucl. Instrum. Methods Phys. Res. B **222**, 601 (2004).

[27] J. Hoszowska, J.-Cl. Dousse, J. Kern, and C. Rhême, Nucl. Instrum. Methods Phys. Res. A **376**, 129 (1996).

[28] T. A. Carlson and M. O. Krause, Phys. Rev. **140**, 1057 (1965).

[29] J. Berakdar, A. Lahmam-Bennani, and C. D. Cappello, Phys. Rep. **374**, 91 (2003).

[30] A. Lahmam-Bennani, C. Dupré, and A. Duguet, Phys. Rev. Lett. **63**, 1582 (1989).

[31] M. A. Coplan, J. H. Moore, and J. P. Doering, Rev. Mod. Phys. **66**, 985 (1994).

[32] Y. V. Popov, C. D. Cappello, B. Joulakian, and N. M. Kuzmina, J. Phys. B **27**, 1599 (1994).

[33] B. E. Marji, C. Schröter, A. Duguet, A. Lahmam-Bennani, M. Lecas, and L. Spielberger, J. Phys. B **30**, 3677 (1997).

[34] O. Mauron and J.-Cl. Dousse, Phys. Rev. A **66**, 042713 (2002).

[35] M. Polasik, K. Kozioł, K. Słabkowska, M. Czarnota, and M. Pajek, J. Phys. Conf. Ser. **163**, 012050 (2009).

[36] C. J. Powell, Rev. Mod. Phys. **48**, 33 (1976).

[37] C. S. Campos, M. A. Z. Vasconcellos, J. C. Trincavelli, and S. Segui, J. Phys. B **40**, 3835 (2007).

[38] S. Segui, M. Dingfelder, and F. Salvat, Phys. Rev. A **67**, 062710 (2003).

[39] C. Tang, Z. Luo, Z. An, F. He, X. Peng, and X. Long, Phys. Rev. A **65**, 052707 (2002).

[40] W. Cao, J. Hoszowska, J.-Cl. Dousse, Y. Kayser, M. Kavčič, M. Žitnik, K. Bučar, A. Mihelič, J. Szlachetko, and K. Słabkowska, Phys. Rev. A **80**, 012512 (2009).

[41] T. Pattard and J. M. Rost, Phys. Scr. **T80**, 295 (1999).

[42] T. Pattard, J. Phys. B **35**, L207 (2002).

[43] J. M. Rost and T. Pattard, Phys. Rev. A **55**, R5 (1997).

[44] J. W. Cooper and R. E. LaVilla, Phys. Rev. Lett. **25**, 1745 (1970).

[45] M. O. Krause, T. A. Carlson, , and R. D. Dismukes, Phys. Rev. **170**, 37 (1968).

[46] T. Åberg and J. Utriainen, Phys. Rev. Lett. **22**, 1346 (1969).

[47] T. Åberg, Phys. Rev. A **4**, 1735 (1971).

[48] K. G. Dyall and F. P. Larkins, J. Phys. B **15**, 4103 (1982).

[49] V. O. Kostroun and G. B. Baptista, Phys. Rev. A **14**, 363 (1976).

[50] G. B. Baptista, J. Phys. B : At. Mol. Opt. Phys. **34**, 389 (2001).

[51] J. Kawai, T. Nakajima, T. Inoue, H. Adachi, M. Yamaguchi, K. Maeda, and S. Yabuki, Analyst **119**, 601 (1994).

[52] H. Hayashi, N. Watanabe, and Y. Udagawa, J. Phys. : Condens. Matter **8**, 37 (1996).

[53] J. Kawai, Analy. Sci. **21**, 733 (2005).

[54] J. H. Scofield, Phys. Rev. A **9**, 1041 (1974).

[55] J. L. Campbell, A. Perujo, W. J. Teesdale, and B. M. Millman, Phys. Rev. A **33**, 2410 (1986).

[56] M. Budnar, A. Mühleisen, M. Hribar, H. Janžekovič, M. Ravnikar, Ž. Šmit, and M. Žitnik, Nucl. Instrum. Methods Phys. Res. B **63**, 377 (1992).

[57] I. Abrahams, D. S. Urch, B. Vrebos, and M. West, J. Phys. B : At. Mol. Opt. Phys. **32**, L597 (1999).

[58] D. F. Anagnostopoulos, R. Sharon, D. Gotta, and M. Deutsch, Phys. Rev. A **60**, 2018 (1999).

[59] R. Diamant, R. Sharon, W. A. Caliebe, C.-C. Kao, and M. Deutsch, J. Phys. B : At. Mol. Opt. Phys. **39**, 651 (2006).

[60] R. D. Cowan, *The Theory of Atomic Structure and Spectra* (University of California Press, Berkeley, 1981).

[61] F. Gel'mukhanov and H. Ågren, Phys. Rep. **312**, 87 (1999).

[62] J. Szlachetko, J.-Cl. Dousse, J. Hoszowska, M. Pajek, R. Barrett, M. Berset, K. Fennane, A. Kubala-Kukus, and M. Szlachetko, Phys. Rev. Lett. **97**, 073001 (2006).

[63] J. Szlachetko, J.-Cl. Dousse, J. Hoszowska, M. Berset, W. Cao, M. Szlachetko, and M. Kavčič, Rev. Sci. Instrum. **78**, 093102 (2007).

[64] T. D. Thomas, Phys. Rev. Lett. **52**, 417 (1984).

[65] A. Mühleisen, M. Budnar, and J.-Cl. Dousse, Phys. Rev. A **54**, 3852 (1996).

[66] C. Herren and J.-Cl. Dousse, Phys. Rev. A **56**, 2750 (1997).

[67] S. P. Limandri, A. C. Carreras, R. D. Bonetto, and J. C. Trincavelli, Phys. Rev. A. **81**, 012504 (2010).

[68] H. R. Verma, J. Phys. B: At. Mol. Opt. Phys. **33**, 3407 (2000).

[69] D. Mitra, M. Sarkar, D. Bhattacharya, and L. Natarajan, X-Ray Spectrom. **37**, 585 (2008).

Part 1.

L-subshell Coster-Kronig yields of palladium determined via synchrotron-radiation-based high-resolution x-ray spectroscopy

W. Cao[1], J. Hoszowska[1], J.-Cl. Dousse[1], Y. Kayser[1], M. Kavčič[2], M. Žitnik[2], K. Bučar[2] A. Mihelič[2], J. Szlachetko[3], and K. Słabkowska[4]

[1] *Department of Physics, University of Fribourg, Ch. du Musée 3, Ch-1700 Fribourg, Switzerland*

[2] *J. Stefan Institute, P.O. Box 3000, SI-1001 Ljubljana, Slovenia*

[3] *European Synchrotron Radiation Facility (ESRF), 38043 Grenoble, France*

[4] *Faculty of Chemistry, Nicholas Copernicus University, 87-100 Toruń, Poland*

I. INTRODUCTION

The Coster-Kronig (CK) transitions are special Auger transitions in which the initial and final atomic states are characterized by the presence of a vacancy in the same major shell. In the CK decay an initial vacancy in the i-subshell is transferred to a higher subshell j, and a bound electron is ejected simultaneously. The vacancy transfer probability is described by the so-called CK yield f_{ij}. The CK rates depend strongly on the overlap between the initial and final state wavefunctions, and are very sensitive to electron binding energies as well as solid-state effects [1, 2].

Experimental determination of L-shell CK yields is challenging. Data are scarce or nonexistent and often suffer from large uncertainties. Most measurements were performed by means of the widely used $K\alpha$-L x-ray coincidence method [1, 3] which has proved to be a powerful tool for determining the f_{23} CK yield and the L_2- and L_3-subshell fluorescence yields [3, 4]. For the L_1 subshell this technique cannot be used since the KL_1 radiative transition is dipole forbidden. In addition, the $K\alpha$ and L x-ray coincidence detection is difficult to apply to low-Z and mid-Z elements. The alternative photoionization experimental method was limited to the use of radio-nuclides [5]. About two decades ago, with the advent of x-ray synchrotron radiation sources the photoionization method based on the selective photoionization of the L subshells by monochromatic synchrotron radiation was introduced [6]. By this mean, the Coster-Kronig vacancy shifts to higher subshells can be switched on and off. By tuning the photon energy across the absorption L-edges and recording the x-ray fluorescence lines [7, 8] or detecting Auger electrons [9, 10] all CK yields can be obtained. So far, measurements of the x-ray fluorescence lines were performed by means of energy-dispersive semiconductor detectors. To the best of our knowledge, high-resolution x-ray emission spectroscopy has not been employed.

The L-subshell CK transitions around Z=48 have drawn plenty of attention due to the predicted cutoff of the $L_1 - L_3M_{4,5}$ CK transitions in this region of the periodic table. For elements above the Z value corresponding to the cutoff, the CK transition probabilities vanish because the transitions are energetically forbidden. From theoretical calculations [11] an abrupt cut-off between Z=49 and Z=50 is expected, however, experimental data suggest that the cut-off is not sharp but extends over a certain range $48 \leq Z \leq 50$ [12, 13]. Indeed, more experimental data are needed in this mid-Z regime.

In this paper we report on the high-

resolution synchrotron-radiation-based determination of the L-subshell f_{12}, f_{13} and f_{23} Coster-Kronig yields of Pd ($Z=46$). The palladium L-edge absorption spectrum [14, 15] and the L-shell emission lines [16] are well understood, making it a good candidate for CK rate determination. The measurements of the $L\alpha_{1,2}$ ($L_3 - M_{4,5}$) and $L\beta_1$ ($L_2 - M_4$) lines were carried out by means of high-resolution x-ray emission spectroscopy. From the measured x-ray absorption spectrum the individual L-subshell photoionization cross sections were determined and compared to theoretical values. The CK yields were derived from the variation of the $L\alpha_{1,2}$ or $L\beta_1$ fluorescence line intensities at the absorption L-edges due to the onsets of CK vacancy transfers.
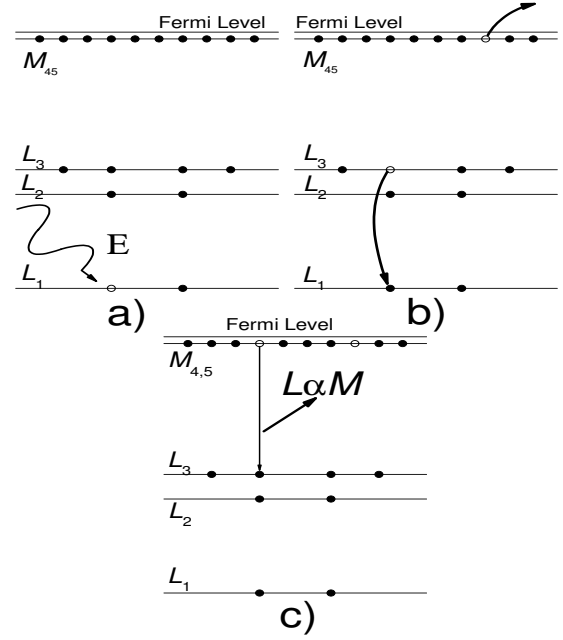

FIG. 1: The $L_1 - L_3 M_{4,5}$ Coster-Kronig transition and the $L\alpha M$ satellite x-ray emission. (a) Photoionization of the L_1 electron, (b) Coster-Kronig process, (c) $L\alpha M$ satellite transition.

II.   EXPERIMENT

Moreover, from the intensities of the resolved $L\alpha M$ satellite x-ray transitions the partial CK yield $f_{13}^{L_1 L_3 M}$ was determined. This was possible because for elements with $Z \leq 91$ the $L_2 - L_3 M$ CK transition is energetically forbidden. For illustration, the $L_1 - L_3 M_{4,5}$ CK transition together with the fluorescence decay following the CK process are shown in Fig. 1. This experimental result is new, since the low-resolution x-ray spectroscopy method [8, 17] cannot give direct information on the $L\alpha M$ satellite lines resulting from the $L_1 - L_3 M_{4,5}$ CK process.

The experiments were carried out at the bending magnet XAFS beamline at the Elettra synchrotron, Trieste, Italy. The primary x-ray beam was monochromatized by means of a double-crystal Si(111) monochromator. To suppress higher photon energies a Pt-coated mirror was used and the second monochromator crystal was detuned with respect to the first one. The energy bandwidth of the monochromatized radiation was 0.4 eV and the photon flux was $\sim 10^8$ ph/s. The top-view of the experimental setup is shown in Fig. 2. For the x-ray absorption experiment
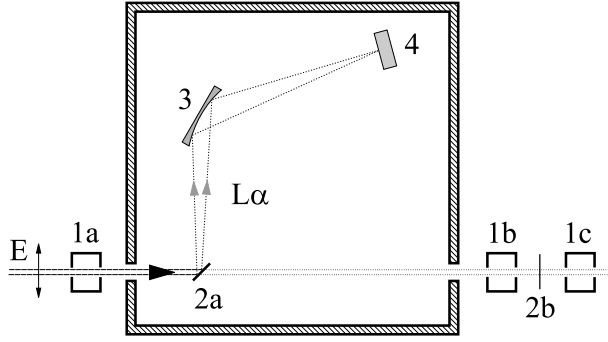
FIG. 2: A top-view scheme of the experimental setup showing the ionization chambers (1), the x-ray spectrometer with the palladium target (2a), silicon crystal (3) and the CCD detector (4). For the *L*-edge absorption measurement a thin Pd foil (2b) was mounted perpendicular to the beam in the vacuum chamber installed between the second (1b) and the third (1c) ionization detector. The first ionization chamber (1a) served to monitor the photon flux during the x-ray emission spectra measurements.

the dedicated vacuum chamber installed between the second and the third ionization chambers was employed. The *L*-edge x-ray absorption spectrum was recorded at room temperature in the transmission mode. A self-supported 1.66 μm thick Pd metallic foil was used. The photon energy was tuned with a step width of 0.5 eV in the range from 3120 eV to 3700 eV. The incident and the transmitted intensities were corrected for the attenuation in the Kapton™ windows in the beam path as well as for the gas absorption in the ionization chambers. The experimental absorption coefficients were normalized in the L_3 pre-edge region to the attenuation data from the NIST database [18].

For the high-resolution x-ray emission spectra measurements the Johansson-type curved crystal spectrometer of Ljubljana [19] was installed in the beamline hutch between the first and the second ionization chamber (see Fig. 2). A 114 μm thick metallic palladium sample was mounted in the evacuated spectrometer chamber at 45 deg. to the incoming beam. The *L*α x-ray fluorescence lines of Pd were measured using a cylindrically curved Si(111) crystal in the first order of reflection. The x-ray fluorescence was observed at the angle of 90 deg. with respect to the horizontally polarized incident photon beam to minimize the background due to elastic scattering. The diffracted x-rays were recorded with a thermoelectrically cooled (-40°C) back illuminated CCD (charge-coupled device) camera consisting of 770$\times$1153 pixels with a pixel size of 22.5$\times$22.5 μm^2. Positions of the target, crystal and detector were kept fixed during the whole experiment to ensure constant instrumental parameters. The instrumental energy resolution of the x-ray spectrometer was $\sim$ 0.3 eV. For normalization purposes the incident photon flux was recorded with the first ionization chamber each 10 seconds. Beam intensities were corrected for absorption in the gas and the 25 μm thick exit Kapton™ window of the ionization detector. Depending on the incident photon energy and the total photon number,

the time to collect an $L\alpha$ x-ray spectrum varied from 50 to 170 minutes. The fluorescence spectra were calibrated using the reference energy of the $L\alpha_1$ x-ray line of 2838.64(5) eV reported in Ref. [20].

A series of 35 $L\alpha$ x-ray emission spectra was recorded. The incident beam energy was tuned from the L_3-edge (3174 eV) to 3675 eV, i.e., 68 eV above the L_1-edge (3607 eV). Because of software acquisition problems at the end of the experiment, the measurements of the $L\beta_1$ x-ray emission lines could not be completed successfully. The latter were carried out later at the ID21 beamline at the ESRF, Grenoble, employing the Fribourg von Hamos curved crystal spectrometer [21]. The same thick Pd target was used and mounted at 45.8 deg. with respect to the incident beam and a quartz ($1\bar{1}0$) crystal in the first order of reflection was employed. Four $L\beta_1$ x-ray spectra were recorded, two at incident beam energies below and two above the L_1-edge.

III. DATA ANALYSIS

A. Spectra fitting

The Pd $L\alpha$ x-ray spectra measured at three different photon energies are shown in Fig. 3. The advantage of the high-resolution emission spectroscopy is that the individual $L\alpha_{1,2}$ x-ray transitions can be resolved. As a consequence, an elaborated fitting procedure [8] can be avoided. However, the diagram transitions may be accompanied by satellite lines resulting from additional vacancies present in the N- and M-shells during the x-ray transition. In inner-shell photoionization these multiple-vacancy configurations may be induced by shake [22] and Coster-Kronig processes. Due to the reduced screening of the nuclear charge the x-ray satellite lines are shifted in energy with respect to the diagram transitions.

To identify the underlying satellite structure for the fitting procedure the observed x-ray spectra were compared to multi-configuration Dirac-Fock (MCDF) calculations [23]. For illustration, x-ray spectra measured at incident beam energies between the L_3- and L_2-edges (E=3180.5 eV), between the L_2- and L_1-edges (E=3550 eV) and well above the L_1-edge (E=3646 eV), together with the results of the MCDF calculations are depicted in Fig. 3(a), Fig. 3(b) and Fig. 3(c), respectively. The energies and relative intensities of the individual MCDF multiplet components indicate that the first order $L\alpha N$ satellite is not resolved from the $L\alpha_{1,2}$ lines. This overlap of the $L\alpha N$ satellite transitions with the diagram lines contributes to a non-lifetime broadening of the latter. In contrast, the $L\alpha M$ satellite is well

separated from the parent diagram lines. The calculated average energy shift of the $L\alpha M$ satellite transitions relative to the $L\alpha_1$ line amounts to 10.16 eV.

From Fig. 3 it can be seen that the $L\alpha$ x-ray emission spectrum depends on the photon energy. For incident beam energies in the vicinity of the L_3-edge, the measured $L\alpha$ lines were found to be resonantly enhanced and narrowed. For photon energies slightly above the L_3-edge, the resonant inelastic x-ray scattering (RIXS) process leads to additional peaks in the $L\alpha_{1,2}$ x-ray spectrum. For illustration, the $L\alpha_{1,2}$ x-ray spectrum observed at an incident beam energy 6.5 eV above the L_3-edge is shown in Fig. 3(a). Detailed works on the L-edge RIXS for other elements can be found elsewhere [24, 25]. With increasing photon energy, the $L\alpha N$ satellite lines due to the shake process start to broaden the diagram lines. This nonlifetime broadening becomes more important when additional holes in the N shell are created via the $L_{1,2} - L_3 N$ CK transitions. For energies above the L_1-edge, the opening of the $L_1 - L_3 M_{4,5}$ CK channel results in a prominent M-shell satellite line [see Fig. 3(c)].

Taking into account the above considerations, the fitting procedure was based on the following assumptions. The $L\alpha_{1,2}$ and $L\beta_1$ lines consist of the diagram transitions and the N-shell satellites that contribute to the
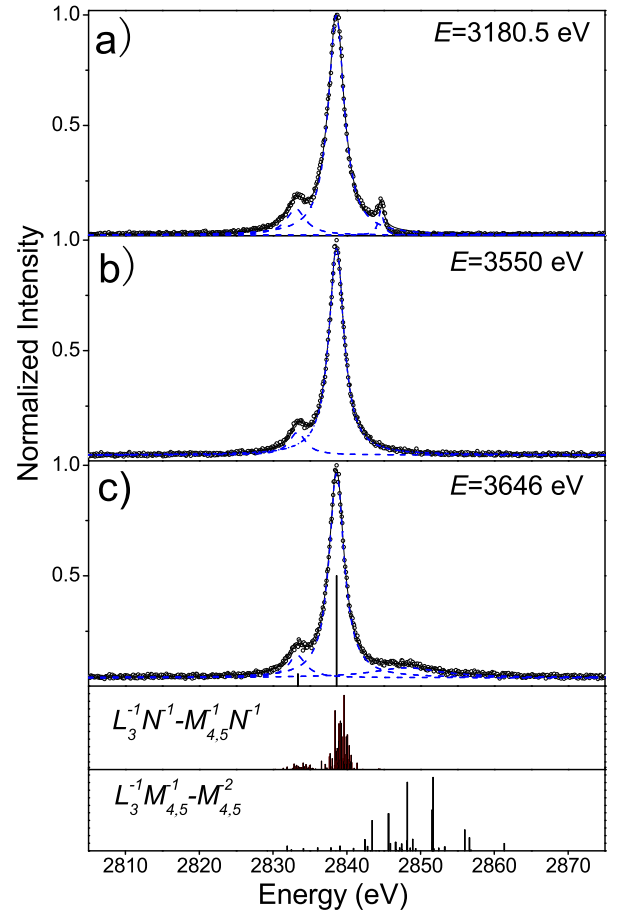

FIG. 3: (color online) Fitted high-resolution $L\alpha$ x-ray spectra of Pd at different incident beam energies. The solid thick lines represent the total fit to the experimental data (dots) and the dashed lines the individual components. (a) The peak on the high energy side of the $L\alpha$ line is due to RIXS (see text). (b) Shown is the spectrum consisting of the $L\alpha_{1,2}$ diagram lines and the unresolved N-satellites. (c) The $L\alpha$ diagram lines, the N-satellite and resolved M-satellite lines. The stick spectra in the lower panels correspond to MCDF calculations for the $L\alpha N$ and $L\alpha M$ satellite transitions, respectively.

spectral broadening of the Lorentzian profiles, while the $L\alpha M$ satellite transitions are well resolved from the diagram lines. The

high-resolution x-ray spectra were fitted by means of the least-square minimization program Peakfit^{TM}. The non-lifetime broadening of the $L\alpha_{1,2}$ and $L\beta_1$ lines was accounted for by letting the Lorentzian widths free in the fit and the $L\alpha M$ satellite line was fitted with a single Lorentzian function. An average energy shift of 9.68(16) eV was found for the $L\alpha M$ satellite, comparable to the value of 10.16 eV predicted by MCDF calculations.

B. Self-absorption corrections

The fitted $L\alpha$ intensities were normalized to the incident beam flux and data collecting time. In addition, to account for the self-absorption of the fluorescence x-rays and attenuation of the incident photon beam in the target, all fitted intensities were multiplied by the following dimensionless correction factor

$$F_{corr} = \frac{[\mu(E)/cos(\theta_1) + \mu_e/cos(\theta_2)]t}{1 - e^{-[\mu(E)/cos(\theta_1) + \mu_e/cos(\theta_2)]t}}, \quad (1)$$

where $\mu(E)$ stands for the total experimental absorption coefficient at the incident beam energy E and μ_e corresponds to the absorption coefficient at the $L\alpha$ (or $L\beta$) energy from [18], t is the target thickness and θ_1 and θ_2 are the angles of the incident and fluorescence photon beams with respect to the normal to the sample surface. Note that for a thick target as the one used in the present exper-
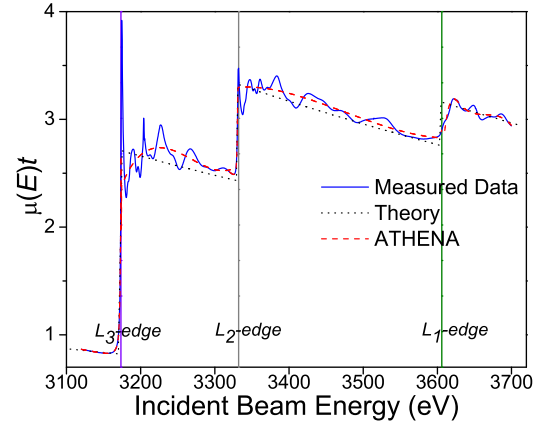

FIG. 4: (color online) Experimental and theoretical [18] photoabsorption for a 1.66 μm thick palladium sample. For comparison, the "smoothed background" calculated by means of the ATHENA program is also plotted.

iments, the denominator of Eq.1 is approximately 1.

C. Correction of the L x-ray fluorescence intensities for solid-state effects

The measured L x-ray absorption spectrum is depicted in Fig. 4, where the total photoabsorption coefficient μ multiplied by the thickness t of the Pd foil employed for this measurement is plotted as a function of the energy of the incoming photon beam.

The more complex electronic structure of solids compared to atoms results in a different behavior of the absorption coefficient as a function of the photon energy. For Pd, due to the rich hybridization states, the L-edge

absorption spectrum exhibits x-ray absorption near-edge structures (XANES), which can extend as much as 64 eV above the L_3-edge [14], and for photon energies beyond this region the extended x-ray absorption structures (EXAFS) [26]. As a consequence, photoabsorption cross sections at the L-edges are either enhanced or diminished compared to the atom-like cross sections for an isolated atom [14, 27]. To eliminate the solid-state effects and to extract the real atomic cross section from the measured data, the ATHENA [28, 29] program was employed. The calculations were based on the assumption that the EXAFS oscillations are small and that XANES dominates near threshold. The partial cross sections were normalized in the EXAFS regions defined according to [14] and the ATHENA spline algorithm was used. The binding energies E_i of the L_i subshells were determined from the first order derivatives of the rising absorption edges. The calculated "smoothed background" going through the oscillations corresponds to the atom-like photoabsorption cross section $\mu^{at}(E)$. The latter is compared to the measured photoabsorption cross section $\mu(E)$ in Fig. 4. Since in the energy domain of interest, the coherent and incoherent scattering photoionization cross sections are negligibly small compared to the photoelectric cross section, the total photoionization cross section $\sigma(E)$ and

$\sigma^{at}(E)$ were approximated by the $\mu(E)$ and $\mu^{at}(E)$, respectively. Furthermore, subtracting from $\sigma(E)$ and $\sigma^{at}(E)$ the polynomial functions determined by means of the program ATHENA from the data in the three pre-edge regions, the subshell photoionization cross sections $\sigma_i(E)$ and $\sigma_i^{at}(E)$ can be obtained.

To account for the solid-state effects, the atom-like $L\alpha$ fluorescence intensity $I_i^{at}(E)$ originating from the decay of a primary vacancy in the L_i-subshell was derived from the partial experimental intensity $I_i(E)$ using the following expression:

$$I_i^{at}(E) = \frac{I_i(E)}{U_i(E)}, \qquad (2)$$

where the correction function $U_i(E)$, as defined in [29], is

$$U_i(E) = 1 + \frac{\sigma_i(E) - \sigma_i^{at}(E)}{\sigma_i^{at}(E_i)}. \qquad (3)$$

It should be noted that $I_3(E)$ was deduced in a straightforward way from the fits of the $L\alpha$ line measured with beam energies below the L_2-edge, whereas for $i = 2$ and $i = 1$, the $L\alpha$ fluorescence originating from photoionization of the lower lying subshell(s) was subtracted beforehand (see Sect. IV). A similar but simpler (because of a single absorption edge) procedure was employed to correct the $L\beta_1$ intensities.

D. Parametrization of the *L*-subshell cross sections

The experimental $L\alpha$ fluorescence intensity $I(E)$ is proportional to the total $L\alpha$ x-ray production cross section $\sigma_{L\alpha}^{X}(E)$ which can be written as

$$\sigma_{L\alpha}^{X}(E) = \omega_{L\alpha}[\sigma_3(E) + f_{23}\sigma_2(E) + (f_{13}^{L_1 L_3 N} + f_{12}f_{23} + f'_{13})\sigma_1(E)] + \omega_{L\alpha M} f_{13}^{L_1 L_3 M}\sigma_1(E), \quad \text{(4a)}$$

where $\sigma_i(E)$ are the L_i (i=1,2 or 3) subshell photoionization cross sections and f'_{13} denotes the L_1 to L_3 hole transfer rate resulting from the $L_1 L_3$ radiative transition. The $\omega_{L\alpha}$ and $\omega_{L\alpha M}$ stand for the $L\alpha$ diagram line and $L\alpha M$ satellite fluorescence yields, respectively. Similarly, the $L\beta$ x-ray production cross section $\sigma_{L\beta}^{X}$ reads

$$\sigma_{L\beta}^{X}(E) = \omega_{L\beta}[\sigma_2(E) + f_{12}\sigma_1(E)], \quad \text{(4b)}$$

where $\omega_{L\beta}$ is the partial $L\beta_1$ fluorescence yield. The CK rates can be derived from the intensity jumps of the measured L x-ray fluorescence at the L-edges, provided the dependence of the subshell photoionization cross sections $\sigma_i(E)$ on the incident photon energy is known.

It is generally assumed that the cross sections vary smoothly with photon energy and within a certain energy range the dependence can be described by a power-law [8, 30].

In the mid-Z range, the following analytical function can be used:

$$\sigma_i^{at}(E) = a_i[E(keV)]^{b_i}, \quad \text{(5)}$$

where a_i and b_i are the fitting parameters for a particular subshell i. The dependence is different for individual L_i-subshells and changes in the vicinity of the L-edges.

The XANES and EXAFS modulations in our experimental absorption spectrum did not permit a reliable power-law fit to the data. In order to extract the a_i and b_i parameters we have resorted to the theoretical absorption coefficients [18, 31]. The values from the NIST database [18] were found to be in good agreement with our experimental data. However, it should be noted that the photoabsorption cross sections in the energy region of interest are calculated with an energy step of $\sim$ 100 eV and a smaller energy grid is obtained from an interpolation algorithm.

This fact affects the accuracy of the fit. An alternative is to use the data given by Ref. [31] in which a smaller energy grid is applied. Both sets of calculated data agree quite well below the L_1-edge. For the L_1 absorption coefficient, however, values from [31] were found to be $\sim 22\%$ smaller than those from [18] and the present experimental results. Therefore, to obtain the a_i and b_i parameters the following approach was adopted. First, the parameters a_i and b_i for the L_3 and L_2 absorption coefficients and the b_1 were extracted from the data of Henke *et al.* [31] using Eq.(5). To get a_1, the data from [18] were fitted with a fixed value of the b_1 parameter obtained from the former fit. The obtained fitting parameters are collected in Table I. It can be seen that b_2 and b_3 are almost the same, while a_2 is about half of a_3. These values are consistent with those predicted by Jitschin *et al.* [17] for elements with $47 \leq Z \leq 51$. For comparison, the fitted parameters for the data from Ref. [18], calculated with an interpolated energy step of 2 eV, are also listed in Table I.

The experimental and theoretical [18] photoabsorption coefficients are shown on the same plot of Fig. 4. Due to the L_3- and L_2-edge "white lines" which originate from photoexcitation to the unfilled valence states as well as the oscillatory structures resulting from solid-state effects, differences between the theoretical and experimental absorption data can be observed. However, the calculated "smoothed values", for which the changes in the absorption cross sections due to XANES and EXAFS were averaged out, are found in reasonable agreement with theory. The minor deviations from the power-law dependence of the cross sections based on the independent particle approximation are related to electron-correlations effects [30].

IV.   RESULTS AND DISCUSSION

The f_{23} CK yield was extracted from the $L\alpha$ intensity jump at the L_2-edge. First, the atom-like fluorescence intensity below the L_2-edge was fitted with the following expression:

$$I_3^{at}(E) = Ca_3\omega_{L\alpha}[E(keV)]^{b_3} \qquad (6)$$

yielding the parameter $A_3 = Ca_3\omega_{L\alpha}$, where C is the instrumental proportionality constant. To derive the CK contribution, the fluorescence intensities $I_3^{at}(E)$ for energies above the L_2-edge were extrapolated and subtracted from the $I(E)$ data. Since the L_3 EXAFS oscillations are very small for photon energies $E > E_2$, we have assumed that the extrapolated values $I_3(E)=I_3^{at}(E)$. The obtained $I_2(E)$ intensities were converted using the correction function $U_2(E)$ to atom-like values $I_2^{at}(E)$. The latter were fitted with

TABLE I: Analytical fit to the *L*-subshell photoabsorption cross sections of palladium (in units of 10^3 cm^{2}g^{-1}).

Ionized Subshell	Fitted Function	Fitted Function[a]
L_3	$16.483[E(keV)]^{-2.456}$	$11.413[E(keV)]^{-2.158}$
L_2	$8.639[E(keV)]^{-2.442}$	$11.710[E(keV)]^{-2.711}$
L_1	$1.082[E(keV)]^{-1.253}$	$8.739[E(keV)]^{-2.937}$

[a]Fit to the data from [18] (see text).
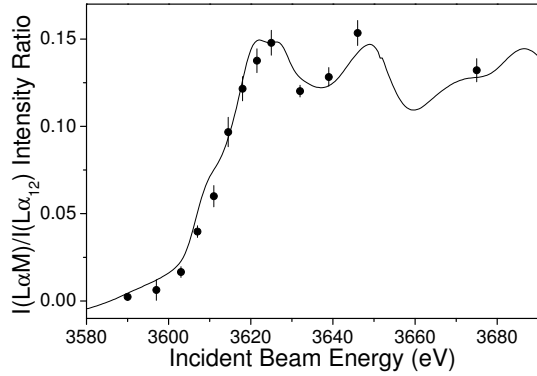
FIG. 5: Ratio of the $L\alpha M$ satellite line to the diagram line versus the photon energy. The solid line represents the experimental photoionization cross section $\sigma_1(E)$ normalized to the ratio at an energy of E=3625 eV.

a similar function providing the parameter $A_2 = f_{23}Ca_2\omega_{L\alpha}$. The value for f_{23} was then derived from the relation

$$f_{23} = \frac{A_2 a_3}{A_3 a_2}. \qquad (7)$$

For the f_{13} yield, first the partial CK yield $f_{13}^{L_1L_3N}$ was determined. To this end, a similar approach as for f_{23} was adopted. The extrapolated values for $I_2^{at}(E)$ and $I_3^{at}(E)$ were first subtracted from $I(E)$ giving the intensity $I_1^{L_1L_3N}(E)$, and after correction with

$U_1(E)$ the corresponding atom-like function $I_1^{L_1L_3N^{at}}(E)$ was fitted to obtain the value for the parameter $A_1^{L_1L_3N}$:

$$A_1^{L_1L_3N} = (f_{13}^{L_1L_3N}+f_{12}f_{23}+f'_{13})Ca_1\omega_{L\alpha}. \quad (8)$$

Subsequently, the partial CK $f_{13}^{L_1L_3N}$ yield was calculated using the following expression:

$$f_{13}^{L_1L_3N} = \frac{A_1^{L_1L_3N}a_3}{A_3a_1} - (f_{12}f_{23} + f'_{13}). \quad (9)$$

The partial $f_{13}^{L_1L_3M}$ CK yield was determined from the M-satellite intensities employing the following formula:

$$f_{13}^{L_1L_3M} = \frac{A_1^{L_1L_3M}a_3}{A_3a_1}, \qquad (10)$$

where $A_1^{L_1L_3M} = f_{13}^{L_1L_3M}Ca_1\omega_{L\alpha M}$ is the fitting parameter for the $L\alpha M$ satellite fluorescence intensity $I_1^{L_1L_3M^{at}}(E)$. Only data for incident photon energies above 3618 eV were considered. The CK channel is fully open then and the M-satellite to diagram line intensity ratios normalized to the experimental photoionization cross section $\sigma_1(E)$ are constant (see Fig. 5). For beam energies in the

vicinity of the L_1-edge a smooth rise of the ratio with photon energy can be observed. This variation is mainly related to the finite lifetime of the L_1 vacancy state.

A similar method was applied to deduce the f_{12} yield, using the following formula:

$$f_{12} = \frac{A_1' a_2}{A_2' a_1}, \tag{11}$$

where $A_1' = f_{12} C' a_1 \omega_{L\beta}$ and $A_2' = C' a_2 \omega_{L\beta}$.

Further, to account for the differences in the fluorescence yields of the $L_3^{-1} \to M_{4,5}^{-1}$ diagram line and the $L_3^{-1} M_{4,5}^{-1} \to M_{4,5}^{-2}$ x-ray transition in the presence of an additional hole in the $M_{4,5}$ shell, the ratio $\omega_{L\alpha M}/\omega_{L\alpha}$ was estimated. The following relations based on a statistical weighting procedure similar to the one described in [32] were employed:

$$\omega_{L\alpha} = \frac{\Gamma_{L\alpha}}{\Gamma_3} \tag{12a}$$

$$\omega_{L\alpha M} = \frac{\frac{9}{10}\Gamma_{L\alpha}}{\Gamma_{L\beta} + \Gamma_{L\iota} + \Gamma^A_{L_3 M_{123} M_{123}} + \Gamma^A_{L_3 M_{123} N} + \frac{9}{10}(\Gamma_{L\alpha} + \frac{8}{9}\Gamma^A_{L_3 M_{45} M_{45}} + \Gamma^A_{L_3 M_{123} M_{45}} + \Gamma^A_{L_3 M_{45} N}) + \Gamma^A_{L_3 NN}}, \tag{12b}$$

where Γ_3 is the L_3-subshell total transition rate, $\Gamma_{L\alpha}$ the total $L\alpha$ x-ray emission rate, $\Gamma_{L\beta}$ the sum of the x-ray emission rates of the $L\beta_2$, $L\beta_6$ and $L\beta_{15}$ transitions, and Γ^A stands for the radiationless transition rates. In the calculation, the radiative transition rates $\Gamma_{L\alpha}$, $\Gamma_{L\beta}$ and $\Gamma_{L\iota}$ were taken from the theoretical calculations of Scofield [33], and the Auger probabilities were interpolated from the values quoted in Ref. [34] for Rh ($Z=45$) and Ag ($Z=47$). A $\omega_{L\alpha M}/\omega_{L\alpha}$ ratio of 1.014 was found. This value denotes a negligibly small difference between the $L\alpha$ and $L\alpha M$ satellite line fluorescence yields.

As already mentioned, N- and M-shell satellites are due not only to CK transitions, but may also originate from the shake process. In the shake process the primary electron is ejected rapidly and due to the sudden change of the central potential a subsequent excitation of a second electron to a bound state or to the continuum takes place. To delineate the role played by shake contributions to L x-ray fluorescence intensity changes, the shake probabilities for Pd were calculated in the framework of the sudden approximation model [35] using self-consistent Dirac-Fock wavefunctions from the code of [36]. More information on the calculations can be found in [37]. The calculated N-shake probability when a single vacancy is created in the L_i subshell was found to be $P_N=0.202$, where

for $N_{4,5}$ electrons $P_{N_{4,5}}$=0.184. For the M-shell, the shake probability of P_M=0.0088 for the initial single vacancy in the L_1 subshell, and P_M=0.0092 in the $L_{2,3}$ subshells, respectively, were obtained.

Although the shake probabilities of $N_{4,5}$ subshell electrons can reach as much as 18%, this contribution is constant over the whole range of incident photon energies and thus does not influence the L x-ray intensity jumps. Concerning the M-shake probability, according to the sudden approximation model the above calculated values are valid for primary photon energies higher than about 10 times the LM double ionization threshold, i.e., ∼6970 eV [38]. This means that, the relative satellite intensity due to M-shake events is even less than 1.8%, and thus is negligibly small. Indeed, the observed $L\alpha M$ satellites originate from the $L_1-L_3M_{4,5}$ CK transitions.

Fig. 6 shows the experimental values and fitted curves of the atom-like fluorescence intensities $I^{at}(E)$ given by:

$$I^{at}(E) = I_3^{at}(E) + I_2^{at}(E) + I_1^{at}(E), \quad (13)$$

where $I_1^{at}(E) = I_1^{L_1L_3N^{at}}(E) + I_1^{L_1L_3M^{at}}(E)$ stands for the atom-like fluorescence intensity due to a hole in the L_1 subshell. The fluorescence intensity jumps at the L-edges corresponding to the particular CK transi-
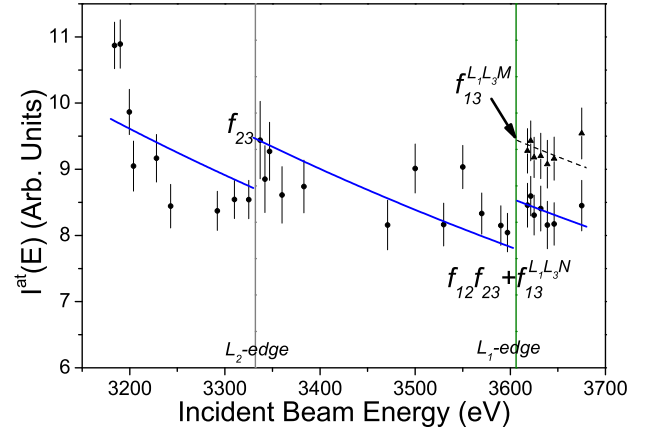

FIG. 6: (color online) Atom-like fluorescence intensities $I^{at}(E)$ plotted against the incident beam energy. Experimental points are depicted with solid circles, while the solid lines represent the fitted curves. The data set used to derive the partial Coster-Kronig yield $f_{13}^{L_1L_3M}$ is plotted separately (solid triangles), while the dashed line stands for the fitted values. The vertical lines indicate the L-edges.

tion yields are also depicted. For the f_{23} CK rate, a value of 0.164 ± 0.033 was calculated using Eq.(7). The partial CK yields of 0.324 ± 0.032 for $f_{13}^{L_1L_3N}$ and 0.406 ± 0.023 for $f_{13}^{L_1L_3M}$ were deduced adopting for the f_{12} yield the value of $0.047(1)$ from Eq.(11). This f_{12} rate is close to the value of $0.044(4)$ reported by Sorensen for Ag [9] and to the calculated prediction of 0.065 of Chen *et al.* [2] but smaller than the result of 0.1 reported by Krause [39]. The total CK probability $f_{13} = f_{13}^{L_1L_3N} + f_{13}^{L_1L_3M}$ amounts to 0.730 ± 0.039. It should be noted that since the competing intrashell radiative transitions are negligibly small compared to the CK pro-
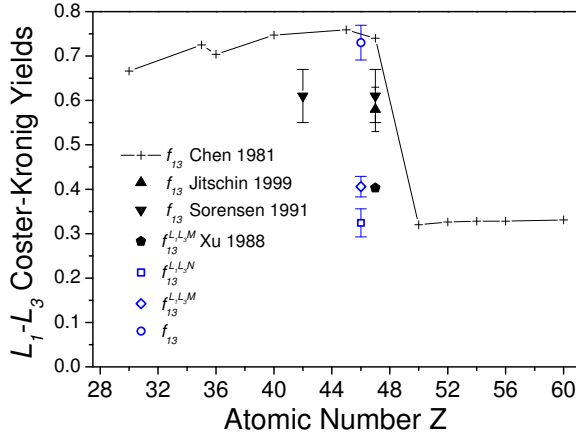
FIG. 7: (color online) Present f_{13} CK rates of Pd (open symbols) compared to theoretical values from [2] and available experimental data for neighboring elements, Mo [10] and Ag [8, 10, 40].

for Pd is found to be $\sim 20\%$ higher.

The f_{23} CK rate is consistent within the experimental uncertainty with the theoretical value from [2]. The present total CK probability f_{13} is also comparable with the calculations of Chen *et al.* [2], but the relative contributions of the $f_{13}^{L_1L_3N}$ and $f_{13}^{L_1L_3M}$ CK yields are quite different. In fact, the partial CK transition $L_1 - L_3N$ for Pd is close to the values of the semi-empirical fit of Krause [39] for elements in the range $50 \leq Z \leq 74$ for which the $L_1 - L_3M$ CK transitions are energetically forbidden [34].

cess [10], the value of f'_{13} was not taken into consideration in the calculations.

The present results together with the theoretical predictions are listed in Table II and the f_{13} CK probabilities are compiled in Fig. 7. In Table II, the CK yields calculated using the fitting parameters obtained from the interpolated photoabsorption coefficients of Ref. [18] are also presented. It can be seen that both sets of data agree quite well with each other. To the best of our knowledge, no other experimental data for the CK yields of Pd exist. Compared to the experimental values reported for Ag [8, 10], the total f_{13} rate

The discrepancies between the theoretical and experimental values can be partly ascribed to the overestimated theoretical $L_1 - L_3M$ transition rates. As already pointed out by Chen *et al.* [41] for the case of Ag, adjusting the $L_1 - L_3M_{4,5}$ rate by a factor 0.4 leads to a better agreement of the experimental and theoretical L_1 level widths. Indeed, for Pd the calculated L_1 width is 6.8 eV [2], while a value of 3.9 eV is recommended by Campbell and Papp [42]. We have therefore rescaled the theoretical CK transition width $\Gamma_{L_1L_3M}^{CK}$ using the following transformation:

$$\Gamma_1 = \Gamma_{tot}^A + \Gamma_{tot}^R = \frac{\Gamma_{tot}^A}{1 - \omega_1} \longrightarrow \Gamma_1^{exp} = \frac{\sum_{(-)} \Gamma^A + \Gamma_{L_1L_3N}^{CK} + \eta\Gamma_{L_1L_3M}^{CK}}{1 - \omega_1}, \qquad (14)$$

TABLE II: Coster-Kronig transition yields of palladium.

	f_{23}	f_{12}	f_{13}	$f_{13}^{L_1L_3N}$	$f_{13}^{L_1L_3M}$
Present	0.164(33)	0.047(1)	0.730(39)	0.324(32)	0.406(23)
Present[a]	0.130(30)	0.072(4)	0.743(45)	0.307(34)	0.436(29)
Theory[b]	0.154	0.065	0.75	0.095	0.655
Theory[c]	-	0.103	0.58	0.163	0.418
Ag [8]	0.18(3)	0.14(3)	0.58(5)		
Ag [9]	0.16(3)	0.044(4)	0.61(5)		
Ag Theory[b]	0.155	0.068	0.74	0.108	0.634
Ag Theory[c]	-	0.109	0.56	0.191	0.364

[a]These results were derived using the fitting parameters listed in the second column of Table I.
[b]Calculations by Chen *et al.* [2, 34].
[c]Calculations with adjusted $L_1 - L_3M$ transition rates (see text).

where Γ_1 and Γ_1^{exp} represent the theoretical and experimental widths of the atomic level L_1, Γ_{tot}^A and Γ_{tot}^R the sum of the widths of all Auger and radiative transitions decaying L_1-vacancy states, ω_1 the partial fluorescence yield of the L_1-subshell, $\sum_{(-)} \Gamma^A$ the total L_1 Auger width minus the widths of the $L_1 - L_3M$ and $L_1 - L_3N$ CK transitions, and η is a constant. The widths of the radiationless transitions were obtained from the Auger transition probabilities reported by Chen [34], whereas the width Γ_1 and fluorescence yield ω_1 were taken from Ref. [2] and the experimental width Γ_1^{exp} from Ref. [42]. The adjustment factor η can be deduced from (14):

$$\eta = \frac{(1 - \omega_1)\Gamma_1^{exp} - \sum_{(-)} \Gamma^A - \Gamma_{L_1L_3N}^{CK}}{\Gamma_{L_1L_3M}^{CK}}. \tag{15}$$

As Chen's calculations reported in [2, 34] concern only the neighbour elements Rh (Z=45) and Ag (Z=47), the factors η were first computed for these two elements. Values of 0.425 and 0.325, respectively, were obtained from which the factor η corresponding to Pd was then determined by interpolation. Finally, the adjusted CK yields f_{12}^{adj}, $f_{13}^{L_1L_3M,adj}$ and $f_{13}^{L_1L_3N,adj}$ given in Table II were calculated by means of the following relations:

$$f_{12}^{adj} = \frac{\Gamma_1}{\Gamma_1^{exp}} f_{12} \tag{16a}$$

$$f_{13}^{L_1L_3M,adj} = \frac{\eta \cdot \Gamma_1}{\Gamma_1^{exp}} f_{13}^{L_1L_3M} \tag{16b}$$

$$f_{13}^{L_1L_3N,adj} = \frac{\Gamma_1}{\Gamma_1^{exp}} f_{13}^{L_1L_3N}. \tag{16c}$$

As shown in Table II, the obtained $f_{13}^{L_1L_3M,adj}$ value is close to our experimental result, but the $f_{13}^{L_1L_3N,adj}$ rate is still a factor of two

smaller. This results in a twice as large experimental $L_1 - L_3N$ to $L_1 - L_3M$ CK yields ratio compared to the calculated one. A similar trend can be also observed for Ag. Calculations including many-body and solid-state effects for the radiative and nonradiative L_1-subshell decay rates and more experimental data in this Z region would certainly help to unravel the observed discrepancies.

The estimated uncertainties of the derived Pd CK yields of 10-25% stem mainly from the uncertainties of the fitting parameters A_i. With the current method the solid-state effects could be diminished to a large extent and the effect of the parameters b_i was found to be small. However, the differences between the experimental and relativistic Hartree-Slater (RHS) calculations, caused by the electron-correlation effects [17], can be as much as 3% below the L_2-edge and 4% above, respectively. These differences also affect the uncertainties of the $L\alpha$ intensities extracted from the extrapolation of the fitted photoionization cross sections beyond the individual L-subshell edges, in particular the L_3-edge. It should be also noted that numerical results of different theoretical predictions can vary up to 2% [43]. All of these effects can lead to uncertainties up to 30% for the CK yields [3].

V. CONCLUDING REMARKS

We have carried out the first determination of the Coster-Kronig transition yields for Pd via synchrotron-radiation-based high-resolution measurements of the L x-ray emission lines. By means of a fitting procedure making use of the power-law dependence of the photoionization cross sections on the primary photon energy, the f_{23} and f_{13} CK yields were derived from the relative $L\alpha$ intensity jumps at the L-edges, and the f_{12} rate from the $L\beta_1$ intensity jump at the L_1-edge. The measured L-edge x-ray absorption spectrum was compared to the theoretical cross sections and served to correct the L x-ray intensities for solid-state effects. Thanks to the resolved $L\alpha M$ satellite lines, the partial $L_1 - L_3M_{4,5}$ CK transition yield could be determined. The differences in the transition probabilities for the M-satellite lines and the parent diagram lines were accounted for. The sensitivity of the CK yields to the parametrization of the photoabsorption cross sections was also considered. Our result for the total f_{13} CK yield is consistent with the theoretical calculations of Chen *et al.* [2], however, the obtained value is higher compared to the experimental ones for neighboring elements.

The discrepancies between the present and theoretical values for the relative contribu-

tions of the partial $L_1 - L_3N$ and $L_1 - L_3M$ CK yields point to the need of including many-body and solid-state effects for the radiative and nonradiative L_1-subshell decay rates. While the total f_{13} Coster-Kronig yields are available, the experimental data for partial f_{13} CK transition rates are scarce or not existing. More experimental values obtained from measurements with the synchrotron radiation based high-resolution x-ray emission or Auger-electron spectroscopy techniques for the relative contributions of the partial $L_1 - L_3N$ and $L_1 - L_3M$ CK yields are called for.

---

[1] W. Bambynek, B. Crasemann, R. W. Fink, H.-U. Freund, H. Mark, C. D. Swift, R. E. Price, and P. V. Rao, Rev. Mod. Phys **44**, 716 (1972).

[2] M. H. Chen, B. Crasemann, and H. Mark, Phys. Rev. A **24**, 177 (1981).

[3] J. L. Campbell, At. Data Nucl. Data Tables **85**, 291 (2003).

[4] R. W. Dunford, E. P. Kanter, B. Krässig, S. H. Southworth, L. Young, P. H. Mokler, Th. Stöhlker, S. Cheng, A. G. Kochur, and I. D. Petrov, Phys. Rev. A **74**, 062502 (2006).

[5] J. L. Campbell, At. Data Nucl. Data Tables **95**, 115 (2009), and references therein.

[6] W. Jitschin, G. Materlik, U. Werner, and P. Funke, J. Phys. B **18**, 1139 (1985).

[7] U. Werner and W. Jitschin, Phys. Rev. A **38**, 4009 (1988).

[8] W. Jitschin, R. Stötzel, T. Papp, and M. Sarkar, Phys. Rev. A **59**, 3408 (1999).

[9] S. L. Sorensen, R. Carr, S. J. Schaphorst, S. B. Whitfield, and B. Crasemann, Phys. Rev. A **39**, 6241 (1989).

[10] S. L. Sorensen, S. J. Schaphorst, S. B. Whitfield, B. Crasemann, and R. Carr, Phys. Rev. A **44**, 350 (1991).

[11] S. Puri, D. Mehta, B. Chand, N. Singh, and P. N. Trehan, X-ray Spectrom. **22**, 358 (1993).

[12] B. L. Doyle and S. M. Shafroth, Phys. Rev. A **19**, 1433 (1979).

[13] E. Rosato, Nucl. Instrum. Methods Phys. Res. B **15**, 591 (1986).

[14] T. K. Sham, Phys. Rev. B **31**, 1888 (1985).

[15] L. C. Witjens, J. H. Bitter, A. J. van Dillen, K. P. de Jong, and F. M. F. de Groot, Phys. Chem. Chem. Phys. **6**, 3903 (2004).

[16] M. Czarnota, M. Pajek, D. Banás, J.-Cl. Dousse, Y.-P. Maillard, O. Mauron, P.-A. Raboud, M. Berset, D. Chmielewska, J. Rzadkiewicz, et al., Braz. J. Phys. **36**, 546 (2006).

[17] W. Jitschin and R. Stötzel, Phys. Rev. A

58, 1221 (1998).

[18] http://physics.nist.gov/xcom.

[19] M. Kavčič, A. G. Karydas, and Ch. Zarkadas, Nucl. Instrum. Methods Phys. Res. B **222**, 601 (2004).

[20] R. D. Deslattes, E. G. Jr. Kessler., P. Indelicato, L. de Billy, E. Lindroth, and J. Anton, Rev. Mod. Phys. **75**, 35 (2003).

[21] J. Hoszowska, J.-Cl. Dousse, J. Kern, and C. Rhême, Nucl. Instrum. Methods Phys. Res. A **376**, 129 (1996).

[22] T. Åberg, Phys. Rev. **156**, 35 (1967).

[23] K. Słabkowska and M. Polasik, Rad. Chem. Phys. **75**, 1471 (2006).

[24] M. A. MacDonald, S. H. Southworth, J. C. Levin, A. Henins, R. D. Deslattes, T. LeBrun, Y. Azuma, P. L. Cowan, and B. A. Karlin, Phys. Rev. A **51**, 3598 (1995).

[25] M. Žitnik, M. Kavčič, K. Bučar, A. Mihelič, M. Štuhec, J. Kokalj, and J. Szlachetko, Phys. Rev. A **76**, 032506 (2007).

[26] J. J. Rehr and R. C. Albers, Rev. Mod. Phys. **72**, 621 (2000).

[27] J. E. Müller and J. W. Wilkins, Phys. Rev. B **29**, 4331 (1984).

[28] http://cars9.uchicago.edu/∼ravel/software/exafs/.

[29] B. Ravel and M. Newville, Phys. Scr. T **115**, 1007 (2005).

[30] W. Jitschin, U. Werner, G. Materlik, and G. D. Doolen, Phys. Rev. A **35**, 5038 (1987).

[31] B. L. Henke, E. M. Gullikson, and J. C. Davis, At. Data Nucl. Data Tab. **54**, 181 (1993). Online calculations at http://henke.lbl.gov/optical_constants/.

[32] F. P. Larkins, J. Phys. B **4**, 1 (1971).

[33] J. H. Scofield, At. Data Nucl. Data Tables **14**, 121 (1974).

[34] M. H. Chen, B. Crasemann, and H. Mark, At. Data Nucl. Data Tables **24**, 13 (1979).

[35] T. Mukoyama and K. Taniguchi, Phys. Rev. A **36**, 693 (1987).

[36] K. G. Dyall, J. Phys. B **16**, 3137 (1983).

[37] J.-Cl. Dousse and J. Hoszowska, Phys. Rev. A **56**, 4517 (1997).

[38] T. D. Thomas, Phys. Rev. Lett. **52**, 417 (1984).

[39] M. O. Krause, J. Phys. Chem. Ref. Data **8**, 307 (1979).

[40] J. Q. Xu and E. Rosato, Phys. Rev. A **37**, 1946 (1988).

[41] M. H. Chen, B. Crasemann, M. Aoyagi, and H. Mark, Phys. Rev. A **15**, 2312 (1977).

[42] J. L. Campbell and T. Papp, At. Data Nucl. Data Tables **77**, 1 (2001).

[43] J. H. Hubbell, Phys. Med. Biol. **51**, R245 (2006).

Part 2.

Synchrotron-radiation-based determination of Xe

L-subshell Coster-Kronig yields:

A re-examination via high-resolution x-ray spectroscopy

W. Cao[1], J.-Cl. Dousse[1], J. Hoszowska[1], M. Žitnik[2], M. Kavčič[2], and K. Bučar[2]

[1] *Department of Physics, University of Fribourg, Ch. du Musée 3, Ch-1700 Fribourg, Switzerland*

[2] *J. Stefan Institute, P.O. Box 3000, SI-1001 Ljubljana, Slovenia*

I. INTRODUCTION

The decay scheme of atomic inner-shell vacancies is branched into cascades of radiative and non-radiative-Auger transitions. The Coster-Kronig (CK) transitions are the fastest Auger transitions, in which the vacancy transfers within the same major shell. The vacancy transfer probability from the i subshell to the higher j subshell is called the CK yield f_{ij}. CK rates depend on the initial- and final-state wave functions and are very sensitive to electron binding energies as well as to solid-state effects [1, 2].

Particularly interesting is the region around $Z = 48$ where a sharp decrease in the f_{13} value is expected due to the $L_1 - L_3M_{4,5}$ transitions becoming energetically forbidden. Large discrepancies between the theoretical [2, 3] and existing experimental results [4, 5] point out the need for new accurate data. Experimental determination of the L-shell CK yields presents, however, considerable difficulties. For this reason, data are scarce and often suffer from large uncertainties [6]. To date, to determine the f_{23} yields, mostly the $K\alpha$-L x-ray coincidence method [6, 7] was used. This technique, however, fails in the case of the L_1-subshell CK yields due to the dipole forbidden $K - L_1$ radiative transition. The alternative photoionization experimental method was limited to the use of radionuclides [8].

The subshell-selective photoionization method based on energy-tunable monochromatic synchrotron radiation [9] offers the possiblity to measure all L-subshell CK yields. This method has been successfully applied to determine CK yields for solids [9–13] as well as for Xe [14]. So far, most measurements of the x-ray fluorescence lines were performed by means of energy-dispersive semiconductor detectors. In our recent work on Pd ($Z = 46$) [15], the subshell-selective photoionization method was combined with high-resolution x-ray spectroscopy, allowing even the partial $L_1 - L_3M_{4,5}$ CK yield to be deduced. By applying this technique to elements within the mid-Z region it would certainly be possible to reveal the L_1 CK yield cutoff trend.

In this paper, we report on the revisit of the L-subshell f_{23}, f_{13} and f_{12} Coster-Kronig yields for xenon ($Z = 54$) via the synchrotron-radiation-based high-resolution x-ray spectroscopy technique. The individual L-subshell photoionization cross sections were determined from the measured x-ray-absorption spectrum. The measurements of the $L\alpha_{1,2}$ ($L_3 - M_{4,5}$) and $L\beta_1$ ($L_2 - M_4$) lines were carried out by means of a high-resolution Johansson-type crystal x-ray spectrometer. The CK yields were derived from

the variation of the $L\alpha_{1,2}$ and $L\beta_1$ fluorescence line intensities at the absorption L edges due to the onsets of CK vacancy transfers. In addition, the L_1-subshell fluorescence yield ω_1 was also determined from intensity ratios of the well resolved $L\beta_4$ and $L\beta_1$ lines.

II.   EXPERIMENT

The measurements were performed at the x-ray absorption fine structure (XAFS) beamline of Elettra synchrotron in Trieste, Italy, employing the JSI x-ray spectrometer [16]. The primary x-ray beam was monochromatized by means of a double-crystal Si(111) monochromator and higher harmonics were reduced with a Pt-coated mirror. The photon flux incident on the Xe sample was $\sim 10^{10}$ photons/s. The Xe gas was contained in a 10 mm long stainless steel cell sealed with 12.5 μm thick Kapton$^{\mathrm{TM}}$ foils. Two ionization chambers, one in front and one after the spectrometer, were used for the absorption measurements and also for normalization purposes. The experimental setup was similar to the one described in [17].

For the absorption measurement, the Xe gas pressure was kept at a nominal value of 500 mbar. In order to obtain both a high enough photon beam transmission and detector efficiency, the percentages and pressures of the helium-nitrogen gas mixtures for each of the ionization chambers were optimized. The photon energy was tuned with 0.2 eV steps in the range from 4500 to 5800 eV. Another scan over the same energy range was performed with an empty target cell in order to determine the residual attenuation in the Kapton$^{\mathrm{TM}}$ windows and in the ionization chambers. For the fluorescence measurements, the Xe gas pressure was 200 mbar.

The L x-ray fluorescence lines of Xe were measured at an angle of 90° with respect to the horizontally polarized incident photon beam. A cylindrically curved quartz $(10\bar{1}0)$ crystal in the second order of reflection was employed. The diffracted x rays were recorded with a thermoelectrically cooled (-40 ^{o}C) back-illuminated charge coupled device (CCD) camera consisting of 770×1153 pixels with a pixel size of 22.5×22.5 μm^2. The x-ray spectrometer energy resolution was about 0.2 eV. For normalization purposes, the incident photon flux was recorded online with the first ionization chamber each 10 s. Beam intensities were corrected for absorption in the ionization chamber and the Kapton$^{\mathrm{TM}}$ windows in the beam path.

The fluorescence spectra were calibrated using the reference energies of the $L\alpha_1$ (or $L\beta_1$) x-ray line reported in Ref.[18]. Depending on the incident photon energy and the total photon number, the time to collect an L x-ray spectrum varied from 50 to 170 min.

A series of 14 $L\alpha$ and another series of 7 $L\beta_1$ x-ray emission spectra were recorded. The incident-beam energy was tuned from 4850 eV (68 eV above the L_3-edge E_3) to 5700 eV (247 eV above the L_1-edge E_1) for the measurements of the $L\alpha$ lines, and from 5200 eV (96 eV above the L_2-edge E_2) to 5750 eV (297 eV above E_1) for the $L\beta_1$ and $L\beta_4$ lines.

III. DATA ANALYSIS

A. Spectra fitting

The Xe $L\alpha$ and $L\beta_1$ x-ray spectra measured at two different photon energies are shown in Fig. 1 and Fig. 2, respectively. It can be seen that the high-resolution x-ray emission spectroscopy employed in our work permits to resolve the individual $L\alpha$ (or $L\beta$) x-ray transitions, thus avoiding an elaborate fitting procedure such as is needed in the case of L-x-ray spectra measured with energy dispersive detectors [13]. In inner-shell photoionization, however, the diagram transitions may be accompanied by satellite lines resulting from additional vacancies present in outer-subshells via Coster-Kronig and shake [19] processes. Due to the reduced screening of the nuclear charge, the x-ray satellite lines are shifted in energy with respect to the diagram transitions.

Multiconfiguration Dirac-Fock (MCDF) calculations [20] show that the first-order N- and O-satellites are not resolved from the $L\alpha$ and $L\beta_1$ parent lines. This overlap of the LN and LO satellite transitions with the parent diagram lines results in a non-lifetime broadening of the latter. Our calculations, performed within the framework of the sudden approximation model using self-consistent Dirac-Fock wave functions from the code of reference [20], predict for the O-shake probability a value of 0.14 and for the N-shake 0.05. Although the O-shell electron shake contribution is non negligible, the fluorescence intensity jumps are not affected because it is constant over the measured photon energy range. The same holds for the N-shell shake contribution. For incident beam energies tuned above the L_1-edge, the opening of the $L_1 - L_3N$ CK channel results in an asymmetry on the high-energy flank of the $L\alpha_1$ line (see Fig. 1(b)). The $L\alpha M$ satellite transitions, expected at $\sim$13 eV above the $L\alpha_1$ line, were not observed. This is not surprising because the $L_1 - L_3M$ CK transitions are energetically forbidden and the M-shake probability of 0.006 is negligibly small.

Taking the above considerations into account, each $L\alpha_{1,2}$ line was fitted by two Lorentzians with widths as free parameters. Above the L_1-edge an additional Lorentzian profile was needed to account for the $L\alpha_1N$ satellite contribution. For the $L\beta_1$ line as well
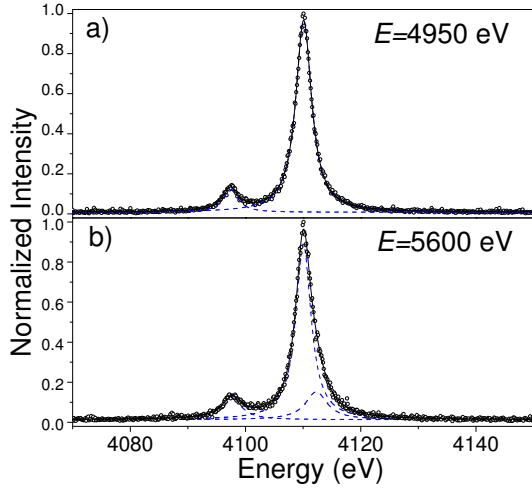
tion $\mu(E)b$, where b stands for the interaction

FIG. 1: (Color online) Fitted high-resolution $L\alpha$ x-ray spectra of Xe at different incident-beam energies, (a) E =4950 eV and (b) E=5600 eV. Solid thick lines represent the total fit to the experimental data (dots) and dashed lines the individual components.
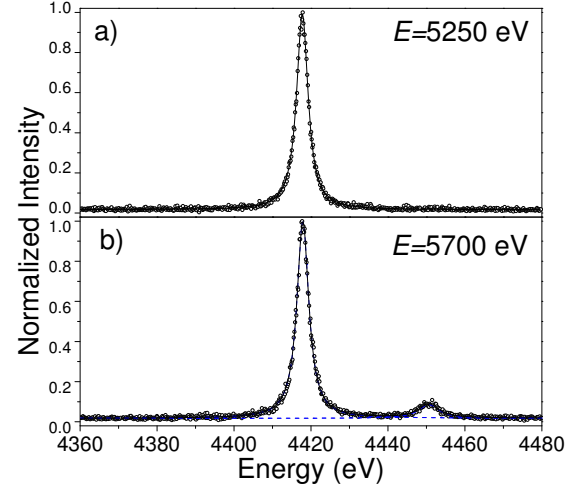

FIG. 2: (Color online) Fitted high-resolution $L\beta_1$ ($L_2 - M_4$) x-ray spectra of Xe at different incident-beam energies, (a) E =5250 eV and (b) E=5700 eV. Solid thick lines represent the total fit to the experimental data (open circles) and dashed lines the individual components. In (b), the peak on the high energy side of the $L\beta_1$ line corresponds to the $L\beta_4$ ($L_1 - M_2$) transition.

as for the $L\beta_4$ (L_1-M_2) line observed for photon impact energies tuned above the L_1 edge (see Fig. 2(b)), a single Lorentzian profile was used because the $L_1 - L_2N$ CK transitions are very weak. The fitted L x-ray intensities were normalized to the same incident photon flux and data acquisition time. In addition, each spectrum collected at an incident energy E was weighted by the corresponding beam-absorption correction factor

$$F_{corr}(E) = \frac{\mu(E)b}{1 - \exp[-\mu(E)b]}, \qquad (1)$$

which is valid for a perpendicular experimental geometry [21]. The total attenua-

path, was measured at a target gas pressure of 200 mbar in the beam energy range 4500 eV $\leq$E$\leq$ 5800 eV with 1 eV steps.

B. *L*-subshell cross section parametrization

The experimental $L\alpha$ fluorescence intensity $I(E)$ is proportional to the total L x-ray production cross section

$$\sigma_{L\alpha}^X(E) = \omega_{L\alpha}[\sigma_3(E) + f_{23}\sigma_2(E) + (f_{13} + f_{12}f_{23} + f'_{13})\sigma_1(E)], \qquad (2)$$

where $\sigma_i(E)$ are the L_i (i=1,2 or 3) sub-shell photoionization cross sections and f'_{13} denotes the L_1 to L_3 hole transfer rate resulting from the $L_1 - L_3$ radiative transition. The $\omega_{L\alpha}$ stands for the $L\alpha$ diagram line fluorescence yield. Similarly, the $L\beta_1$ and the $L\beta_4$ x-ray production cross sections are

$$\sigma_{L\beta_1}^X(E) = \frac{\Gamma_{L\beta_1}}{\Gamma_2}[\sigma_2(E) + f_{12}\sigma_1(E)], \qquad (3)$$

and

$$\sigma_{L\beta_4}^X(E) = \frac{\Gamma_{L\beta_4}}{\Gamma_1}\sigma_1(E) = \frac{\Gamma_{L\beta_4}}{\Gamma_1^{rad}}\omega_1\sigma_1(E), \quad (4)$$

respectively. $\Gamma_{L\beta_1}$ and $\Gamma_{L\beta_4}$ represent the fluorescence widths of the two transitions, Γ_1 and Γ_2 the total widths of the L_1 and L_2 subshells, and Γ_1^{rad} the radiative width of the L_1 subshell.

In order to derive the CK yields from the measured L x-ray fluorescence intensities, the variation of the photoionization cross sections with photon energy should be known. It is generally assumed that within a certain energy range the cross sections vary smoothly with photon energy and the dependence can be described by a power-law. According to the independent particle approximation (IPA) calculations, the single L_i-

TABLE I: The fitting parameters for the power-law dependence of the L_i-subshell ($i = 3, 2, 1$) photoionization cross sections.

Parameter	i		
	3	2	1
a_i (Mbarn)	7.640	4.076	-
a_i [14](Mbarn)	7.818	3.716	0.467
b_i [14]	-2.753	-2.654	-1.765

subshell photoionization cross section σ_i for Xe can be expressed as

$$\sigma_i(E) = a_i E^{b_i}, \qquad (5)$$

where a_i is in the unit of Mbarn and E in keV.

The Xe L-shell photoionization cross sections are shown in Fig. 3. Because the temperature and pressure of Xe in the gas cell could not be determined accurately, the measured Xe L-edge absorption spectrum was normalized to the L_3-pre-edge x-ray absorption coefficients reported by Wuilleumier [22]. The L_3-pre-edge attenuation coefficients were fitted with the power-law and extrapolated in order to get the total L-shell photoionization cross section.

Below the L_2 edge, the L_3-subshell ionization cross section is given by the measured total L-shell photoionization cross section. The

latter is depicted by circles in Fig. 3 and compared to the power-law dependence of Jitschin *et al.* [14] shown by the dashed line. Obvious deviations of our experimental values from those based on the IPA calculations are observed. These differences could be due to many-body and multi-ionization effects. However, in the region slightly below the L_2 edge, the slopes of our experimental and IPA theoretical curves match each other quite well. Thus, adopting for the parameter b_3 the value of Jitschin *et al.* [14], the curve given by Eq. (5) was just scaled down to match the experimental points before the L_2 edge. Above the L_2 edge, the rescaled power-law curve was used to extrapolate the L_3-subshell cross section which was then subtracted from the experimental values to get the L_2 and L_2- plus L_1-subshell cross sections for incident beam energies $E_2 < E < E_1$ and $E > E_1$, respectively. Similarly, the L_1-subshell cross section was obtained by subtracting the extrapolated values from the rescaled power-law curve for the L_2-subshell cross section. The parameters a_i of the rescaled extrapolation curves together with the parameters a_i and b_i of Jitschin *et al.* [14] are listed in Table I. The fitted curves are depicted with solid lines in Fig. 3.
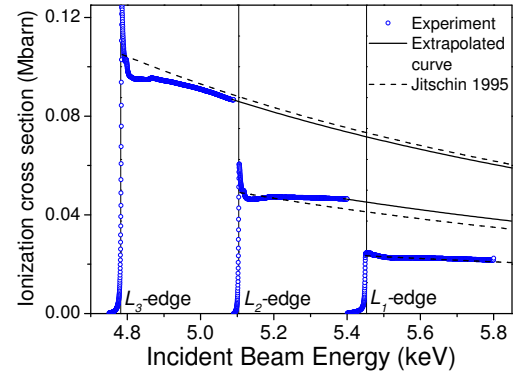

FIG. 3: (Color online) Experimental and theoretical L-subshell photoionization cross sections of Xe. The solid lines are the extrapolated curves obtained by scaling the analytical expression given by Eq.(5) to the measured values (open circles). The dashed lines are the theoretical values given by Jitschin *et al.* [14].

IV. RESULTS AND DISCUSSION

The method used to get the CK yields for Xe is similar to the one reported in our previous work [15]. The f_{23} CK yield was extracted from the $L\alpha$ intensity jump at the L_2 edge. First, the fluorescence intensity below the L_2 edge was fitted with the following expression

$$I_3(E) = C\omega_{L\alpha}\sigma_3(E), \qquad (6)$$

where C is the instrumental proportionality constant. From the fit the parameter $A_3 = C\omega_{L\alpha}$ was obtained. To derive the CK contribution, the fluorescence intensities $I_3(E)$ for energies above the L_2 edge were extrapolated and subtracted from the $I(E)$

data. For incident beam energies between the L_2 and L_1 edges, the values

$$I_2(E) = I(E) - I_3(E) \tag{7}$$

correspond to the additional fluorescence intensities due to the $L_2 - L_3$ CK process. From the fit of $I_2(E)$, the parameter $A_2 = f_{23} C \omega_{L\alpha}$ was obtained. Finally, the f_{23} CK rate was derived from the ratio of A_2 to A_3:

$$f_{23} = \frac{A_2}{A_3}. \tag{8}$$

Similarly, the f_{13} CK yield can be expressed as

$$f_{13} = \frac{A_1}{A_3} - f_{12}f_{23}, \tag{9}$$

where the f_{12} yield is given by the $L\beta_1$ intensity jump at the L_1 edge:

$$f_{12} = \frac{A_1'}{A_2'}. \tag{10}$$

Here, A' is introduced to distinguish the $L\alpha$ and $L\beta_1$ intensities. The fitting parameters for the $L\beta_1$ line intensities are $A_2' = C'\omega_{L\beta_1}$ and $A_1' = f_{12}C'\omega_{L\beta_1}$, where the instrumental proportionality constant is C' due to the changes of the crystal and detector positions, etc. The term f_{13}' is omitted in Eq. (9) because the competing intrashell radiative transition $L_1 - L_3$ is negligibly weak compared to the CK process [12].

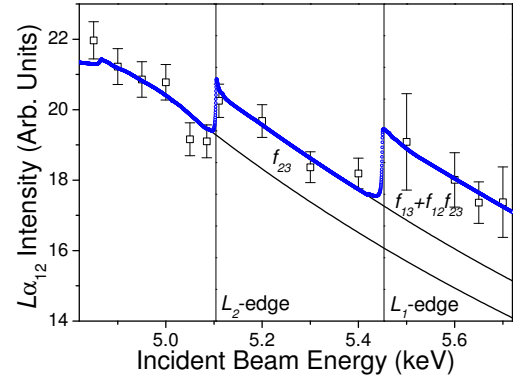Results of the fitting procedure for the $L\alpha$

FIG. 4: (Color online) The $L\alpha_{1,2}$ x-ray fluorescence intensities (open squares) fitted with the measured photoionization cross sections (open circles). The solid lines show the corresponding extrapolated power-law curves.

intensities are presented in Fig. 4. Values of 0.118 ± 0.029, 0.383 ± 0.037 and 0.096 ± 0.016 were found for the f_{23}, f_{13} and f_{12} Coster-Kronig yields, respectively. They are listed in the first row of Table II. For comparison, CK yields adopted in the former work [14] are listed in the second row. The theoretical predictions given by Chen *et al.* [2], the values recommended by Campbell [6] and the semi-empirical values reported by Krause [23] are also quoted. Our data for the f_{12} and f_{23} are in general smaller than the values from theoretical and semi-empirical predictions, but are consistent with the values adopted by Jitschin *et al.* [14]. For the f_{13} CK rate, however, the listed values in Table II differ: the present value is closer to the one reported by Chen *et al.* [2], while the result

from the work of Ref.[14] is closer to the one by Campbell [6]. To make a detailed comparison with the former work of Jitschin *et al.* [14], data with and without electron correlation corrections [14] are also presented in the table. The current value for f_{13} is found to be closer to the result obtained in [14] from the IPA fit, but much larger than the one with correlation corrections.

In order to get a more general view of the Z-dependence for the f_{13} yield in this Z region, the f_{13} CK probabilities for Xe and the existing experimental results for neigbouring elements Mo ($Z = 42$) [12], Pd ($Z = 46$) [15], Ag ($Z = 47$) [12, 24], and the recent results for Ba ($Z = 56$) [25] and La ($Z = 57$) [26] are compiled in Fig. 5. It can be seen that the present result is in reasonable agreement with values for higher Z elements (Ba and La) and also with the partial $L_1 - L_3N$ yield for Pd.

Differences among the f_{13} CK yield values can be attributed mainly to the determination of the L_i-subshell photoionization cross sections. Limitations of the IPA model can be clearly seen in Fig. 3. The discrepancies between the IPA model and the fit to the present experimental data could be due to multiple ionization processes [27, 28], electron correlation effects [29, 30], quantum interferences between one and two electron excitation processes [31], or the dynamic screen-
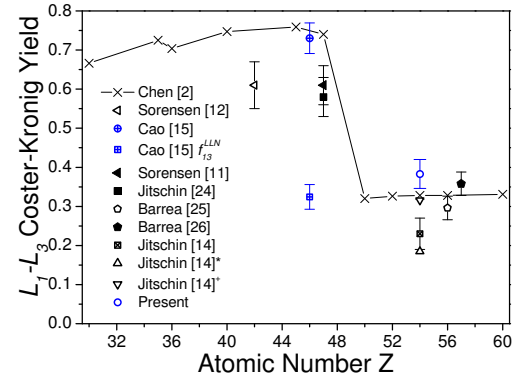

FIG. 5: (Color online) Present f_{13} CK rate of Xe (open circle). The datum is compared to theoretical values from [2], the available experimental data for the neighboring elements, Mo [12], Pd [15], Ag [11, 24], Ba [25], La [26], and for Xe [14] to the adopted value, as well as to values with (*) and without (+) electron correlation corrections. The f_{13}^{LLN} denotes the Pd partial $L_1 - L_3N$ CK yield obtained in [15].

ing effects [32]. Calculations including these effects could lead to a more precise total L-shell photoionization cross section. This is an issue still under debate [33] which is, however, beyond the scope of the present work.

When the energy of the photon beam is tuned above the L_1 edge, both $L\beta_1$ and $L\beta_4$ transitions are observed in the measured spectrum (see Fig. 2(b)). The intensity ratio of these two close lying lines can be accurately calculated, giving the possibility to determine the ω_1 fluorescence yield. This method is straightforward and free from elaborate spectrometer efficiency corrections [7, 34]. Using Eq. (3) and Eq. (4), the L_1-

TABLE II: Coster-Kronig rates and the L_1 fluorescence yield for Xe.

	f_{23}	f_{13}	f_{12}	ω_1
Present	0.118(29)	0.383(37)	0.096(16)	0.059(2)
Jitschin [14]	0.14(2)	0.23(4)	0.12(3)	-
Chen [2]	0.174	0.328	0.196	0.048
Campbell [6]	0.159(40)	0.25(8)	-	-
Krause [23]	0.154(31)	0.28(4)	0.19(4)	0.046(9)
Jitschin [14]*	0.115	0.185	0.095	-
Jitschin [14]+	0.174	0.316	0.169	-

* Results with electron correlation corrections
+ Results without electron correlation corrections

subshell fluorescence yield is given by

$$\omega_1 = \frac{I_{L\beta_4}}{I_{L\beta_1}} \frac{\Gamma_{L\beta_1}}{\Gamma_{L\beta_4}} \frac{\Gamma_1^{rad}}{\Gamma_2} \frac{[f_{12}\sigma_1(E) + \sigma_2(E)]}{\sigma_1(E)}. \quad (11)$$

By adopting for $\Gamma_{L\beta_1}$ and $\Gamma_{L\beta_4}$ the interpolated values of Campbell and Wang [35], and for the Γ_1^{rad} and Γ_2 the calculations of Chen *et al.* [2], ω_1 was found to be 0.059 ± 0.002. This result is higher than the theoretical predictions of Chen *et al.* [2] and Krause [23], and smaller than the value of 0.068 ± 0.007 determined for Ba ($Z = 56$) [25].

V.   CONCLUSION

We have determined the Coster-Kronig transition yields for Xe via synchrotron-radiation-based high-resolution measurements of the L x-ray emission lines. By making use of the measured L-subshell photoionization cross sections and the power-law dependence of the photoionization cross sections on the primary photon energy, the

f_{23} and f_{13} CK yields were derived from the relative $L\alpha$ intensity jumps at the L edges, and the f_{12} rate from the $L\beta_1$ intensity jump at the L_1 edge. From the intensity ratios of the $L\beta_4$ and the $L\beta_1$ lines, the fluorescence yield of the L_1-subshell was also determined.

Present results for the f_{12} and f_{23} CK yields were found to be consistent with those of Jitschin *et al.* [14], whereas for the f_{13} rate a higher value was obtained. The discrepancy was mainly attributed to the different parametrization of the L_i photoionization cross sections and, in particular, to the limitations of the IPA model used by Jitschin *et al.*. Indeed, the multiple electron excitation, many-body and time-dependent effects, which are implicitly included in our measured photoionization cross sections, were neglected in the IPA theoretical predictions. To further reduce the uncertainty of the CK values, more elaborate calculations would be needed. Experimentally, coincidence mea-

surements between the CK electron and the photon or Auger electron emitted in the subsequent decay would allow to separate the L_3 and L_2 photoionization cross sections above the L_2 and L_1 thresholds, respectively.

---

[1] W. Bambynek, B. Crasemann, R. W. Fink, H.-U. Freund, H. Mark, C. D. Swift, R. E. Price, and P. V. Rao, Rev. Mod. Phys **44**, 716 (1972).

[2] M. H. Chen, B. Crasemann, and H. Mark, Phys. Rev. A **24**, 177 (1981).

[3] S. Puri, D. Mehta, B. Chand, N. Singh, and P. N. Trehan, X-ray Spectrom. **22**, 358 (1993).

[4] B. L. Doyle and S. M. Shafroth, Phys. Rev. A **19**, 1433 (1979).

[5] E. Rosato, Nucl. Instrum. Methods Phys. Res. B **15**, 591 (1986).

[6] J. L. Campbell, At. Data Nucl. Data Tables **85**, 291 (2003).

[7] R. W. Dunford, E. P. Kanter, B. Krässig, S. H. Southworth, L. Young, P. H. Mokler, Th. Stöhlker, S. Cheng, A. G. Kochur, and I. D. Petrov, Phys. Rev. A **74**, 062502 (2006).

[8] J. L. Campbell, At. Data Nucl. Data Tables **95**, 115 (2009), and references therein.

[9] W. Jitschin, G. Materlik, U. Werner, and P. Funke, J. Phys. B **18**, 1139 (1985).

[10] U. Werner and W. Jitschin, Phys. Rev. A **38**, 4009 (1988).

[11] S. L. Sorensen, R. Carr, S. J. Schaphorst, S. B. Whitfield, and B. Crasemann, Phys. Rev. A **39**, 6241 (1989).

[12] S. L. Sorensen, S. J. Schaphorst, S. B. Whitfield, B. Crasemann, and R. Carr, Phys. Rev. A **44**, 350 (1991).

[13] R. A. Barrea, C. A. Pérez, and J. Sánchez, J. Phys. B: At. Mol. Opt. Phys. **35**, 3167 (2002).

[14] W. Jitschin, R. Stötzel, T. Papp, M. Sarkar, and G. D. Doolen, Phys. Rev. A **52**, 977 (1995).

[15] W. Cao, J. Hoszowska, J.-Cl. Dousse, Y. Kayser, M. Kavčič, M. Žitnik, K. Bučar, A. Mihelič, J. Szlachetko, and K. Słabkowska, Phys. Rev. A **80**, 012512 (2009).

[16] M. Kavčič, A. G. Karydas, and Ch. Zarkadas, Nucl. Instrum. Methods Phys. Res. B **222**, 601 (2004).

[17] M. Žitnik, M. Kavčič, K. Bučar, A. Mihelič, M. Štuhec, J. Kokalj, and J. Szlachetko, Phys. Rev. A **76**, 032506 (2007).

[18] R. D. Deslattes, E. G. Jr. Kessler, P. Indelicato, L. de Billy, E. Lindroth, and J. Anton, Rev. Mod. Phys. **75**, 35 (2003).

[19] T. Åberg, Phys. Rev. **156**, 35 (1967).

[20] K. G. Dyall, I. P. Grant, C. T. Johnson, F. A. Parpia, and E. P. Plummer, Comp. Phys. Comm. **55**, 425 (1989).

[21] F. Gel'mukhanov and H. Ågren, Phys. Rep. **312**, 87 (1999).

[22] F. Wuilleumier, Phys. Rev. A **6**, 2067 (1972).

[23] M. O. Krause, J. Phys. Chem. Ref. Data **8**, 307 (1979).

[24] W. Jitschin, R. Stötzel, T. Papp, and M. Sarkar, Phys. Rev. A **59**, 3408 (1999).

[25] R. A. Barrea, C. A. Pérez, and J. Sánchez, Nucl. Instrum. Methods Phys. Res. B **215**, 308 (2004).

[26] R. A. Barrea, C. A. Pérez, and J. Sánchez, Spectrochem. Acta B **58**, 51 (2003).

[27] I. Arčon, A. Kodre, M. Štuhec, D. Glavič-Cindro, and W. Drube, Phys. Rev. A **51**, 147 (1995).

[28] Y. Ito, A. M. Vlaicu, T. Tochio, T. Mukoyama, M. Takahashi, S. Emura, and Y. Azuma, Phys. Rev. A **57**, 873 (1998).

[29] W. Jitschin and R. Stötzel, Phys. Rev. A **58**, 1221 (1998).

[30] A. Zangwill and P. Soven, Phys. Rev. A **21**, 1561 (1980).

[31] K. Zhang, E. A. Stern, J. J. Rehr, and F. Ellis, Phys. Rev. B **44**, 2030 (1991).

[32] A. L. Ankudinov, A. I. Nesvizhskii, and J. J. Rehr, Phys. Rev. B **67**, 115120 (2003).

[33] S. Botti, A. Schindlmayr, R. Del Sole, and L. Reining, Rep. Prog. Phys. **70**, 357 (2007).

[34] T. Papp, J. L. Campbell, and S. Raman, Phys. Rev. A **49**, 770 (1994).

[35] J. L. Campbell and J.-X. Wang, At. Data Nucl. Data Tables **43**, 281 (1990).

Part 3.

Double L_3M ionization of Pd induced by impact

with medium-energy electrons

W. Cao[1], J.-Cl. Dousse[1], J. Hoszowska[1], M. Kavčič[2], Y. Kayser[1], J.-L. Schenker[1],
and M. Žitnik[2]

[1] *Department of Physics, University of Fribourg, Ch. du Musée 3, Ch-1700 Fribourg,
Switzerland*

[2] *J. Stefan Institute, P.O. Box 3000, SI-1001 Ljubljana, Slovenia*

I. INTRODUCTION

The electron-induced double ionization (DI) of neutral atoms may result from direct mechanisms for the ejection of two electrons without any internal atomic rearrangement, or indirect mechanisms in which the ejection of a single inner-shell electron is followed by an Auger decay. Direct mechanisms can be subdivided into shake [1] and so-called two-step-one (TS1), and two-step-two (TS2) processes [2]. Shake results from the sudden change in the atomic potential as a consequence of an inner-shell ionization or nuclear decay, whereas the TS1 process describes the knock out (KO) of a second bound electron by the first ionized electron and the TS2 process corresponds to the knock-out of two electrons from the same atom by a single incoming electron.

TS processes are important because they result from electron-electron interactions and permit therefore to investigate electron correlation effects. A straightforward method to study the TS processes is provided by $(e, 3e)$ experiments [3–5]. An alternative experimental approach consists to observe by means of high-resolution spectroscopy the radiative decay of atoms doubly ionized by electron impact. The latter method was used for instance by Mauron and Dousse [6]. In this study the double KL ionization induced in

several light atoms by low-energy electrons was determined as a function of the incident electron energy. The energy dependent double ionization cross sections (DICSs) were derived from the measured intensity ratios $I_{K\alpha L^{(1)}} : I_{K\alpha L^{(0)}}$ of the resolved L-satellite-to-parent-diagram x-ray lines, using available experimental values for the electron-induced single K-shell ionization cross sections.

The determination of two-step L_3M DICSs of mid-Z elements by means of the second experimental approach is, however, quite challenging for the following reasons. First, experimental data for the L-subshell electron-induced single ionization cross sections (EIICSs) are scarce and suffer of large uncertainties [7]. Many theoretical predictions for the EIICSs are also questionable. For instance, those from [8] and [9] are in good overall agreement with the recent experimental values of [10], but they poorly reproduce the experimentally observed energy dependencies of the cross sections, especially for energies close to the ionization thresholds [10]. Secondly, the use of the satellite-to-diagram line ratio method requires that the M-satellite lines are well resolved from their parent diagram lines, which is not an easy task. According to multi-configuration Dirac-Fock (MCDF) calculations [11, 12], for mid-heavy elements the average energy shift of the $L\alpha M$-satellites with respect to the par-

ent $L\alpha$ diagram line is indeed only ~ 10 eV. Low-resolution detectors are unable to resolve such close lying satellite lines and the use of crystal spectrometers is thus mandatory. However, the latter suffer from a poor efficiency as compared to low-resolution detectors, which makes the measurements more difficult and time consuming. Last but not least, $L_{1,2} - L_3M$ Coster-Kronig (CK) transitions, if energetically allowed, contribute significantly to the observed L_3M double ionization and the measured $L\alpha M$ to $L\alpha_{1,2}$ intensity ratios have to be corrected to account for this indirect DI contribution. Therefore, for the determination of the TS cross sections via the satellite-to-diagram line intensity ratio method, reliable CK probabilities are needed.

Analytical expressions for the EIICSs based on the distorted-wave Born approximation (DWBA) [13] were published recently [14]. The theoretical values obtained from these analytical expressions were found to be in good agreement with the experimental cross sections reported for the L subshells in [15] and to provide reliable results even for energies close to the ionization thresholds. On the other hand, a precise value was obtained lately for the $L_1 - L_3M_{4,5}$ CK yield of Pd by means of synchrotron-radiation-based high-resolution x-ray spectroscopy [16]. Hence Pd was chosen in the present work to investigate the contribution of TS processes to the electron-induced L_3M double ionization of mid-Z elements.

II. EXPERIMENT

The experiment was performed at the Physics Department of the University of Fribourg, employing a high-resolution reflecting-type von Hamos curved crystal spectrometer [17] for the measurements of the target x-ray emission. The sample fluorescence was produced by bombarding the Pd target with the beam from an energy-tunable thermo-ionic electron gun. The latter was equipped with a Ta disk cathode and electrostatic focusing and deflection electrodes. With this cathode, the electron gun can be operated safely at a pressure of 10^{-6} mbar which corresponds to the vacuum in the spectrometer chamber for standard operation. The accelerating voltage can be varied from 50 V to 20 kV, with a precision of 1 V. The beam current is independently adjustable from 1 μA to 1 mA. Thanks to a feedback stabilized emission current control, the relative stability of the electron beam intensity is better than 0.1%.

A top view of the experimental setup is depicted in Fig. 1. As shown, the electron beam was perpendicular to the crystal and detector translation axes which are both par-

allel to the dispersion direction of the spectrometer. The Pd target consisted of a thick metallic foil. It was positioned so that the angle δ between the normal to the foil and the beam direction was 29.6°. The exit angle of the x-rays relatively to the normal to the sample surface was thus $\kappa = \pi/2 - \delta - \theta$, where θ stands for the Bragg angle. To avoid that the foil melts as a result of the heatload due to the electron bombardment, a rather large thickness of 114 μm was chosen. The von Hamos spectrometer was operated in the so-called slit geometry. In this geometry, the target is viewed by the crystal through a narrow slit which is located on the translation axis of the detector and serves as the effective source of x-ray radiation. For this experiment, a slit width of 0.2 mm was adopted as the best compromise between a high enough energy resolution and an acceptable spectrometer luminosity. Furthermore, to reduce the background a cylindrical collimator was installed between the electron gun and the target and the spectrometer slit was covered with a ∼20 μm thick Be window. The fluorescence x rays from the target were diffracted in first order by a 10 cm high × 5 cm long × 0.15 mm thick quartz ($1\bar{1}0$) crystal plate bent cylindrically to a radius of 25.4 cm. The diffracted x rays were recorded by a thermoelectrically cooled (-40°C) back illuminated CCD (Charge-Coupled Device) camera con-
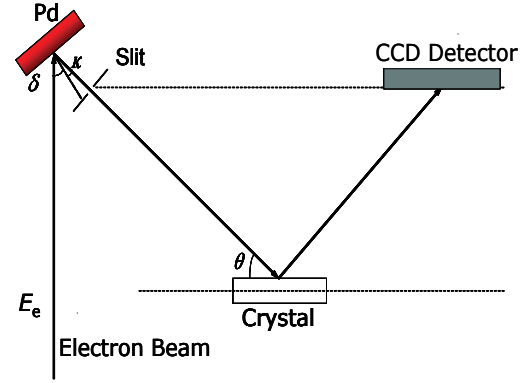

FIG. 1: (Color online) Top view of the experimental setup. The dotted lines represent the translation axes along which the crystal and CCD detector can be moved to change the central Bragg angle (for further details see [17]).

sisting of 1340×400 pixels with pixel sizes of 20×20 μm^2.

The $L\alpha$ x-ray emission spectrum of Pd was recorded for 15 different electron beam energies ranging from 4 keV to 18 keV (nominal energies). Depending on the incident electron energy and beam current, the collecting times varied between 1 and 5 hours. To probe the effect of L_3M vacancy states with more than one hole in the M-shell (see Appendix), measurements of the $L\beta_1$ (L_2-M_4 transition) and $L\beta_{3,4}$ ($L_1-M_{3,2}$ transitions) x-ray lines were also performed. The $L\beta_1$ line was measured at two electron beam energies ($E_e = 10$ keV and 15 keV), while the $L\beta_{3,4}$ lines were measured at a single beam energy ($E_e = 16$ keV). For the energy calibration of the $L\alpha_{1,2}$ x-ray spectra, the $K\alpha_1$ lines of Cr and Mn were

measured with the same crystal but in second order of diffraction, using the reference energies of 5414.805(7) eV and 5898.801(8) eV reported in [18]. The same method was employed to calibrate in energy the $L\beta_1$ and $L\beta_{3,4}$ spectra, but in this case, the $K\alpha_1$ x-ray lines of Mn and Fe ($E = 6404.006(10)$ eV [18]) were used as reference energies.
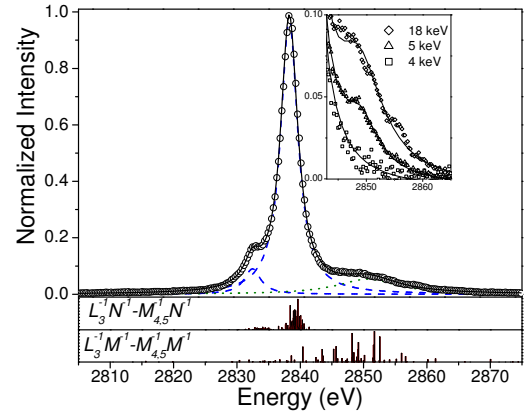

FIG. 2: (Color online) Fitted high-resolution $L\alpha$ x-ray spectrum of Pd at the incident electron beam energy of 8 keV. The solid thick line stands for the total fit to the experimental data (open circles), while the dashed lines and the dotted line represent the $L\alpha_{1,2}$ diagram and $L\alpha M$ satellite lines, respectively. The stick spectra in the lower panels correspond to the results of the MCDF calculations for the $L\alpha N$ and $L\alpha M$ satellite transitions. In the inset, the evolution of the M-satellites as a function of the beam energy is shown.

III.   DATA ANALYSIS AND METHODOLOGY

A.   Spectra fitting

For the Bragg angle region corresponding to the $L\alpha$ x-ray spectrum, the energy resolution of the von Hamos spectrometer was about 1.1 eV. This resolving power of $\sim 4 \times 10^{-4}$ allowed us to resolve the $L\alpha_{1,2}$ doublet and to separate the latter from its $M-$shell satellite structure. On the contrary, the $N-$shell satellites could not be resolved because, as shown by MCDF calculations [19], they are fully overlapping with the $L\alpha_{1,2}$ diagram lines, which leads to a non-lifetime broadening of the latter. The $L\alpha_{1,2}$ diagram lines and the unresolved $L\alpha N$ satellite lines were fitted with two Lorentzians, while a single Lorentzian was employed to fit the bump corresponding to the M-satellite structure. For illustration, the fitted $L\alpha_{1,2}$ spectrum measured at an incident electron

beam energy of 8 keV is depicted in Fig. 2. The M-satellite region is shown enlarged in the inset for three other beam energies (4 keV, 5 keV and 18 keV). The energies and relative intensities of the individual MCDF multiplet components corresponding to the $L\alpha N$ and $L\alpha M$ satellite transitions are also shown in the bottom panels.

For the spectra induced by the lower energy electrons, the $L\alpha M$ satellites are weak and the fluctuations of the experimental points rather large so that the fit of the satellite structure with a single Lorentzian looks
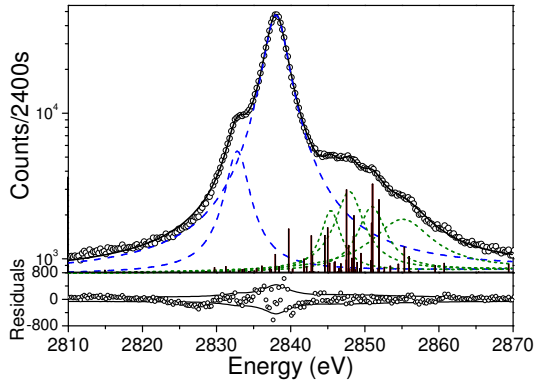
FIG. 3: (Color online) Pd high-resolution $L\alpha$ x-ray spectrum induced by the 12 keV electron beam and fitted with 6 Lorentz functions. The solid thick line represents the total fit to the experimental data (open circles), the dashed lines the fitted $L\alpha_{1,2}$ diagram transitions, the dot lines the fitted $L\alpha M$ satellites and the stick spectrum the results of the MCDF calculations for the $L\alpha M$ satellites. Fit residuals are shown in the lower panel where they are compared with the statistical errors ($\pm 2\sigma$) of the data points (thin lines).

quite reasonable. At higher electron energies, however, the intensity of the $M-$shell satellites increases and some fine structures can be oberved (see inset of Fig. 2). In this case the shape of the $M-$satellite region is more difficult to reproduce with a single Lorentzian. To probe the goodness of the satellite intensities returned by the single Lorentzian fits, the $L\alpha$ spectrum measured at 12 keV was refitted, using two Lorentzians for the diagram lines as before but four Lorentzians for the $M-$satellites. All parameters were let free in the fit. The spectrum measured at 12 keV

was chosen as probe-spectrum because at this energy the $L\alpha M$ to $L\alpha$ intensity ratio was found to be the biggest. The result of the new analysis is presented in Fig. 3. As shown, the fit is of good quality. In particular, the shape of the $L\alpha M$ satellite region is well reproduced by the four Lorentzians. However, it can be noted that some components on the left side of the MCDF stick spectrum coincide in position with the $L\alpha_1$ Lorentzian and, to a smaller extent, with the $L\alpha_2$ one, but clearly not with the four Lorentzians used to fit the satellite region. The fitted intensity of the diagram lines is therefore too big and the one of the satellites too small. To account for this impreciseness of the analysis, the satellite-to-diagram intensity ratio was corrected as follows:

$$i_{cor} = i_{fit} \frac{1 + \frac{\sum I_{MCDF}^{out}}{\sum I_{MCDF}^{in}}}{1 - i_{fit} \frac{\sum I_{MCDF}^{out}}{\sum I_{MCDF}^{in}}}, \qquad (1)$$

where $\sum I_{MCDF}^{in}$ represents the sum of the relative intensities of the MCDF components covered by the profile corresponding to the sum of the four satellite Lorentzians and $\sum I_{MCDF}^{out}$ the sum of the relative intensities of the MCDF components lying outside this profile. Using the above formula, a value $i_{cor} = 0.204(15)$ was found for the corrected $L\alpha M$ to $L\alpha$ intensity ratio, whereas the uncorrected ratio provided by the new fit was $i_{fit} = 0.156(12)$. It is somewhat surprising to note that the corrected ratio is in very good

agreement with the ratio of 0.201(8) obtained with the single Lorentzian fit. This is probably due to the fact that the low-energy tail of the broad single Lorentzian is partly overlapping with the diagram lines and covers thus the MCDF components that are lying outside the sum profile in the four-Lorentzians fit. Finally, as the ratios obtained by the two methods were consistent, we decided to use

the simplest method, i.e., to fit the satellite region of the 15 measured spectra with a single Lorentzian.

B. Parametrizations

For the beam energy E_e the corrected experimental intensity ratio $I_{L\alpha M}$ to $I_{L\alpha_{1,2}}$ can be written as:

$$i_{cor}(E_e) = \frac{\omega_{L\alpha M}}{\omega_{L\alpha}} \frac{\Omega^* c^* \left[N_{shake}(E_e) + f_{13}^{LLM} N_{L_1}(E_e) + N_{TS}(E_e) \right]}{\Omega c \left[N_{L_3}(E_e) - N_{shake}(E_e) + (f_{13}^{LLN} + f_{12}f_{23} + f_{13}')N_{L_1}(E_e) + f_{23}N_{L_2}(E_e) \right]},$$

$$(2)$$

where $\omega_{L\alpha}$ and $\omega_{L\alpha M}$ denote the $L\alpha_{1,2}$ and $L\alpha M$ partial x-ray fluorescence yields. The $\omega_{L\alpha M}$ to $\omega_{L\alpha}$ ratio can be deduced from a statistical scaling procedure [16, 20]. The instrumental efficiency is given by the term Ωc for the diagram lines and $\Omega^* c^*$ for the $M-$satellites, where Ω, respectively Ω^*, is the solid angle of the spectrometer and c, respectively c^*, an instrumental constant which takes into consideration the crystal reflectivity and CCD detector efficiency. As the energy difference between the diagram and satellite lines is only about 10 eV, the ratio $\frac{\Omega^* c^*}{\Omega c}$ is nearly equal to one. The coefficients

f_{ij} $(1 \leq i < j \leq 3)$ represent the $L_i - L_j$ subshell CK yields, f_{13}^{LLM} and f_{13}^{LLN} the partial CK yields of the $L_1 - L_3 M_{4,5}$ and $L_1 - L_3 N$ transitions, respectively, and f_{13}' the L_1 to L_3 hole-transfer rate resulting from the $L_1 - L_3$ radiative transition. However, the value of f_{13}' is very small as compared to the CK yields [21] and can thus be neglected.

The symbols N_s represent the number of atoms that undergo per second a given process s. Taking the target self-absorption into consideration, $N_s(E_e)$ can be written as:

$$N_{L_i,shake,TS}(E_e) = \frac{N_A N_e \rho}{A} \times \int_0^{h_{L_i,shake,TS}} \sigma_{L_i,shake,TS}(E(x)) \exp[-\mu \frac{x}{\cos(\kappa)}] dx. \qquad (3)$$

Here N_A is the Avogadro constant, N_e the number of electrons impinging per second on the target, ρ the density of the sample and A its atomic mass number. In the integral $\sigma_{L_i,shake,TS}(E)$ stands for the single ionization cross section of the L_i subshell, the shakeoff cross section or the cross section of the TS process, μ is the total absorption coefficient at the energy of the emitted $L\alpha$ or $L\alpha M$ x-ray and κ is the above mentioned x-ray exit angle.

Due to the lack of experimental EIICSs for the Pd $L-$subshells, the formula proposed by Campos et al. in [14] was used:

$$\sigma_{L_i}(U) = \frac{A_{L_i}}{B_{L_i} + U} \ln(U), \qquad (4)$$

where the dimensionless parameter $U = E/E_{L_i}^{thr}$ denotes the overvoltage of the incoming electron, E is the electron energy and $E_{L_i}^{thr}$ the ionization threshold energy for the L_i subshell. The parameters A_{L_i} and B_{L_i} depend on the atomic number Z of the target. They can be derived from the equations given in [14].

The shakeoff cross section σ_{shake} was obtained by multiplying the single ionization cross section σ_{L_3} by the shake probability given by the Thomas model [22]:

$$P_{Thomas}(E) = P_\infty \exp\left(-\frac{r^2 E_s^2}{15.32(E - E_{shake}^{thr})}\right). \qquad (5)$$

In the above equation, E_s is the shake energy, r the distance covered by the ionized electron during the time the atomic potential changes and P_∞ the shake probability at the saturation. The energies E, E_s and E_{shake}^{thr} are in eV and the radius r in Å. For E_s, the average binding energy of the M-shell electrons in Ag ($Z=47$) was employed [$(Z+1)-$potential approximation]. The theoretical $L_3 M$ shakeoff threshold was assumed to be the same as the one of the $L_3 M$ TS threshold:

$$E_{shake}^{thr} = E_{TS}^{thr} = E_{L_3}^{thr} + E_s. \qquad (6)$$

As suggested in [23], the distance r was approximated to the average value of the radii for which the squared $3d$ wave functions peak in ionic Pd$^+$. $3d$ orbitals were chosen because of their bigger shake probability and larger electron population as compared to $3s$ and $3p$ orbitals. The value of P_∞ was calculated in the framework of the sudden approximation

model [24], using self-consistent Dirac-Fock wavefunctions from the code of [25]. It should be mentioned here that the Thomas model was originally developed for shake processes following photoionization. We have thus implicitly assumed that the shake probability is independent from the first ionization mechanism. This assumption is, however, not critical because the shake contribution to the total L_3M DI was found to be small with respect to other processes (see Fig. 5).

The upper integration limits $h_{L_i,shake,TS}$ in Eq. (3) correspond to the depths in the sample at which the electron energy $E(x) = E^{thr}_{L_i,shake,TS}$, where $E^{thr}_{L_i,shake,TS}$ is the threshold energy of the single L_i subshell ionization, shake or TS process. Providing that the multiple scattering of the incoming electrons can be neglected, these depths can be derived from the stopping power $s(E)$:

$$s(E) = -\frac{dE}{dx/\cos\delta} \rightarrow h_{L_i,shake,TS} = x|_0^{h_{L_i,shake,TS}} = -\int_{E_e}^{E^{thr}_{L_i,shake,TS}} \frac{\cos\delta}{s(E)} dE, \qquad (7)$$

where δ is the angle between the incoming electron beam and the normal to the sample surface. As the coordinate x is equal to zero at the front surface of the sample, the above depths can be interpreted as effective sample thicknesses for the three processes. The values of $s(E)$ were determined by interpolating the data quoted in the NIST tables [26] with the program ESTAR [27], using a grid of 10 eV steps. A trapezoidal integration algorithm was then employed to calculate numerically the effective sample thicknesses for the different beam energies.

As the constant $C = \frac{N_A N_e \rho}{A}$ in Eq. (3) can be set as a common factor in both the numerator and denominator of Eq. (2) and thus cancels out, the following new parameters will be used in further discussions:

$$\Pi_{L_i,shake,TS}(E_e) = N_{L_i,shake,TS}(E_e)/C. \quad (8)$$

The quantities $\Pi_{L_i,shake,TS}(E_e)$, named hereafter *cross-section-integrals*, have the dimension of a cross section multiplied by a length. Replacing $N_{L_i,shake,TS}(E_e)$ by the corresponding cross-section-integrals, one can write Eq. (2) in the following form:

$$i_{cor}(E_e) = i_{shake}(E_e) + i_{CK}(E_e) + i_{TS}(E_e), \qquad (9)$$

where the partial ratios corresponding to the shake, Coster-Kronig and two-step processes

are given by:

$$i_{TS}(E_e) = \frac{\omega_{L\alpha M}}{\omega_{L\alpha}} \frac{\Pi_{TS}(E_e)}{D(E_e)}. \qquad (12)$$

$$i_{shake}(E_e) = \frac{\omega_{L\alpha M}}{\omega_{L\alpha}} \frac{\Pi_{shake}(E_e)}{D(E_e)}, \qquad (10)$$

In the three above equations, the function $D(E_e)$ is defined by:

$$i_{CK}(E_e) = \frac{\omega_{L\alpha M}}{\omega_{L\alpha}} \frac{f_{13}^{LLM} \Pi_{L_1}(E_e)}{D(E_e)}, \qquad (11)$$

$$D(E_e) = \Pi_{L3}(E_e) - \Pi_{shake}(E_e) + (f_{13}^{LLN} + f_{12}f_{23})\Pi_{L_1}(E_e) + f_{23}\Pi_{L_2}(E_e). \qquad (13)$$

The experimental TS cross-section-integrals can then be deduced from Eqs. (12) and (9):

$$\Pi_{TS}^{exp}(E_e) = \frac{\omega_{L\alpha}}{\omega_{L\alpha M}} D(E_e) \times \left(i_{cor}(E_e) - i_{shake}(E_e) - i_{CK}(E_e) \right). \qquad (14)$$

To determine the TS cross section or TS cross-section-integral at any electron energy E, an analytical expression is, however, needed. Two different approaches were employed. In the first one, an energy dependence similar to the one proposed by Campos [14] was used:

$$\sigma_{TS}(U') = \frac{A_{TS}}{B_{TS} + U'} \ln(U'). \qquad (15)$$

In the above equation the unknown parameters are A_{TS} and B_{TS}, the threshold energy

being given by Eq. (6). The notation U' is employed to distinguish the TS overvoltage from the single ionization overvoltage U occuring in Eq. (4).

As the Campos model is usually employed for the determination of single ionization cross sections, an alternative approach based on the model of Pattard and Rost [28–30] was also probed. In this model the electron-induced multi-ionization cross section has the following form:

$$\sigma(E) = \sigma_M \left[\frac{E - E_{thr}}{E_M - E_{thr}} \right]^{\alpha} \left[\frac{\alpha + 1}{\alpha \left(\frac{E - E_{thr}}{E_M - E_{thr}} \right) + 1} \right]^{(\alpha+1)}, \qquad (16)$$

where E_M and σ_M are the energy and amplitude of the maximum cross section. For the threshold exponent α, a value of 2.2704 was adopted as suggested in [29] for mid-heavy and heavy elements.

To determine the values of the parameters A_{TS} and B_{TS} of Eq. (15) and σ_M and E_M of Eq. (16) that reproduce at best the experimental data, the least-squares fit from the Matlab$^{\text{TM}}$ optimization package was employed. The algorithm is based on the trust-region reflective Newton method [31]. Briefly speaking, the program minimizes the quantity χ^2 defined by:

$$\chi^2 = \sum [\Pi_{TS}^{fit}(E_e) - \Pi_{TS}^{exp}(E_e)]^2, \qquad (17)$$

where $\Pi_{TS}^{fit}(E_e)$ and $\Pi_{TS}^{exp}(E_e)$ stand for the fitted and experimental values of the two-step cross-section-integrals. The fitting error for the parameter p_i is then given by:

$$\Delta(p_i) = \sqrt{\chi^2 \mathcal{C}_{ii}}, \qquad (18)$$

where $\mathcal{C}_{ii}$ is the i-th diagonal element of the associated error matrix. The parameter χ^2 was preferred to the reduced $\tilde{\chi}^2$ to evaluate the goodness of the numerical optimization

precisely because it can be also used to calculate the errors of the fitted parameters.

C. Experimental determination of the TS cross sections as a function of the electron energy

As shown by Eq. (3) the calculation of the cross sections $\sigma_{TS}(E)$ requires the knowledge of the function $E(x)$. In principle, the variation $E(x)$ of the electron energy as a function of the penetration depth could be parametrized using a power law for the energy dependence and determining the constants entering the power law equation with the known stopping powers $s(E)$. In this work, another approach was employed. First, the different beam energies were numbered from 2 for the lowest beam energy to 16 for the highest one, the number 1 being assigned to the threshold energy of the TS process (i.e., $E_e^{(1)} = E_{TS}^{thr}$, $E_e^{(2)} = 4$ keV, ..., $E_e^{(16)} = 18$ keV). The thick target was then divided in several slices of variable thicknesses, the thickness of the slice number i ($i = 1, 2, ..., 15$) being given by $h_{TS}^{(i+1)} - h_{TS}^{(i)}$, where $h_{TS}^{(i)}$ represents the effective thickness of the target for the i-th beam energy. For
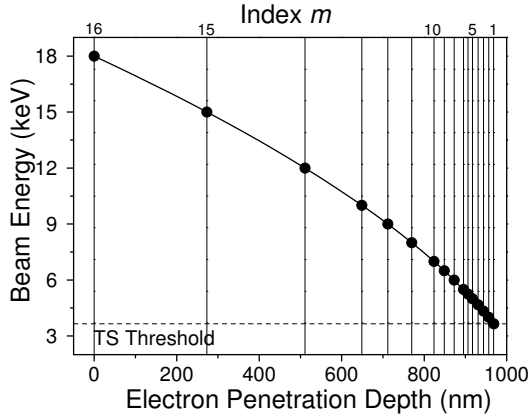
FIG. 4: Target slices and effective TS target thicknesses for the employed electron beam energies. The highest beam energy (18 keV) corresponds to the index m=16, the lowest one (4 keV) to the index m=2, whereas the index m=1 is assigned to the threshold energy for the TS process. The effective thickness corresponding to a particular beam energy $E_e^{(m)}$ is given by the difference between the x-coordinates of the vertical lines labeled 1 and m. Similarly, the thickness of the m-th slice is given by the difference between the x-coordinates of the vertical lines labeled m and $m+1$.

$i > 1$, the effective thicknesses were calculated with Eq. (7), whereas $h_{TS}^{(1)} = 0$ per definition.

The decomposition of the thick target into slices is depicted in Fig. 4. The y-coordinates of the black points correspond to the nominal beam energies. As shown, the curve passing through these points has a negative curvature, which indicates that the specific energy losses of the electrons grow with decreasing energies. The slice number is given by the index m associated to the right boundary of the slice. The virtual front surface for electron beam impact with a nominal energy of $E_e^{(m)}$ is defined by the left boundary of the $(m-1)$-th slice. The thickest slice is the 15th one which is related to the beam energy $E_e^{(16)}$ = 18 keV. Its thickness which corresponds to an energy loss of 3 keV is 273 nm. For this beam energy, the effective target thickness is 969 nm. For comparison, for the next lower energy beams $E_e^{(15)}$=15 keV, $E_e^{(14)}$=12 keV and $E_e^{(13)}$=10 keV, the effective thicknesses are 696, 458 and 320 nm, respectively.

According to Eq. (3) and Eq. (8), the experimental cross-section-integrals $\Pi_{TS}(E_e^{(m)})$ can then be expressed as:

$$\Pi_{TS}^{exp}(E_e^{(m)}) = \sum_{i=2}^{m} \int_{h_{TS}^{(i-1)}}^{h_{TS}^{(i)}} \sigma_{TS}(E(x)) \exp\left[-\mu\frac{x}{\cos(\kappa)}\right] \mathrm{d}x. \tag{19}$$

Using a trapezoidal algorithm to evaluate the integrals in Eq.(19), the cross-section-integrals can be written as follows:

$$\Pi_{TS}^{exp}(E_e^m) \approx$$

$$\sum_{i=2}^{m}(h_{TS}^{(i)} - h_{TS}^{(i-1)})\frac{\sigma_{TS}(E_e^{(i)})+\sigma_{TS}(E_e^{(i-1)})}{2} \exp\left[-\mu\frac{h_{TS}^{(m)}-h_{TS}^{(i)}}{\cos(\kappa)}\right] \exp\left[-\mu\frac{h_{TS}^{(i)}-h_{TS}^{(i-1)}}{2\cos(\kappa)}\right]. \quad (20)$$

The terms $\exp\left[-\mu\frac{h_{TS}^{(i)}-h_{TS}^{(i-1)}}{2\cos(\kappa)}\right]$ and $\exp\left[-\mu\frac{h_{TS}^{(m)}-h_{TS}^{(i)}}{\cos(\kappa)}\right]$ in Eq. (20) account for the absorption of the emitted x-rays in the target layer extending from the middle

of the $(i-1)$-th slice to the virtual front surface. From Eq. (20) the following recurrence relation between the cross-section-integrals $\Pi_{TS}^{exp}(E_e^{(m)})$ and $\Pi_{TS}^{exp}(E_e^{(m-1)})$ can be derived:

$$\Pi_{TS}^{exp}(E_e^{(m)}) = \Pi_{TS}^{exp}(E_e^{(m-1)}) \exp\left[-\mu\frac{h_{TS}^{(m)}-h_{TS}^{(m-1)}}{\cos(\kappa)}\right]$$

$$+ \frac{\sigma_{TS}(E_e^{(m)})+\sigma_{TS}(E_e^{(m-1)})}{2}(h_{TS}^{(m)}-h_{TS}^{(m-1)}) \exp\left[-\mu\frac{h_{TS}^{(m)}-h_{TS}^{(m-1)}}{2\cos(\kappa)}\right]. \quad (21)$$

Finally, using the approximation

$$\frac{\sigma_{TS}(E_e^{(m)})+\sigma_{TS}(E_e^{(m-1)})}{2} = \sigma_{TS}(E_{av}),$$

$$(22)$$

where $E_{av} = \frac{E_e^{(m)}+E_e^{(m-1)}}{2}$, the TS cross section $\sigma_{TS}(E_{av})$ is given by:

$$\sigma_{TS}(E_{av}) \approx \frac{\Pi_{TS}^{exp}(E_e^{(m)}) - \Pi_{TS}^{exp}(E_e^{(m-1)}) \exp\left[-\mu\frac{h_{TS}^{(m)}-h_{TS}^{(m-1)}}{\cos(\kappa)}\right]}{(h_{TS}^{(m)}-h_{TS}^{(m-1)}) \exp\left[-\mu\frac{h_{TS}^{(m)}-h_{TS}^{(m-1)}}{2\cos(\kappa)}\right]}. \quad (23)$$

It should be noted at this point that E_{av} represents the "average" energy of the $E_e^{(m)}$ electron beam in the $(m-1)$-th slice and not the average energy with respect to the whole pen-

etration depth.

IV.   RESULTS AND DISCUSSION

As shown in the preceding section, a precise determination of the TS process contribution to the observed $L\alpha M$ to $L\alpha$ intensity ratios requires a reliable knowledge of the electron-induced single ionization cross sections σ_{L_i}. Therefore, the DWBA-based predictions from Eq. (4) were carefully probed by comparing them to experimental L x-ray production cross sections measured for neighbouring elements [32]. The coefficients A_{L_i} and B_{L_i} of Eq. (4) were computed using the Z-dependence formula given in Ref. [14], whereas for the calculation of the overvoltages U, the experimental L_i-subshell ionization thresholds reported in Ref. [16] were used. The latter and the employed A_{L_i} and B_{L_i} values are listed in Table I. From the comparison it was found that the theoretical values from Eq. (4) are reliable over a wide range of incident electron energies. It should be mentioned, however, that the goodness of the theoretical predictions was more difficult to probe for impact energies just above the ionization thresholds because experimental data are scarce in these energy regions and affected by larger uncertainties due to the tiny values of the x-ray production cross sections, particularly those corresponding to

the L_1-subshell. Nevertheless, the relative uncertainties of 4% quoted in Ref. [14] were adopted for the present cross sections σ_{L_i}. The bremsstrahlung and scattering cross sections of medium energy electrons are small as compared to the L_i EIICSs [10, 33] so that they were neglected. The influence of the multiple M-shell ionization was also probed by performing complementary meaurements of the $L\beta_1$ and $L\beta_{3,4}$ x-ray emission lines. As shown in the Appendix, the effect of this multiple ionization is also negligibly small and was thus neither considered. The shakeoff cross sections were determined according to the method presented in Sect. III B and the CK rates f_{ij} were taken from Ref. [16] (see Table I). Note that for Pd $f_{23} = f_{23}^{LLN}$ because $L_2 - L_3 M$ CK transitions are energetically forbidden. The experimental $L\alpha M$ to $L\alpha$ intensity ratios obtained in the present work are shown in Fig. 5 as a function of the nominal electron beam energy. The Coster-Kronig (CK), shakeoff (SO) and two-step (TS) contributions to the intensity ratios are also depicted. They were computed using the method and the equations presented in Sect. III B. For the TS ratios, negative values were found for the lowest beam energies. This is probably due to the fact that the L_1 EIICSs calculated with Eq. (4) are somewhat overestimated in the energy region close to the L_1 ionization threshold. On the other
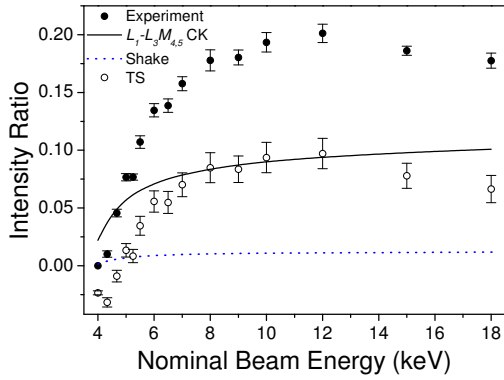
FIG. 5: Experimental $L\alpha M$ to $L\alpha_{1,2}$ intensity ratios (full circles) as a function of the nominal electron beam energy. The partial ratios corresponding to the $L_1 - L_3 M_{4,5}$ Coster-Kronig (solid line), shakeoff (dashed line) and two-step (open circles) processes are also shown.

hand, as shown in Fig. 5, for all beam energies the SO ratios were found to be small as compared to the ones of the two other processes. This is, however, not surprising since it is well known that the probability to observe a shakeoff process in the M-shell as a result of a primary L-shell ionization is very small.

The experimental cross-section-integrals Π_{TS}^{exp} determined from Eq. (14) are listed in the 3rd column of Table II and also presented in Fig. 6 as a function of the nominal beam energies. For the determination of the experimental threshold energy of the TS process, a method similar to the one used in Ref. [34] to deduce the Cu double K-shell ionization threshold was employed. The threshold energy was indeed determined by cal-

culating the x-coordinate of the intersection point of the linear regression lines defined by the data points corresponding to the three lowest beam energies, respectively the five data points lying in the region of fast-increase (see Fig. 6b). A value of 4.89 ± 0.85 keV was found. The rather large uncertainty obtained for E_{TS}^{thr} is due to the statistical errors affecting the low energy data and to the propagation of the errors related to the subtraction of the cross sections corresponding to the other processes. Note that a more precise determination of E_{TS}^{thr} would represent a challenging task because for electron energies close to the threshold the $L\alpha M$ satellite lines due to the TS process are characterized by very low count rates, which leads to high statistical errors. In addition, available experimental CK yields [16, 35, 36] suffer all from rather large uncertainties. On the other hand, the obtained threshold energy is bigger than the value of 3.65 keV provided by the $(Z+1)$ potential approximation (Eq. (6)). This trend, however, is consistent with former observations, e.g., the one concerning the threshold energy of the electron-induced double K-shell ionization of Al [37].

The parameters of the Campos (Eq. (15)) and Pattard-Rost (Eq. (16)) models were numerically optimized in a least-squares fit of the experimental cross-section-integrals $\Pi_{TS}^{exp}(E_e^{(m)})$ with Eq. (19). For the Campos

TABLE I: Coster-Kronig yields f_{ij}, ionization threshold energies $E_{L_i}^{thr}$ and electron impact ionization cross section parameters A_{L_i} and B_{L_i} for the palladium L_i ($i = 1, 2, 3$) subshells. The E_{L_i}'s are expressed in keV, the A_{L_i}'s in kbarn, whereas the B_{L_i}'s are dimensionless parameters.

i	f_{i2}	f_{i3}^{LLM}	f_{i3}^{LLN}	E_{Li}^{thr}	A_{L_i}	B_{L_i}
1	0.047(1)	0.406(23)	0.324(32)	3.61	7.047	0.27426
2	-	-	0.164(33)	3.32	10.305	0.08182
3	-	-	-	3.17	23.614	0.06025

TABLE II: Nominal electron beam energies E_e in keV, experimental $L\alpha M$ to $L\alpha$ intensity ratios, cross-section-integrals $\Pi_{TS}^{exp}(E_e)$ in kbarn·nm, average beam energies E_{av} in keV and cross sections $\sigma_{TS}(E_{av})$ in kbarn. E_{av} represents the average beam energy in the first slice crossed by the incoming electrons.

| E_e	$I_{L\alpha M}/I_{L\alpha}$	$\Pi_{TS}^{exp}(E_e)$	E_{av}	$\sigma_{TS}(E_{av})$
4.00	0	-1.6 (0.1)	-	-
4.33	0.010(3)	-4.2 (0.5)	-	-
4.67	0.046(3)	-1.9 (1.1)	-	-
5.00	0.077(3)	4.1 (1.8)	-	-
5.25	0.077(3)	3.2 (2.2)	5.13	-0.08(27)
5.50	0.107(5)	16.1 (3.8)	5.38	1.19(41)
6.00	0.135(6)	36.0 (5.9)	5.75	0.89(31)
6.50	0.139(6)	46.4 (8.0)	6.25	0.46(42)
7.00	0.156(6)	74.3 (10.7)	6.75	1.15(53)
8.00	0.178(9)	128.7(19.4)	7.50	1.09(42)
9.00	0.180(6)	166.9(22.4)	8.50	0.77(51)
10.0	0.193(8)	233.7(32.0)	9.50	1.22(63)
12.0	0.201(8)	339.1(44.7)	11.0	0.98(41)
15.0	0.186(4)	380.4(51.7)	13.5	0.44(29)
18.0	0.178(6)	402.9(70.9)	16.5	0.38(33)
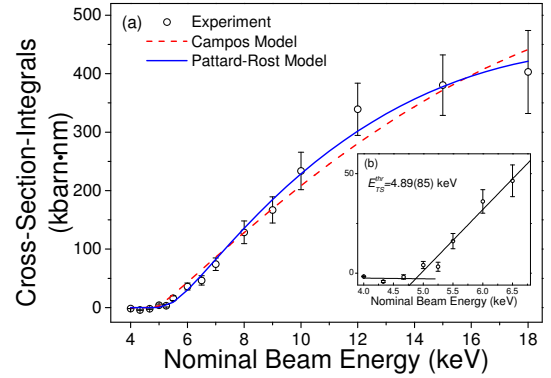
FIG. 6: (Color online) Two-step cross-section-integrals vs nominal electron beam energies. (a) Present experimental values (open circles) and results of the least-squares fits to the experimental data with Eq. (19) using the Pattard-Rost [28–30] (solid line) and Campos [14] (dashed line) models for the energy dependence of the cross sections. (b) Enlarged view of the low energy and fast increase regions showing the data points and regression lines employed to determine the threshold energy of the TS process.

model, only A_{TS} and B_{TS} could be used as free fitting parameters, whereas the threshold energy had to be kept fixed at the value obtained with the above described method (see Fig. 6b). This is due to the fact that some experimental Π_{TS}^{exp} close to the threshold are negative so that the fit may converge for negative values of $\ln(U')$. If one uses in the fit the constraint that the experimental Π_{TS}^{exp} should be zero below the threshold, the fit simply pushes up the fitted value of the threshold. The Campos parameters A_{TS} and B_{TS} obtained from the fit are presented in the 2nd row of Table III. For the Pattard-

Rost model, all parameters could be fitted, the threshold energy included. Results are presented in the 5th row of Table III. A fit with the Pattard-Rost model was also performed with a fixed threshold energy. The σ_M and E_M values obtained from this second fit (see 4th row of Table III) were found, however, to be consistent within the fitting errors with the results obtained from the three parameters fit. For the three fits, the summed squared residuals are quoted in the 5th column of the table. The curves corresponding to the cross-section-integrals fitted with the Campos and Pattard-Rost (threshold energy free) models are depicted in Fig. 6 where they are compared to the experimental values.

From Fig. 6 and Table III, it is obvious that the Pattard-Rost model fits better the experimental cross-section-integrals than the Campos model. A rapid inspection of the table shows in particular that the χ^2 corresponding to the two Pattard-Rost fits are about three times smaller than the one of the fit performed with the Campos model. This is, however, not really surprising because the Campos model was developed for the calculation of single ionization cross sections. It can be also noted that the threshold energy obtained from the three parameters Pattard-Rost fit is in good agreement with the value obtained from the intersection of the regression lines corresponding to the experimental
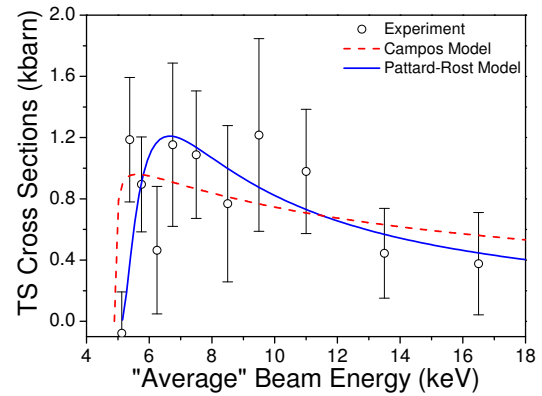

FIG. 7: (Color online) Electron-induced two-step double L_3M ionization cross sections σ_{TS} vs the average value of the beam energy E_{av} in the first crossed target slice. The open circles represent the experimental values obtained with the slice division method described in the text, whereas the solid and dashed lines correspond to the theoretical two-step cross sections calculated using the Pattard-Rost [28–30] and Campos [14] models, respectively.

data points located in, respectively below, the fast increase region.

The experimental cross sections $\sigma_{TS}(E_{av})$ determined from Eq. (23) and the associated "average" energies E_{av} are presented in Table II. They are compared to the values derived from the Campos and Pattard-Rost models in Fig. 7. As shown, the experimental results are affected by rather large uncertainties. The latter are mainly due to the fact that the TS cross sections were determined from the differences of two cross-sections-integrals whose uncertainties are almost as big as their differences. Nevertheless, the curves derived from the Pattard-

TABLE III: Fitted values of the Campos and Pattard-Rost parameters used for the determination of the TS double ionization cross sections. A_{TS} and σ_M are expressed in kbarn, E_{TS}^{thr} and E_M in keV, χ^2 in (kbarn·nm)^2 and B_{TS} is a dimensionless parameter.

Model	A_{TS}	B_{TS}	E_{TS}^{thr}	χ^2
Campos *	1.10(22)	-0.99(06)	4.89(85)	6239
	σ_M	E_M	E_{TS}^{thr}	χ^2
Pattard-Rost*	1.14(16	6.65(58)	4.89(85)	2394
Pattard-Rost†	1.21(38)	6.65(51)	5.11(94)	2280

*ionization threshold fixed in the fit
†ionization threshold free in the fit

Rost model and, to a smaller extent, from the Campos one, reproduce satisfactorily the experimental data. In particular, the maximum cross section σ_M obtained from the Pattard-Rost fit is close to the largest experimental values, whereas the experimental energies corresponding to the biggest cross sections seem to be somewhat underestimated by the theoretical value E_M. A simpler and more straightforward method to determine the dependence of the TS cross sections on the incoming electron energy would have consisted to use very thin targets, i.e., targets with thicknesses in the order of μg/cm^2. In this case, the average energy of the incoming electrons is indeed almost equal to the nominal electron beam energy. However, due to the thinness of the target and the tiny values of the TS cross sections, the partial intensities of the $L\alpha M$ satellites corresponding to the TS process are then so small that they can no more be resolved from the background when the measurements are performed by means of high-resolution x-ray spectroscopy. In addition, due to the electron bombardment large amounts of heat are produced in the target. Test measurements performed with a $\sim$1 μm thick Pd foil showed that the latter started to melt after a few minutes of bombardement. The novel target slice decomposition method employed in this work has thus permitted us to circumvent these intensity and heat load problems.

V.   SUMMARY AND CONCLUDING REMARKS

The palladium $L\alpha$ x-ray spectrum induced by impact with medium-energy electrons was measured by means of high-resolution x-ray spectroscopy using a Bragg-type von Hamos bent crystal spectrometer. The measurements were performed for 15 different electron beam energies ranging from 4 keV to 18 keV. From the observed intensity ratios of the resolved $L\alpha M$ satellites to the parent

$L\alpha_{1,2}$ diagram lines the partial ratios corresponding to the TS process were determined as a function of the nominal electron energy, the contributions to the double L_3M ionization of the $L_1 - L_3M_{4,5}$ CK transitions and shakeoff process having been subtracted beforehand. From the obtained partial intensity ratios the cross-section-integrals associated to the TS process could be determined. It was found that the variation of the TS cross-section-integrals as a function of the nominal electron energy can be well reproduced by using in their calculation the cross section energy dependencies proposed by Campos and Pattard-Rost for the parametrization of $(e, 3e)$ collisions in mid- and high-Z elements. The parameters related to the two models were then determined by fitting the Campos and Pattard-Rost functions to the experimental TS cross-section-integrals. By inserting the fitted parameters in the corresponding cross section formulas of Campos and Pattard Rost, we were able to compute the variation of the TS cross section as a function of the electron energy. On the other hand, the experimental TS cross sections could be also determined directly from the measured cross-section-integrals, using a novel model-independent method based on the decomposition of the thick target into slices. A very satisfactory agreement was observed between the model-dependent and pure experimental

TS cross sections. To our best knowledge, it is the first time that electron-induced two-step double ionization cross sections could be determined for mid-heavy elements. Furthermore, in our opinion, the novel slice decomposition technique used in the present work could be very helpful in many charged particle-induced x-ray fluorescence measurements for which the fluorescence signal has to be determined as a function of the energy of the incoming particles and the use of a thick target is simultaneously mandatory to get a strong enough signal.

APPENDIX A: CONTRIBUTION OF TRIPLY IONIZED STATES TO THE OBSERVED $L\alpha M$ SATELLITE YIELDS

According to MCDF calculations, some low energy components pertaining to the 2nd order $L\alpha M^{(2)}$ satellite (L_3M^{-2}-$M_{4,5}M^{-2}$ transition) are partly overlapping with the 1st order $L\alpha M$ satellite whose relative intensity was used to determine the two-step cross sections. The latter might be thus somewhat overestimated. $L_3^{-1}M^{-2}$ triple vacancy states may be created either directly via electron-induced L_3MM triple ionization or indirectly via electron-induced L_1M double ionization followed by $L_1-L_3M_{4,5}$ CK transitions. Note that the combination of L_2M double ionization followed by $L_2 - L_3M_{4,5}$ CK transi-

tions has not to be considered because for Pd $L_2 - L_3 M_{4,5}$ CK transitions are energetically forbidden. Furthermore, since in all measured $L\alpha$ spectra no structure could be observed in the energy region between 2862 eV and 2865 eV where, according to MCDF calculations, the most intense components of the second order $L\alpha M^{(2)}$ satellite are expected, the contribution of the radiative decay of the $L_3^{-1} M^{-2}$ triple vacancy states to the observed $L\alpha M$ satellite yields was estimated theoretically.

The direct $L_3 MM$ triple ionization was assumed to be decomposable into a $L_3 M$ TS double ionization followed by an additional single M-shell ionization. The number of triply ionized Pd atoms N_{tri} produced per second is thus given by the number of atoms doubly ionized as a result of a TS process multiplied by the probability P_M for a single M-shell ionization, i.e.,

$$N_{tri} \approx N_{TS} P_M = N_{TS} n h_{eff} \sigma_M, \quad \text{(A1)}$$

where n stands for the number of atoms per unit volume and h_{eff} the effective target thickness. Similarly, the TS process can be considered as a single L_3-subshell ionization followed by a single M-shell ionization so that

$$N_{TS} \approx N_{L_3} n h_{eff} \sigma_M, \quad \text{(A2)}$$

and the N_{tri} to N_{TS} ratio can be approximated to:

$$\frac{N_{tri}}{N_{TS}}(E_e) \approx \frac{N_{TS}}{N_{L_3}}(E_e). \quad \text{(A3)}$$

In the above relation the differences between the threshold energies corresponding to the single, double and triple ionization were neglected. The relative excess of intensity of the $L\alpha M$ satellite due to the direct $L_3 MM$ triple ionization is then given by the following relation:

$$i_{excess}^{L_3 MM}(E_e) \approx \frac{N_{tri}}{N_{TS}}(E_e) \times \frac{\sum I_{MCDF}^{overlap}}{\sum I_{MCDF}^{tot}} \times \frac{\omega_{L\alpha M^2}}{\omega_{L\alpha M}}, \quad \text{(A4)}$$

where $\sum I_{MCDF}^{tot}$ and $\sum I_{MCDF}^{overlap}$ represent the sum of the intensities of the MCDF components corresponding to the $L_3^{-1} M^{-2} \rightarrow L_3 M^{-3}$ transition, respectively the sum of the intensities of the latter components which are overlapping with the $L_3^{-1} M^{-1} \rightarrow L_3 M^{-2}$ transition and $\omega_{L\alpha M^1}$ and $\omega_{L\alpha M^2}$ stand for the partial fluorescence yields of the 1st and 2nd order M-satellite lines. The fluorescence yields were determined with a statistical scaling procedure. From Eq. (A4) a maximum value of 1.8(2)% (at E_e=12 keV) was found for the relative contribution of the direct triple ionization $L_3 MM$ to the TS DI cross sections listed in Table II.

As mentioned above, $L_3^{-1} M^{-2}$ triply ionized states may also be created indirectly via $L_1 M$ DI followed by $L_1 - L_3 M_{4,5}$ CK transi-
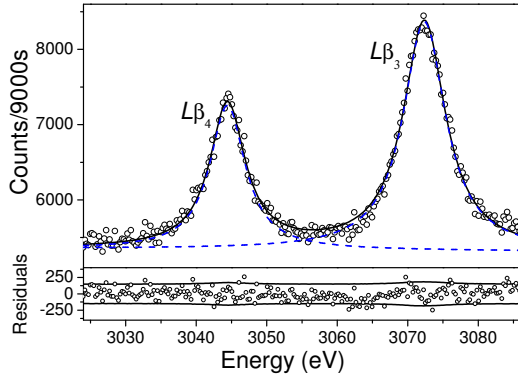
FIG. 8: (Color online) High-resolution $L\beta_{3,4}$ x-ray spectrum of Pd induced by impact with 16 keV electrons. The spectrum was fitted with two Lorentz functions. The thick solid line represents the total fit to the experimental data (open circles) and the dashed lines stand for the fitted $L\beta_4$ and $L\beta_3$ diagram lines. No satellite-induced asymmetry was observed in the high-energy tails of the diagram lines. Fit residuals are shown in the lower panel where they are compared with the statistical errors ($\pm 2\sigma$) of the data points (thin lines).
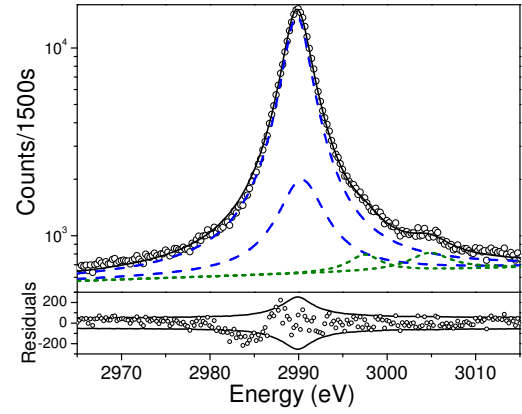
FIG. 9: (Color online) High-resolution $L\beta_1$ x-ray spectrum of Pd induced by impact with 15 keV electrons. The spectrum was fitted with four Lorentz functions. The thick solid line represents the total fit to the experimental data (open circles), the dashed lines the fitted $L\beta_1$ diagram line and $L\beta_1 N$ satellite and the dotted lines the $L\beta_1 M$ satellites. Fit residuals are shown in the lower panel where they are compared with the statistical errors ($\pm 2\sigma$) of the data points (thin lines).

tions. To probe the strength of the $L_1 M$ DI, the $L\beta_{3,4}$ x-ray lines ($L_1 - M_{3,2}$ transitions) were measured. The spectrum was recorded at a beam energy of 16 keV. As the weak $L\beta_6$ x-ray line ($L_3 - N_1$ transition) is lying on the high-energy tail of the $L\beta_3$ line [18] and because both lines are partly overlapping due to their large natural widths [38], only the $L\beta_4$ line was used to probe the $L_1 M$ DI. As shown in Fig. 8 no resolved line or asymmetry corresponding to the M satellite is visible on the high-energy side of the $L\beta_4$ line, proving thus that the $L_1 M$ DI process is negligibly small.

A further contribution to the observed $L\alpha M$ satellite intensities may arise from $L_2 M$ DI followed by $L_2 - L_3 N$ CK transitions. This sequence of processes leads indeed to $L_3^{-1} M^{-1} N^{-1}$ triple vacancy states whose radiative decay gives rise to x-ray transitions that are also overlapping with the $L\alpha M$ satellite. To probe the strength of the $L_2 M$ DI, the $L\beta_1$ x-ray line ($L_2 - M_4$ transition) was measured at two different beam energies (10 keV and 15 keV). The spectrum measured at 15 keV is depicted in Fig. 9. As shown, M- and N-shell satellites are observed. The M-satellites are mainly due to the electron-induced $L_2 M$ DI, whereas the

N-satellites arise from $L_1 - L_2N$ CK transitions. In the fit, the energy difference between the Lorentzians corresponding to the $L\beta_1N$ satellite structure and $L\beta_1$ diagram line was kept fixed at the value provided by the MCDF calculations [19], whereas the widths and intensities of the two lines were let free. The $L\beta_1M$ satellite structure was fitted with two Lorentzians, whose widths, intensities and centroid positions were used as free fitting parameters. From the fit a value of 2.8(7)% was found for the intensity ratio of the $L\beta_1M$ satellite to $L\beta_1$ diagram line. Similarly to Eq. (2), this ratio can be written:

$$i^*(E_e) = \frac{\omega_{L\beta_1M}}{\omega_{L\beta_1}} \times$$
$$\frac{N^*_{shake}(E_e)+N^*_{TS}(E_e)}{(1-f_{23})N_{L_2}(E_e)-N^*_{shake}(E_e)+f_{12}N_{L_1}(E_e)}, \quad (A5)$$

where $\omega_{L\beta_1M}$ and $\omega_{L\beta_1}$ are the partial fluorescence yields of the $L\beta_1M$ and $L\beta_1$ transitions, respectively. The quantities N^*_s have the same meaning as in Eq. (2), the upper star indicating, however, that the shake and TS processes concern now the L_2- instead of L_3-subshell. Using similar calculations as those presented in Sec. III B, the two-step cross-section-integrals $\Pi^*_{TS}(E_e)$ could be then derived. From the latter, the contribution

Π^{add}_{TS} of the L_2M DI followed by L_2-L_3N CK transitions to the experimental cross-section-integrals Π^{exp}_{TS} defined in Eq. (9) was determined, using the f_{23} CK rate quoted in [16]:

$$\Pi^{add}_{TS}(E_e) \approx f_{23}\Pi^*_{TS}(E_e) \qquad (A6)$$

Finally, Π^{add}_{TS}:Π^{exp}_{TS} ratios of 1.3(7)% at $E_e = 15$ keV and 0.6(6)% at $E_e = 10$ keV were obtained.

In conclusion, the total contribution to the TS double ionization cross sections from processes leading to a triple ionization of the Pd atoms is 3.1(7)% for the highest beam energies (15 keV and 18 keV) and significantly smaller for energies below 10 keV. As the contribution varies with the beam energy, a systematic correction of the TS cross sections listed in Table II would have required to measure the $L\beta_{3,4}$ and $L\beta_1$ spectra at the 15 beam energies employed for the measurements of the $L\alpha$ spectra. However, since the corrections are rather small, we have renounced to perform these additional measurements and the systematic errors originating from the triple ionization were taken into consideration in the cross section uncertainties quoted in Table II.

---

[1] T. Åberg, Phys. Rev. **156**, 35 (1967).

[2] T. A. Carlson and M. O. Krause, Phys. Rev.

140, 1057 (1965).

[3] Y. V. Popov, C. Dal Cappello, B. Joulakian,

and N. M. Kurmina, J. Phys. B **27**, 1599 (1994).

[4] B. E. Marji, C. Schröter, A. Duguet, A. Lahmam-Bennani, M. Lecas, and L. Spielberger, J. Phys. B **30**, 3677 (1997).

[5] J. Berakdar, A. Lahmam-Bennani, and C. Dal Cappello, Phys. Rep. **374**, 91 (2003), and references therein.

[6] O. Mauron and J.-Cl. Dousse, Phys. Rev. A **66**, 042713 (2002).

[7] C. J. Powell, Rev. Mod. Phys. **48**, 33 (1976).

[8] E. J. McGuire, Phys. Rev. A **16**, 62 (1977).

[9] M. Gryziński, Phys. Rev. **138**, A336 (1965).

[10] C. S. Campos, M. A. Z. Vasconcellos, X. Llovet, and F. Salvat, Phys. Rev. A **66**, 012719 (2002).

[11] K. Słabkowska and M. Polasik, J. Phys. Conf. Ser. **58**, 263 (2007).

[12] M. Polasik, K. Kozioł, K. Słabkowska, M. Czarnota, and M. Pajek, J. Phys. Conf. Ser. **163**, 012050 (2009).

[13] S. Segui, M. Dingfelder, and F. Salvat, Phys. Rev. A **67**, 062710 (2003).

[14] C. S. Campos, M. A. Z. Vasconcellos, J. C. Trincavelli, and S. Segui, J. Phys. B **40**, 3835 (2007).

[15] D. V. Davis, V. D. Mistry, and C. A. Quarles, Phys. Lett. **38A**, 169 (1972).

[16] W. Cao, J. Hoszowska, J.-Cl. Dousse, Y. Kayser, M. Kavčič, M. Žitnik, K. Bučar, A. Mihelič, J. Szlachetko,

and K. Słabkowska, Phys. Rev. A **80**, 012512 (2009).

[17] J. Hoszowska, J.-Cl. Dousse, J. Kern, and C. Rhême, Nucl. Instrum. Methods Phys. Res. B **376**, 129 (1996).

[18] R. D. Deslattes, E. G. Jr. Kessler., P. Indelicato, L. de Billy, E. Lindroth, and J. Anton, Rev. Mod. Phys. **75**, 35 (2003).

[19] K. Słabkowska and M. Polasik, Radia. Chem. Phys. **75**, 1471 (2006).

[20] F. P. Larkins, J. Phys. B: At. Mol. Opt. Phys. **4**, IB (1971).

[21] S. L. Sorensen, S. J. Schaphorst, S. B. Whitfield, B. Crasemann, and R. Carr, Phys. Rev. A **44**, 350 (1991).

[22] T. D. Thomas, Phys. Rev. Lett. **52**, 417 (1984).

[23] P.-A. Raboud, M. Berset, J.-Cl. Dousse, Y.-P. Maillard, O. Mauron, J. Hoszowska, M. Polasik, and J. Rzadkiewicz, Phys. Rev. A **65**, 062503 (2002).

[24] T. Mukoyama and K. Taniguchi, Phys. Rev. A **36**, 693 (1987).

[25] K. G. Dyall, J. Phys. B **16**, 3137 (1983).

[26] http://physics.nist.gov/PhysRefData /Star/Text/contents.html.

[27] http://physics.nist.gov/PhysRefData /Star/Text/programs.html.

[28] J. M. Rost and T. Pattard, Phys. Rev. A **55**, R5 (1997).

[29] T. Pattard and J. M. Rost, Phys. Scr. **T80**,

295 (1999).

[30] T. Pattard, J. Phys. B **35**, L207 (2002).

[31] T. F. Coleman and Y. Li, SIAM J. Optim. **6**, 418 (1996).

[32] M. Dingfelder, S. Segui, and J. M. Fernández-Varea, Phys. Rev. A **77**, 062710 (2008).

[33] Z. An and Q. Hou, Phys. Rev. A **77**, 042702 (2008).

[34] R. Diamant, S. Huotari, K. Hämäläinen, C. C. Kao, and M. Deutsch, Phys. Rev. Lett. **84**, 3278 (2000).

[35] W. Cao, J.-Cl. Dousse, J. Hoszowska, M. Žitnik, M. Kavčič, and K. Bučar, Phys. Rev. A **81**, 012501 (2010).

[36] J. L. Campbell, At. Data Nucl. Data Tab. **85**, 291 (2003).

[37] K. Fennane, J.-Cl. Dousse, J. Hoszowska, M. Berset, W. Cao, Y.-P. Maillard, J. Szlachetko, M. Szlachetko, and M. Kavčič, Phys. Rev. A **79**, 032708 (2009).

[38] J. L. Campbell and T. Papp, At. Data Nucl. Data Tab. **77**, 1 (2001).

Part 4.

High-resolution KMM radiative Auger emission spectra of calcium induced by synchrotron radiation

W. Cao[1], M. Kavčič[2], J.-Cl. Dousse[1], M. Berset[1], K. Bučar[2], M. Budnar[2], Y.-P. Maillard[1], K. Fennane[1], J. Hoszowska[1], J. Szlachetko[3,4], M. Szlachetko[1], and M. Žitnik[2]

[1] *Department of Physics, University of Fribourg, Ch. du Musée 3, Ch-1700 Fribourg, Switzerland*

[2] *J. Stefan Institute, P.O. Box 3000, SI-1001 Ljubljana, Slovenia*

[3] *European Synchrotron Radiation Facility (ESRF), F-38043 Grenoble, France*

[4] *Institute of Physics, Jan Kochanowski University, 25-406 Kielce, Poland*

I. INTRODUCTION

The decay scheme of atomic inner-shell vacancies is branched into cascades of radiative fluorescence and non-radiative-Auger electron transitions. The radiative Auger (RA) effect represents an additional decay channel in which the transition energy is shared between the photon and electron that are emitted simultaneously. This alternative weak deexcitation channel was predicted by Bloch and co-workers in the 1930s [1, 2] and detected by Åberg and Utriainen only about 35 years later [3].

For the most probable K RA transitions, which are addressed in this work, the emitted photon energy E_e^A is given by

$$E_e^A = E[K^{-1}] - E[M^{-1}M^{-1}(nl, \epsilon l)], \quad (1)$$

where the first term represents the energy of an ion with a single hole in the K-shell and the second term represents the energy of the final configuration state with two holes in M-shell and one electron either in an unoccupied bound state nl (shake-up) or in the continuum with an energy ϵ (shake-off). The RAE signal appears therefore on the low-energy side of the diagram $K-M_{2,3}$ ($K\beta_{3,1}$) line. The onset energy of RAE corresponds to zero kinetic energy of the electron and the continuous distribution of emitted photon en-

ergies extends to $E^A = 0$, when the energy of the ejected electron equals the energy of the Auger electron emitted by the nonradiative $K-MM$ transition ie.,

$$\epsilon = E[K^{-1}] - E[M^{-1}M^{-1}]. \quad (2)$$

The negative offset from the diagram line is thus given by

$$\triangle E_e^A = E[M_{2,3}] - E[M^{-1}M^{-1}(nl, \epsilon l)], \quad (3)$$

where $E[M_{2,3}]$ is the $M_{2,3}$ electron binding energy. The smallest RAE energy offset occurs when nl corresponds to the lowest unoccupied state. The energy sharing between the continuum electron and the photon is strongly asymmetric [4], and leads to the onset of the RAE shake-off signal at

$$\triangle E_e^A \approx E[M_{2,3}] - E[M^{-1}M^{-1}], \quad (4)$$

corresponding to $\epsilon \approx 0$.

Since in the RA transition the energy is shared between the photon and the electron which is shaken off or excited into higher unoccupied states it is expected that the RA x-ray emission spectra should reflect the structure of the unoccupied states. Indeed, it was confirmed by Kawai that the structure of the $KL_{2,3}L_{2,3}$ RA transitions resembles the K x-ray absorption near edge structure (XANES) [5]. This so-called extended x-ray emission

fine structure (EXEFS) method was successfully applied to study the electronic structure of several elements and compounds [6]. Regarding the intensity of the RA x-ray yield relative to the parent diagram line, a decrease with the atomic number Z is predicted by theory [7, 8]. For a given initial inner-shell vacancy, the relative RA x-ray emission yield increases with the principal quantum number of the electrons involved in the transitions because of the higher shake probability for the less bound outer shell electrons. However, large discrepancies exist between the existing experimental data and the available shake-off (up) [7], configuration interaction (CI) [9], DV-X$_\alpha$ [10], and radiative field calculations [11, 12] for the relative intensities as well as for the RA x-ray emission spectral shapes.

Within the RAE spectral region other processes such as the radiative electron rearrangement (RER) [13] and the satellite and hypersatellite lines due to multiple ionization processes may contribute to the overall signal. When using tunable synchrotron radiation the contribution from multiple ionization, which depends on the incident photon energy [14–16], can be reduced by a tuning the excitation energy just above the ionization threshold. For near-threshold excitation energies, however, the RAE signal may also partially overlap with the x-ray Raman structures [17].

Since the RAE transitions are much less intense than the diagram x-ray lines and are situated on their low energy tail, the RA x-ray spectra are measured by means of the wavelength dispersive x-ray spectroscopy technique. To date, experiments based on photoexcitation employing x-ray tubes [18–20] or charged particle excitation [21, 22] have been carried out. In these studies the effect of multiple ionization contributing to the signal within the RA spectral region can not be excluded.

Among the different K RA contributions the strongest one is the KMM RA transition appearing on the low energy tail of the K–M diagram line, and for this reason it was selected for our study. The pure solid Ca target was excited with monochromatic synchrotron radiation with photon energies tuned at 50 eV and 1455 eV above the Ca K absorption edge. In order to evaluate accurately the background underlying the RA x-ray emission signal, a broad spectral region comprising the $K\alpha_{1,2}$ (K–$L_{3,2}$) and $K\beta_{1,3}$ diagram lines was collected. To extract the RA x-ray emission spectral structure and to determine the relative yield a fit of the whole K x-ray spectrum was performed.

II. EXPERIMENT

The measurements were carried out at the x-ray microscopy beamline ID21 of the ESRF, Grenoble, France. The primary x-ray beam from the undulator was monochromatized by means of a double-crystal Si (111) monochromator and the higher harmonics were reduced with a Ni-coated mirror. The relative beam energy resolution was $\sim 2 \times 10^{-4}$. The beam energies were calibrated with the K-edge energies of Ca, Sc, Ti and V [23]. Two calcium foils, one for the absorption and another for the emission spectra measurements, were prepared beforehand and transported in vacuum.

The calcium K-edge absorption spectrum was measured in the fluorescence mode in the energy interval of 4017 eV to 4135 eV. For the x-ray emission measurements, a curved-crystal von Hamos spectrometer [24] was installed in the main experimental hutch of ID21, downstream of the scanning x-ray microscope chamber to which it was connected with a 180 cm long evacuated pipe sealed with a 50 μm thick Kapton$^{\text{TM}}$ foil. In order to maximize the intensity and to avoid the modification of the signal due to the inhomogeneous beam profile seen on the target through the slit system of the spectrometer, a 200 μm pinhole was inserted in the primary beam and the slit of the spectrometer was left completely open. In such a configuration the energy resolution of the spectrometer is determined mainly by the size (width) of the beam on the target.

Fig. 1 shows the top view of the experimental setup. A 5.1 mg/cm^2 foil was mounted in the evacuated chamber with its surface perpendicular to the incoming beam ($\theta_1 = 90^\circ$). The emitted photons were diffracted in first order by a cylindrically curved LiF(200) crystal and recorded with a thermoelectrically cooled (-50 °C) back-illuminated CCD camera consisting of 1340 $\times$ 400 pixels with a pixel size of 20×20 μm^2. Depending on the central Bragg angle θ, the detector covered an energy range of 83 eV to 97 eV. Thus, to record the whole RA spectrum together with the $K\alpha_{1,2}$ and $K\beta_{1,3}$ diagram lines, four different detector positions were required. The neighboring positions were chosen to have a 20 $\sim$ 30 eV overlap, in order to ensure normalization of the x-ray spectra measured at different detector positions.

In order to avoid multiple photon absorption within a single CCD pixel in the measurements of the intense diagram lines, an acquisition time of 1s/image was chosen and in addition the beam intensity was attenuated by inserting a 25 μm thick Ti absorber and a 90 μm thick Al absorber in the beam for the $K\alpha_{1,2}$ and $K\beta_{1,3}$ measurements, respectively.
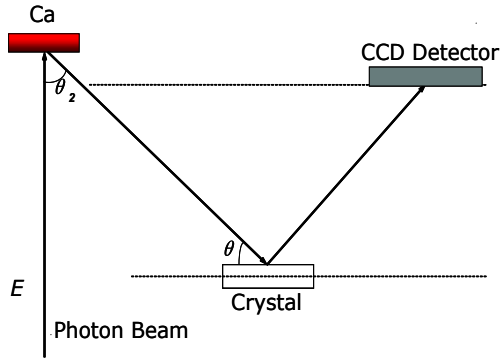
FIG. 1: (Color online) Top view of the experimental set-up used in this work (see text for further details).

For the weak RA x rays near to the $K\beta_{1,3}$ line the exposure times were 1s/image, while the remaining RA spectrum was measured with an acquisition time of 2s/image. For normalization purposes, the incident photon fluxes were recorded with a photodiode before and after each measurement. The diode was calibrated according to the Deutsches Institut für Normung e.V. standard. The photon fluxes on the target without absorbers were typically $3 - 6 \times 10^{11}$ photons/s.

The incident photon beam energy was tuned to 4088 eV, that is 50 eV above the K absorption edge and below the KL and KK double ionization thresholds. At the same time this energy was high enough to avoid the KM resonant Raman scattering contribution to the RAE region. Another beam energy of 5493 eV, which is above the KL double ionization threshold, was employed to check the

effect of multiple ionization and also to test for any excitation energy dependence. The total acquisition time for a single spectrum was ~ 8 hours yielding very good statistics in the RA emission spectrum. The absolute emission energy scale was calibrated using the reference energies of the elastic peak scattered by V (or Ti) targets and the calcium $K\alpha_1$ energy given by Ref. [23].

III.   DATA ANALYSIS

A.   Data corrections

The measured x-ray spectra $Y_N(E_e)$ were first normalized by the photon flux and the overall acquisition time, and then corrected for the target self-absorption factor F_{SA}, the CCD quantum efficiency $F_{\mathbf{CCD}}$, the crystal reflectivity F_{CT}, and the acceptance solid angle Ω of the detector. As all these factors depend on the x-ray emission energy E_e, the final intensities Y were deduced using the following relation

$$Y(E_e) = \frac{Y_N(E_e)F_{SA}(E_e)}{\Omega(E_e)F_{\mathbf{CCD}}(E_e)F_{CT}(E_e)}. \quad (5)$$

The self-absorption correction factor was calculated as:

$$F_{SA}(E_e) = \frac{[\mu_E/\cos\theta_1 + \mu(E_e)/\cos\theta_2]t}{1 - \exp[-(\mu_E/\cos\theta_1 + \mu(E_e)/\cos\theta_2)t]}. \quad (6)$$
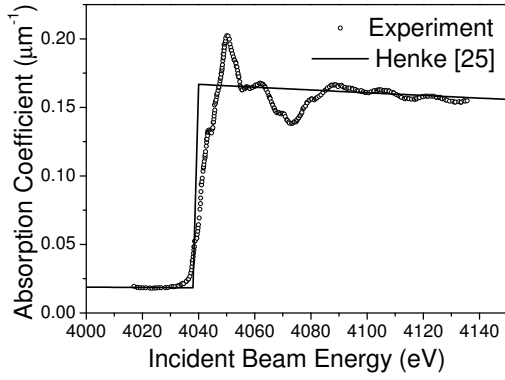
FIG. 2: Experimental (open circle) and theoretical (solid line) x-ray absorption coefficients for solid calcium in the unit of μm^{-1}.

In the above equation, t is the target thickness, and θ_1 and θ_2 are the angles of incident and fluorescence photon beams with respect to the normal to the sample surface. In the geometry applied in our experiment, $\cos\theta_2 = \sin\theta$, where θ is the Bragg angle. μ_E and μ stand for the attenuation coefficient at the incident-beam energy E and x-ray emission energy E_e, respectively.

For the μ_E coefficient the theoretical value from Ref. [25] was adopted. An analytical power-law from [26, 27]

$$\mu(E_e) = a_e(E_e)^{b_e}, \qquad (7)$$

was used to calculate the μ coefficient as a function of x-ray emission energy. In this function a_e and b_e are the fit-parameters to the calculated values from Ref. [25] in the K pre-edge energy region.

Although the major part of x-ray emission energies, including the whole RA structure of primary interest, are situated below the K absorption edge, the high energy part of the spectrum above the $K\beta$ diagram line, particularly the $K\beta_5$ ($K - M_{4,5}$) line, is affected by the an increased self-absorption due to the vicinity of the K absorption edge. In order to avoid the step-function-like correction factor $F_{SA}(E_e)$ given by the theoretical values, the experimental absorption spectrum was used instead. The absorption spectrum was rescaled to the theoretical data from [25] above the K XANES region to get the experimental x-ray attenuation coefficients. The result of this scaling procedure, depicted in Fig. 2, exhibits a good general agreement between our measured absorption spectrum and the theoretical values. These experimental attenuation coefficients were than used to calculate the $F_{SA}(E_e)$ correction factors in the near K absorption edge region.

The $F_{\mathbf{CCD}}(E_e)$ detector efficiency factor was calculated for the back-illuminated silicon CCD detector using equation from [28],

$$F_{\mathbf{CCD}}(E_e) = C_D \left[1 - \exp(-\frac{10^6 X_{Si}}{6.67(1 + \frac{E_e}{1000})^{3.14615}}) \right].$$
$$(8)$$

Here C_D is the detector response constant and X_{Si} is the effective thickness of the Si layer of CCD in cm, which for our particular CCD camera amounts to ~ 0.0015 cm [29].

The LiF (200) crystal reflectivity was calculated by the XOP program [30] for eight emission energies between the $K\alpha_{1,2}$ and $K\beta_{1,3}$ lines and then fitted with a 2nd-order polynomial to obtain the reflectivity correction function $F_{CT}(E_e)$.

B. Spectra fitting

The Ca K x-ray spectra measured at two different photon energies are presented in Fig. 3. Both spectra are dominated by the $K\alpha_{1,2}$ and $K\beta_{1,3}$ diagram lines. There is also the $K\beta_5$ satellite contribution present in both spectra but here we are mainly interested in the broad RA structure on the low energy tail of the $K\beta_{1,3}$ line.

In the fitting model employed to analyze the measured spectra we need to consider that the diagram transitions may be accompanied by satellite lines resulting from additional vacancies present in outer subshells via shake processes [31]. Due to the reduced screening of the nuclear charge in the multi-ionization process, the x-ray satellite lines are shifted in energy with respect to the diagram transitions. The multiconfiguration Dirac-Fock (MCDF) calculations [32] show that the first-order N-satellites are not resolved from the $K\alpha_{1,2}$ and $K\beta_{1,3}$ parent lines. This overlap of the KN satellite transitions with the parent diagram lines results in a non-

lifetime broadening of the latter. The first-order M-satellites, on the other hand, make the diagram lines asymmetric. In contrast, the $KL_{2,3}L$ and $KM_{2,3}L$ satellite transitions whose average energies are ∼24 eV and ∼46 eV above their parent diagram transitions are well resolved in the spectrum taken at 5493 eV excitation energy above the KL double ionization threshold.

The spectra were fitted with the least-square fitting program Peakfit™. The spectrum measured at 4088 eV shows a small asymmetry in the $K\alpha_{1,2}$ diagram line. Although the beam energy is lower than the KL double ionization threshold it is high enough to induce the KN and KM double excitation/ionizations. Thus, each of the $K\alpha_{1,2}$ lines was fitted by four Voigtians, all having the same Gaussian width. Two Voigtians, with their Lorentzian widths taken from the recommended values by Campbell and Papp [33], were employed to distinguish the pure $K - M_{2,3}$ transitions from the satellite lines, whose Lorentzian widths were free fitting parameters. The obtained fitting parameters were then fixed and the tails from the $K\alpha_{1,2}$ subtracted. For the $K\beta_{1,3}$ x-ray spectra, the fitting procedure was similar as for the $K\alpha$ region, except for the Lorentzian widths of the $K\beta$ lines which were left free due to higher uncertainties in the M-shell widths resulting from the strong overlap between the

$M_{2,3}$ and $M_{4,5}$ levels [34]. In addition, much larger widths of the $K - M_{2,3}$ transitions result in an overlap with the KM and KN satellites. The fitted curve and the individual peak components are plotted in Fig. 3(a) in a logarithmic scale to emphasize the weak structures. The importance of including the whole K x-ray spectrum in the fitting procedure in order to determine properly the shape and the background level below the weak RA signal is clearly seen in Fig. 3

The spectrum recorded at the higher beam energy $E = 5493$ eV was analyzed in a similar way. Both diagram lines exhibit a slightly larger asymmetry due to an increased contribution from the KM and KN multi-ionization satellite lines. As a consequence, an additional peak was employed to fit the $K\beta_{1,3}$ line. Further, as the excitation energy was above the KL ionization threshold, additional peaks were needed to account for the $K\alpha L$ and $K\beta_{1,3}L$ satellite lines appearing in the spectrum (see Fig. 3(b)). A value of 23.8(2) eV was extracted for the energy shift of the $K\alpha_1 L$ satellite line relative to the $K\alpha_1$ diagram line, a slightly higher value than previously reported 22.4(8) [35] and 22(2) eV [36]. For the energy shift of the $K\beta_{1,3}L$ satellite line relative to the $K\beta_{1,3}$ diagram line, a value of 46.6(3.8) eV was extracted from our fit in good agreement with the theoretical value 48.7 eV calculated with the GRASP code [32].

IV. RESULTS AND DISCUSSION

The residual spectra $Y_R(E_e^R)$ as a function of the re-scaled E_e^R energy relative to the $K\beta_{1,3}$ peak energy are shown in Fig. 4. The obtained intensity is of the order of 10^{-3} relative to the $K\alpha_{1,2}$ diagram lines and 10^{-2} relative to the $K\beta_{1,3}$ lines, respectively. Despite a very good fit of the overall spectra (typical $\tilde{\chi}^2 \approx 0.999$), the propagation of uncertainties from the diagram and satellite peaks resulted in a non-negligible error in the RA energy region. The final uncertainties were deduced from the data corrections, the statistical errors of the measurements, and the subtraction procedures. The estimated errors are also depicted in Fig. 4.

A. KMM RA shape

In general, the shape of the RA spectra measured at the two different excitation energies is very similar and the same onset energy of $E_s = -22.9(1)$ eV was found for the leading edge of the KMM RA transitions. In the spectrum taken at $E = 5493$ eV, some of the main structures are slightly less well resolved. Since the photon energy is above the KL double ionization threshold, this can be due to additional broadening resulting from
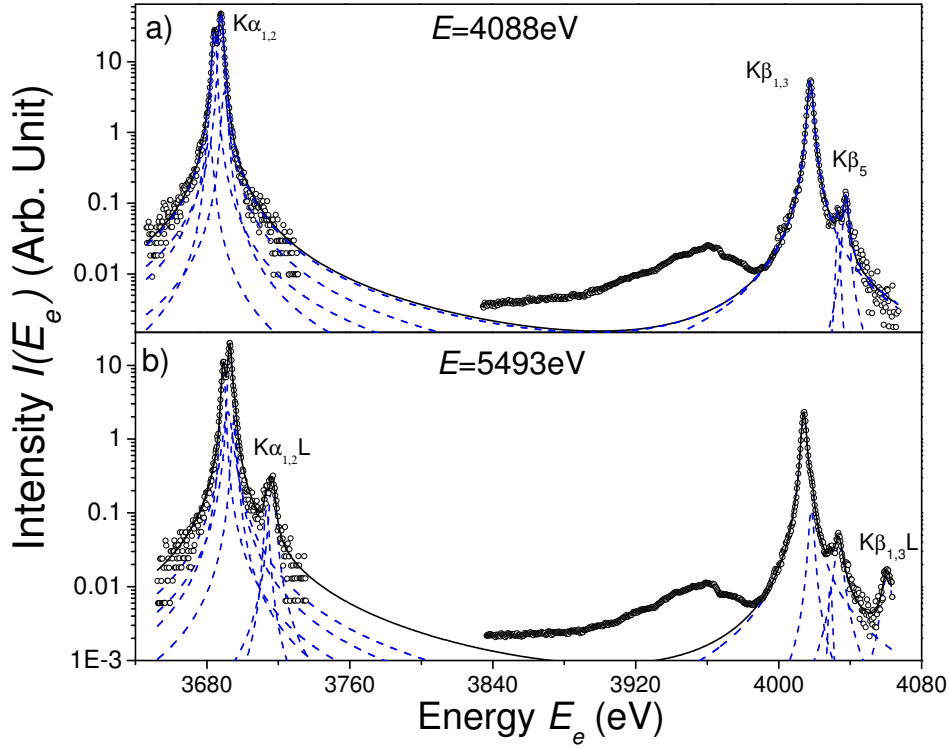
FIG. 3: (Color online) Fitted high-resolution K x-ray spectra of Ca at two different incident-beam energies, (a) E =4088 eV and (b) E=5493 eV. Solid thick lines represent the total fit to the experimental data (open circles) and dashed lines the individual components. Besides the diagram lines labeled in (a), additional satellite peaks on the high energy side of the $K\alpha_{1,2}$ lines and $K\beta_5$ lines correspond to the $K\alpha_{1,2}L$ ($K^{-1}L^{-1}$–L^{-2}) and $K\beta_{1,3}L$ ($K^{-1}L^{-1}$–$M^{-1}L^{-1}$) satellite transitions, respectively.

multi-ionization processes. As both excitation energies are below the double K ionization threshold energy of 8003 eV [35], the spectra are free from the $K\alpha_{1,2}^h$ hypersatellite lines appearing in the proton excited spectrum [21] at the energy of -173.5(6) eV. The contributions from the resonant x-ray Raman scattering and RER transitions were found to be negligibly small in comparison with the RA intensity for calcium [37], and were not taken into consideration in the present work.

The RA transition process involves also the unoccupied nl states in the outer shells. In general, we can distinguish four possible series of the KM_iM_jnl RA transitions, namely, $KM_{2,3}M_{2,3} - np$, $KM_1M_{2,3} - nd$, $KM_1M_{2,3} - ns$, and $KM_1M_1 - np$. The RA spectrum should therefore exhibit fine structures reflecting the density of unoccupied states (DOS) as it has been already ob-
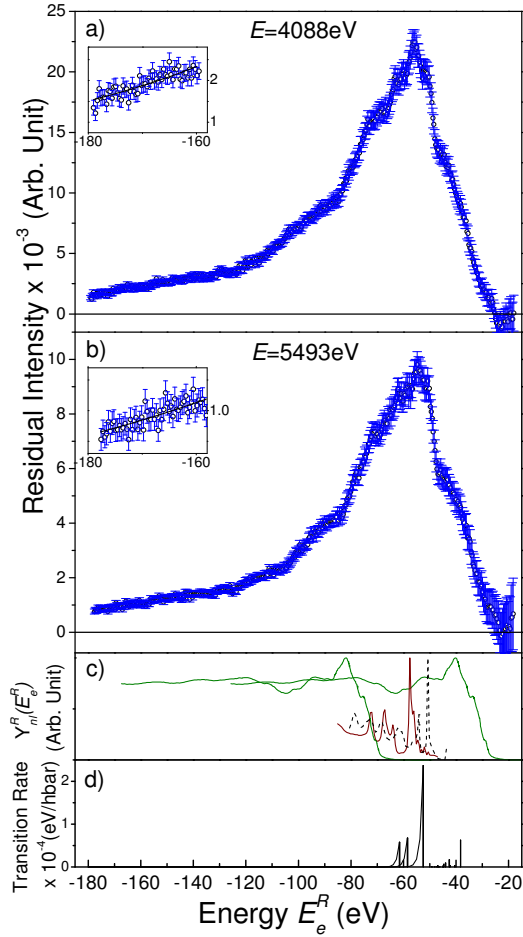
FIG. 4: (Color online) The residual intensities of the fitted high-resolution K x-ray spectra of calcium measured at two beam energies: (a) E = 4088 eV and (b) E = 5493 eV. The insets represent the least-square fits (solid lines) of the exponential slope to the measured residuals (open circles) in the lowest 20 eV energy range. These were used to evaluate the missing RA intensity on the low energy side. The panel (c) shows the realigned nl density of unoccupied states, green solid line for np ($n{\geq}4$), black dashed line for nd ($n{\geq}3$) and wine solid line for ns ($n{\geq}5$), respectively. In the lowest panel (d), the theoretical radiative field transition rates from Baptista [12] are shown as sticks for the main discrete contributions and by an exponential decay for the continuum final states.

served by Kawai *et al.* [5, 6, 38] (the so-called EXEFS method). Neglecting the quadruple transitions [39] and the crystal field effects [40], the measured K absorption spectrum corresponds to the p states DOS considered in our work. For the s- and d- states DOS, theoretical calculations for CaS [41] were adopted. The measured K-edge absorption spectrum was aligned relative to the Fermi level energy $E = 4038.2$ eV, which was determined from the first-order derivative of the experimental curve.

For a meaningful comparison with the measured RA spectrum, the normalized nl DOS were aligned to a common energy scale using the following relation and taking the energy of the $K\beta_{1,3}$ line as reference:

$$Y_{nl}^{R}(E_{e}^{R}) = Y_{nl}(E_{i} - E_{M_{2,3}} + E_{j} - E_{nl}). \quad (9)$$

In the above equation, E_{i} and $E_{M_{2,3}}$ are the calcium M_{i} and $M_{2,3}$ electron binding energies. E_{j} is the binding energy of the outgoing electron calculated within the $Z + 1$ approximation [42]. The recommended values from the X-ray Data Booklet [43] were adopted for the binding energies with respect to the Fermi level. The re-scaled K absorption spectrum and the d- and s- DOS are depicted the (c) panel of Fig. 4. The positions of the peaks are listed as the EXEFS values in the 2nd column of Table I. The

Arabic numbers are employed to distinguish the strongest RA transitions which involve the lowest unoccupied states in each series.

Figure 4 shows some qualitative agreement of the measured RA spectra with the corresponding DOS curves. For more quantitative comparison the leading peaks of each corresponding DOS curve are tabulated in the second column of Table I. The first column of the Table I lists all possible shake-up KMM RAE dipole transitions following the selection rules proposed by Bloch [1] and Aberg [7]. The corresponding transition energies calculated with the DV-$X\alpha$ [10] and the radiative field method [12] are given in the 3rd and 4th column, respectively. Finally, the RAE leading edge energies calculated via the LMM Auger transitions energies [44] are also listed in the 5th column of the table.

B. Relative RA yield

Since it is very important to evaluate properly the tails of the $K\alpha_{1,2}$ and $K\beta_{1,3}$ diagram lines producing the background underlying the RA signal, the relative yield of the $K\beta_{1,3}$ and $K\alpha_{1,2}$ lines were used to check the normalization procedure of the separate spectral regions as well as the different corrections applied to the measured intensities. The same value (given in Table II) was obtained for both spectra, lower than the the-oretical calculation from Scofield [8], but in agreement with his later result of 0.107 [45] and the experimental value of 0.105(5) [46]. The Lorentzian widths of the $K\beta_{1,3}$ diagram line extracted from the fit are consistent with the values recommended by Campbell and Papp [33]. A slight systematic overestimation is attributed to the unresolved N-satellites which broaden the diagram line distributions.

The total RA yield was determined by integrating the measured spectra presented in Fig. 4 in the E_l to the E_s emission energy interval. However, we can notice in Fig. 4 that even after careful background subtraction we have not yet reached zero intensity on the lower edge E_l of our measured emission energy interval. The missing RA intensity on the low energy side was evaluated as

$$Y_R = \int_{-E_{K\beta_{1,3}}}^{E_l} a_R \exp[b_R E_e^R] \, dE_e^R, \qquad (10)$$

employing exponential functions to describe analytically the trend of the RA x-ray tail distribution according to the first approximation of the Auger electron escape process [47]. In this equation, a_R and b_R are the least-square-fit parameters to the residuals in the lowest 20 eV energy interval. The fit results are depicted in the insets of Fig. 4. The contribution of this part to the total RA intensity was found to be $\sim 5\%$ and was added to the measured intensities. The total RA inten-

TABLE I: The calcium KMM radiative Auger transition energies for different final state configurations relative to the $K\beta_{1,3}$ diagram lines (eV). The initial configuration is Ca$(1s)^{-1}$ $^2S^e$. The theoretical calculations of the DV-$X\alpha$ [10], the radiative field [12], and the values deduced from the Auger transition energies [21] are listed for comparison.

KMM-RAE final configuration	EXEFS[a]	DV-$X\alpha$[10]	Radiative field [12]	Transition Edge [21]
$(3p)^{-2}$ ^3P $4p$ $^2P^o$		-41	-38.3	-31.2
$(3p)^{-2}$ ^1D $4p$ $^2P^o$	-40.1	-43	-40.5	-33.4
$(3p)^{-2}$ ^1S $4p$ $^2P^o$		-47	-42.3	-35.3
$(3p)^{-2}$ ^3P $(n \geq 5)p$ $^2P^o$		-46	-43.5[a]	
$(3p)^{-2}$ ^1D $(n \geq 5)p$ $^2P^o$		-48	-46.4[a]	
$(3p)^{-2}$ ^1S $(n \geq 5)p$ $^2P^o$		-52	-47.7[a]	
$(3s3p)^{-1}$ ^3P $3d$ $^2P^o$	-50.7	-	-	-48.0[b]
$(3s3p)^{-1}$ ^1P $3d$ $^2P^o$		-	-	
$(3s3p)^{-1}$ ^3P $(n \geq 4)d$ $^2P^o$		-	-	
$(3s3p)^{-1}$ ^1P $(n \geq 4)d$ $^2P^o$		-	-	
$(3s3p)^{-1}$ ^3P $5s$ $^2P^o$	-57.6	-55	-	-56.7[b]
$(3s3p)^{-1}$ ^1P $5s$ $^2P^o$		-62	-	
$(3s3p)^{-1}$ ^3P $(n \geq 6)s$ $^2P^o$		-64	-	
$(3s3p)^{-1}$ ^1P $(n \geq 6)s$ $^2P^o$		-71	-	
$(3s)^{-2}$ ^3S $4p$ $^2P^o$	-81.8	-	-	-73.4[b]
$(3s)^{-2}$ ^1S $4p$ $^2P^o$		-	-	
$(3s)^{-2}$ ^3S $(n \geq 5)p$ $^2P^o$		-	-	
$(3s)^{-2}$ ^1S $(n \geq 5)p$ $^2P^o$		-	-	

[a] The average value for $n \geq 5$ final state configuration.
[b] The average value for the final state configuration.

sities were then divided by the corresponding $K\beta_{1,3}$ intensities to get the relative RA yields R_M, which are listed in the 4th row of Table II.

These values were further corrected for the second order $(KM - (Mnl)(Mn'l'))$ RA process which might contribute slightly to the low energy part of our KMM RA spectrum. Assuming the same relative transition yield R_c for the first order RA KMM to the $K\beta_{1,3}$ diagram line and the second order $KMMM$ to the first order KMM RA emission lines,

the measured ratio of R_M can be written as

$$R_c^2 + R_c = R_M. \tag{11}$$

The positive solutions of the above equation for R_c yield the final RA intensities listed in the bottom line of the Table II. The corrections of less than 6% indicate the negligible influence of higher orders KMM RA processes to the final RA intensities.

The difference of the relative KMM RA yield obtained for spectra measured at two excitation energies was within the experi-

TABLE II: The relative $K\beta_{1,3}$ versus $K\alpha_{1,2}$ yields, the fitted Lorentzian widths for the $K\beta_{1,3}$ diagram lines, the measured relative KMM RA intensity versus the $K\beta_{1,3}$ intensity, and the corrected RA rates for the two incident beam energies of 4088 eV and 5493 eV.

	4088 eV	5493 eV	Reference
$Y_{K\beta_{1,3}}/Y_{K\alpha_{1,2}}$	0.098(1)	0.103(3)	0.126 [8]
Lorentzian Width (eV)	2.09(8)	2.22(15)	1.97(20) [33]
R_M	0.055(4)	0.058(5)	-
R_c	0.052(3)	0.055(5)	0.056^a [8]

^{a}The contribution of the double hole creation process during the $K\beta_{1,3}$ transition.

mental error, suggesting the independence of the RAE intensity on the excitation energy. The quoted intensity of 0.053(3) represents an average value from the two measurements. Compared to other experimental results our value exceeds significantly the proton-induced relative KMM RA intensity of 0.031(5) [21], the x-ray tube induced value of 0.016(6) [19], as well as the recent theoretical predictions of Baptista [12]. On the other hand, the reported value is in agreement with the theoretical ratio for the total double vacancy production with single $K - 3p$ transitions predicted by Scofield [8], and the theoretical Z dependence reported by Åberg [7]. The theoretical curve for the double vacancy production with single $K-3p$ transitions taking into account only the $3s$ and $3p$ vacancies [8, 37, 48] slightly underestimates our experimental value. In order to get a more general
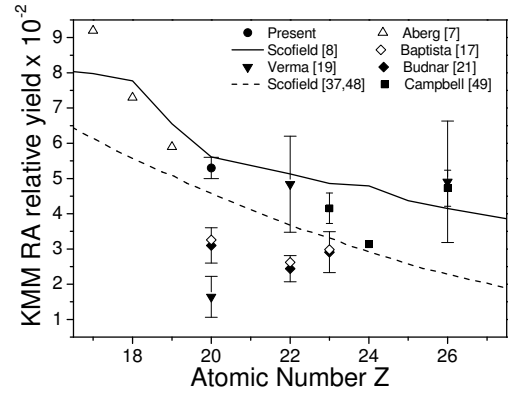

FIG. 5: Present experimental KMM RA yield for calcium compared to experimental values from Ref. [19] and Ref. [21], and theoretical values from Scofield for the total KM RA transition possibilities [8] (solid line) and only for the $3s$ and $3p$ rates (dashed line) [37, 48]. The calculations for the neighboring elements of Cl$^-$ (Z=17), Ar (Z=18) and K$^+$ (Z=19) [7], and the set of experimental results for neighboring elements V ($Z = 23$), Cr ($Z = 24$) and Fe ($Z = 26$) from [49] are also shown for comparison.

view of the KMM RA relative intensity in this Z region, the existing experimental data for neighboring elements obtained with x-ray fluorescence method [19, 37, 48], MeV proton excitation [21] and intensities obtained from the measurements of the $K\beta/K\alpha$ ratios in radionuclides following electron capture [49] are compiled in Fig. 5. Three sets of theoretical predictions already mentioned above are also shown in the figure.

First of all we notice a large scattering of the existing experimental data indicating the presence of systematic errors in different experiments. The general decrease with

increasing atomic number predicted by theory is confirmed by experiments. No systematic differences between experimental data obtained for different ionization modes can be observed supporting the independence of the RA emission on the mode of excitation. Our result is the only one so far obtained in an experiment employing monochromatic synchrotron radiation for excitation. In addition, the energy resolution of our RAE measurements is around 1 eV and is superior to the previous experiments with a moderate resolution of a few eV. This plays an important role in an accurate determination of the tails from both the $K\alpha_{1,2}$ and $K\beta_{1,3}$ diagram lines producing the background underneath the broad RA structure. We believe that the difficulties connected with this background subtraction are the main source of large discrepancies between the experimental data. Additional measurements for other elements following the method used in our work are clearly needed for reliable comparisons and conclusions. Despite the high energy resolution of the measured emission spectra no distinct structure due to discrete shake-up excitations to higher unoccupied outer shells could be observed, most likely due to the solid state effects which broaden and modulate the RAE structure.

V. CONCLUSION

We have reported on the photoinduced KMM radiative Auger emission spectra for calcium recorded at two different excitation energies and with a high energy resolution in the detection channel. Tunable monochromatic photon beams allowed to selectively exclude contributions to the RA spectral region from other possible processes. The high energy resolution and low background noise insured a reliable determination of the $K\beta_{1,3}$ diagram line width and the instrumental broadening. This represented a reliable basis for subtraction of the KMM RA contribution from the measured spectra.

For the RA structure, the EXEFS method [5] and the DV-X_α [10] calculations were considered in assigning the peaks in the RAE spectra. While the experimental transition energies were found to agree well with the results of these two models, the observed RA transition edges lied systematically above the values evaluated from the recalculated Auger electron energies [21]. The relative yield of the KMM RA with respect to the $K\beta_{1,3}$ diagram line was found to be 0.053(3), in agreement with the theoretical predictions from Scofield [8, 37, 48].

Differences among the various experimental KMM RA relative yields and theoretical calculations are found. This can be mainly

attributed to the difficulties in an accurate determination of the background which is essential to isolate the RAE contribution. We did not attempt to extract the intensities of the separate RAE shake-up and shake-off transitions from our data. However, the presented spectra would allow a precise comparison with possible new theoretical results despite the difficulties of such calculations due to the complexity of the matrix elements which govern the RA transitions [10].

[1] F. Bloch and P. A. Ross, Phys. Rev. **47**, 884 (1935).

[2] F. Bloch, Phys. Rev. **48**, 187 (1935).

[3] T. Åberg and J. Utriainen, Phys. Rev. Lett. **22**, 1346 (1969).

[4] M. O. Krause, T. A. Carlson, , and R. D. Dismukes, Phys. Rev. **170**, 37 (1968).

[5] J. Kawai, T. Nakajima, T. Inoue, H. Adachi, M. Yamaguchi, K. Maeda, and S. Yabuki, Analyst **119**, 601 (1994).

[6] J. Kawai, Analy. Sci. **21**, 733 (2005).

[7] T. Åberg, Phys. Rev. A **4**, 1735 (1971).

[8] J. H. Scofield, Phys. Rev. A **9**, 1041 (1974).

[9] K. G. Dyall and F. P. Larkins, J. Phys. B **15**, 4103 (1982).

[10] H. Hayashi, N. Watanabe, and Y. Udagawa, J. Phys. : Condens. Matter **8**, 37 (1996).

[11] V. O. Kostroun and G. B. Baptista, Phys. Rev. A **14**, 363 (1976).

[12] G. B. Baptista, J. Phys. B : At. Mol. Opt. Phys. **34**, 389 (2001).

[13] M. Oura, T. Kambara, Y. Kanai, S. Kravis, Y. Nakai, and Y. Awaya, Riken Rev. **4**, 29 (1994).

[14] P.-A. Raboud, M. Berset, J.-Cl. Dousse, Y.-P. Maillard, O. Mauron, J. Hoszowska, M. Polasik, and J. Rzadkiewicz, Phys. Rev. A **65**, 062503 (2002).

[15] J. Hoszowska, A. K. Kheifets, J.-Cl. Dousse, M. Berset, I. Bray, W. Cao, K. Fennane, Y. Kayser, M. Kavčič, J. Szlachetko, et al., Phys. Rev. Lett. **49**, 102 (2009).

[16] T. D. Thomas, Phys. Rev. Lett. **52**, 417 (1984).

[17] J. Tulkki and T. Åberg, J. Phys. B **15**, 435 (1982).

[18] C. Herren and J.-Cl. Dousse, Phys. Rev. A **56**, 2750 (1997).

[19] H. R. Verma, J. Phys. B: At. Mol. Opt. Phys. **33**, 3407 (2000).

[20] D. Mitra, M. Sarkar, D. Bhattacharya, and L. Natarajan, X-Ray Spectrom. **37**, 585 (2008).

[21] M. Budnar, A. Mühleisen, M. Hribar, H. Janžekovič, M. Ravnikar, Ž. Šmit, and M. Žitnik, Nucl. Instrum. Methods Phys.

Res. B **63**, 377 (1992).

[22] S. P. Limandri, A. C. Carreras, R. D. Bonetto, and J. C. Trincavelli, Phys. Rev. A. **81**, 012504 (2010).

[23] R. D. Deslattes, E. G. Jr. Kessler., P. Indelicato, L. de Billy, E. Lindroth, and J. Anton, Rev. Mod. Phys. **75**, 35 (2003).

[24] J. Hoszowska, J.-Cl. Dousse, J. Kern, and C. Rhême, Nucl. Instrum. Methods Phys. Res. A **376**, 129 (1996).

[25] B. L. Henke, E. M. Gullikson, and J. Davis, At. Data Nucl. Data Tab. **54**, 181 (1993).

[26] W. Jitschin and R. Stötzel, Phys. Rev. A **58**, 1221 (1999).

[27] J. Padežnik-Gomilšek, A. Kodre, I. Arčon, and M. Hribar, Phys. Rev. A **68**, 042505 (2003).

[28] J. R. Janesick, *Scientific Charge-Coupled Devices* (SPIE, Washington, 2001).

[29] J. Szlachetko, J.-Cl. Dousse, J. Hoszowska, M. Berset, W. Cao, M. Szlachetko, and M. Kavčič, Rev. Sci. Instrum. **78**, 093102 (2007).

[30] M. S. del Río and R. J. Dejus, *Synchrotron Radiation Instrumentation: Eighth International Conference edited by T. Warwick et al.* (Americal Institute of Physics, 2004).

[31] T. Åberg, Phys. Rev. **156**, 35 (1967).

[32] K. G. Dyall, I. P. Grant, C. T. Johnson, F. A. Parpia, and E. P. Plummer, Comput. Phys. Communicat. **55**, 425 (1989).

[33] J. L. Campbell and T. Papp, At. Data Nucl. Data Tab. **77**, 1 (2001).

[34] R. D. Cowan, *The Theory of Atomic Structure and Spectra* (University of California Press, Berkeley, 1981).

[35] M. Oura, H. Yamaoka, K. Kawatsura, K. Takahiro, N. Takeshima, Y. Zou, R. Hutton, S. Ito, Y. Awaya, M. Terasawa, et al., J. Phys. B: At. Mol. Opt. Phys. **35**, 3847 (2002).

[36] M. Deutsch, Phys. Rev. A **39**, 1077 (1989).

[37] O. Keski-Rahkonen and J. Ahopelto, J. Phys. C **13**, 471 (1980).

[38] J. Kawai, Rigaku J. **15**, 33 (1998).

[39] J. J. Rehr and R. C. Albers, Rev. Mod. Phys. **70**, 621 (2000).

[40] F. M. F. de Groot, J. C. Fuggle, B. T. Thole, and G. A. Sawatzky, Phys. Rev. B **41**, 928 (1990).

[41] A. V. Soldatov, A. N. Kravtsova, M. E. Fleet, and X. Liu, Phys. Scripta **T115**, 323 (2005).

[42] M. H. Chen, B. Crasemann, and H. Mark, Phys. Rev. A **21**, 436 (1980).

[43] G. P. Williams, *Electron binding energies: X-ray data booklet compiled and edited by A. C. Thompson and D. Vaughan* (Lawrence Berkeley National Laboratory, 2001).

[44] F. P. Larkins, J. Phys. B: At. Mol. Opt. Phys. **4**, IB (1971).

[45] J. H. Scofield, At. Data Nucl. Data Tab. **14**,

121 (1974).

[46] N. V. Rao, S. B. Reddy, G. Satyanarayana, and D. L. Sastry, Physca B+C **138**, 215 (1986).

[47] T. Koshikawa and R. Shimizu, J. Phys. D: Appl. Phys. **7**, 1303 (1974).

[48] A. Servomaa and O. Keski-Rahkonen, J. Phys. C **8**, 4124 (1975).

[49] J. L. Campbell, A. Perujo, W. J. Teesdale, and B. Millman, Phys. Rev. A **33**, 2410 (1986).

Acknowledgements

"A journey is best measured in friends, rather than miles."

During the four years of my Ph.D. studies, many people have given me their guidance and help. I would like thus at the end of this thesis to express my thanks to all of them.

First of all, I would like to address my sincere gratitude to Prof. Dr. Jean-Claude Dousse. His supervision was the foundation for all my gains. His integral views, unique insights, abundant experiences and immense knowledge inspired and enriched me as a student, researcher and physicist. Besides his supervision and help in my study, his passions, patience and enthusiasm have influenced and enhanced my own character. It's a pleasure to have the chance of working with him.

I thank Dr. Joanna Hoszowska for all her help and guidance. Her comments and suggestions helped me a lot in learning experimental physics. I have also appreciated her kind and efficient assistance in preparing scientific papers.

I would like to address my appreciations to Prof. Jian-zu Zhang. He has enlarged my horizons and bridged my understanding between the theoretical and experimental physics.

I am very grateful to Dr. Matjaž Kavčič and Dr. Matjaž Žitnik for all their help. Their useful and invaluable discussions and persuasions directed me to a precise and broad understanding of my projects. I deeply appreciate their patience and generosity of sharing the instruments, times, projects and ideas.

I would like to acknowledge Prof. Dr. J. L.(Iain) Campbell from the University of Guelph, Canada, for having accepted to review my Ph.D. thesis.

I would like to thank all colleagues and friends who worked together with me during these years: Michel Berset, Dr. Karima Fennane, Yves Kayser, Yves-Patrik Maillard, Stanislaw Nowak, Jean-Luc Robyr, Jean-Luc Schenker, Dr. Jakub Szlachetko and Dr. Monika Szlachetko. I would like to address my gratitude to Dr. Klemen Bučar, Prof. Dr. Milos Budnar and Dr. Andrej Mihelič from Slovenia and colleagues from Poland. Warm thanks go to my friends from China, Dr. Li Yu, Dr. Tsu-Chien Weng, Prof. Liming He, Prof. Dr. Youhua Luo and Dr. Meng Zhang.

I thank the professors and colleagues in the Physics Department for exchanging ideas and sharing beautiful times. I thank the administrative and workshop staffs of the department for their kindnesses and helps.

Last but not the least, I thank all my friends in and out of Switzerland, without whom, my daily life in Fribourg would have not been colorful. I thank all my family members who have been constantly loving and supporting me. They give me strength when I am weak; they give me persuasions when I am frivolous; they give me encouragements when I am frustrated and they give me applauds when I am progressing.

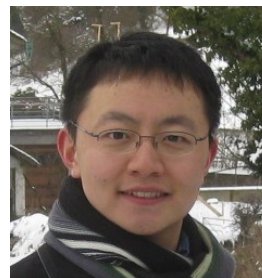# CURRICULUM VITAE

First name: Wei

Last name: CAO

Date of birth: 09 Jul. 1982

Place of birth: Jiangsu, China

Nationality: Chinese

Marital status: Single

EDUCATION

07.2006-11.2010

Physics Department, University of Fribourg, Switzerland

THESIS - L-subshell Coster-Kronig rates of Pd and Xe, electron-induced L_3M double ionization of Pd, and KMM RAE of Ca investigated by means of high-resolution x-ray spectroscopy

09.2003-07.2005

Physics Department, East China University of Science and Technology, China

THESIS - Calculation of Helium $^1D - {}^3D$ term intervals for $1snd$ ($n = 4 \sim 20$) states

07.2002-10.2002

Physics Department, University of Fribourg (Exchange Student), Switzerland

09.1999-07.2003

Physics Department, East China University of Science and Technology, China

English Language Department (Secondary Branch), East China University of Science and Technology, China

DIPLOMAS

Master of Science,   East China University of Science and Technology, China, July 2005

Bachelor of Engineer,   East China University of Science and Technology, China, July 2003

Certificate of Literature, East China University of Science and Technology, China, July, 2003

LIST OF PUBLICATIONS

I. REFERRED ARTICLES

1) W. Cao, J.-Cl. Dousse, J. Hoszowska, M. Žitnik, M. Kavčič, and K. Bučar, Synchrotron-radiation-based determination of Xe L-subshell Coster-Kronig yields: A reexamination with high-resolution x-ray spectroscopy, Phys. Rev. A, **81**(1): 012501 (2010).

2) Y. Kayser, D. Banaś, W. Cao, J.-Cl. Dousse, J. Hoszowska, P. Jagodzinski, M. Kavčič, A. Kubala-Kukuś, S. Nowak, M. Pajek, and J. Szlachetko, Depth profiles of Al impurities implanted in Si wafers determined by means of the high resolution grazing emission x-ray fluorescence technique, Spectrochemica Acta B, **65**(6): 445-449 (2010).

3) J. Hoszowska, A. K. Kheifets, J.-Cl. Dousse, I. Bray, W. Cao, K. Fennane, Y. Kayser, M. Kavčič, J. Szlachetko, and M. Szlachetko, Single-photon double K-shell ionization of low-Z atoms, J. Phys-Conf. Ser., **194**: 022040 (2009).

4) J. Hoszowska, A. K. Kheifets, J.-Cl. Dousse, M. Berset, I. Bray, W. Cao, K. Fennane, Y. Kayser, M. Kavčič, J. Szlachetko, and M. Szlachetko, Double K-shell photoionization of low-Z atoms and He-like ions, Eur. J. Phys-ST, **169**: 23-27 (2009).

5) A. Kubala-Kukus, D. Banaś, W. Cao, J.-Cl. Dousse, J. Hoszowska, Y. Kayser, M. Pajek, M. Salome, J. Susini, J. Szlachetko, and M. Szlachetko, Observation of ultra low-level Al-impurities on silicon surface by high-resolution grazing emission x-ray fluorescence excited by synchrotron radiation, Phys. Rev. B, **80**(11): 113305 (2009).

6) M. Zhang, L. M. He, L. X. Zhao, X. J. Feng, W. Cao, and Y. H. Luo, A density functional theory study of the Au_7H_n (n = 1-10) clusters, J. Mol. Struct.: THEOCHEM, **911**: 61-65 (2009).

7) W. Cao, J. Hoszowska, J.-Cl. Dousse, Y. Kayser, M. Kavčič, M. Žitnik, K. Bučar, A. Mihelič, J. Szlachetko, and K. Słabkowska, L-subshell Coster-Kronig yields of palladium determined via synchrotron-radiation-based high-resolution x-ray spectroscopy, Phys. Rev. A, **80**(1): 012512 (2009).

8) J. Szlachetko, D. Banaś, A. Kubala-Kukus, M. Pajek, W. Cao, J.-Cl. Dousse, J. Hoszowska, Y. Kayser, M. Szlachetko, M. Kavčič, M. Salome, and J. Susini, Application of

the high-resolution grazing-emission x-ray fluorescence method for impurities control in semiconductor nanotechnology, J. Appl. Phys., **105**: 086101 (2009).

9) M. Kavčič, M. Žitnik, K. Bučar, A. Mihelič, M. Štuhec, J. Szlachetko, W. Cao, R. Alonso Mori, and P. Glatzel, Separation of two-electron photoexcited atomic processes near the inner-shell threshold, Phys. Rev. Lett., **102**: 143001 (2009).

10) K. Fennane, J.-Cl. Dousse, J. Hoszowska, M. Berset, W. Cao, Y.-P. Maillard, J. Szlachetko, M. Szlachetko and M. Kavčič, Double K-shell ionization of Al induced by photon and electron impact, Phys. Rev. A, **79**(3): 032708 (2009).

11) J. Hoszowska, A. K. Kheifets, J.-Cl. Dousse, M. Berset, I. Bray, W. Cao, K. Fennane, Y. Kayser, M. Kavčič, J. Szlachetko, and M. Szlachetko, Physical mechanisms and scaling laws of K-shell double photoionization, Phys. Rev. Lett., **102**: 073006 (2009).

12) J. Szlachetko, J.-Cl. Dousse, J. Hoszowska, M. Berset, W. Cao, M. Szlachetko, and M. Kavčič, Relative detection efficiency of back- and front-illuminated charge-coupled device cameras for x-rays between 1 keV and 18 keV, Rev. Sci. Instrum., **78**: 093102 (2007).

13) M. Kavčič, J.-Cl. Dousse, J. Szlachetko, and W. Cao, Chemical effects in the Kβ X-ray emission spectra of sulfur, Nucl. Instrum. Methods Phys. Res. B, **260**: 642-646 (2007).

14) L. M. He and W. Cao, Many-body calculations of helium $^1D - ^3D$ term intervals for $1snd$ ($n = 12 \sim 20$) high Rydberg states. Can. J. Phys., **84**(12): 1097-1106 (2006).

15) W Cao, Y. X. Zhu, H. Lu and L. M. He, Approximate normalization form of the numeric continuum state wave function and the integral processing for the residue of TRK summery, Chin. J. Comput. Phys., **23**(1): 115-119 (2006).

16) L. M. He, W. Cao, X. Q. Chen, and Y. X. Zhu, Calculation of helium $^1D - ^3D$ term intervals for $1snd$ ($n = 4 \sim 11$) states, Act. Phys. Sin., **54**(11): 5077-5081 (2005).

17) Y. X. Zhu, L. M. He, W. Cao, and Z. M. Ge, The magnetic fine structure calculation of helium 10G-10M Rydberg states, Act. Phys. Sin., **54**(11): 5082-5088 (2005).

18) W. Cao, L. M. He, Y. X. Zhu and Z. M. Ge, Deduction of the normalization of continuum state wave functions and its verification via completeness condition, Chin. J. At. Mol. Phys., **22**(3): 524-529 (2005).

19) X. Q. Chen, L. M. He, W. Cao, and Y. X. Zhu, MBPT calculation of $^1D - {}^3D$ splittings in helium Rydberg states, J. East Chin. Uni. Sci & Tech., **30**(6): 706-709 (2004).

20) W. Cao, L. M. He, X. Q. Chen, and Y. X. Zhu, Integral processing for the sum of infinite series in MBPT calculation, Chin. J. At. Mol. Phys., **21**(4): 691-694 (2004).

II.   CONFERENCE ABSTRACTS

1) J.-Cl. Dousse, M. Berset, W. Cao, K. Fennane, M. Kavčič, J. Szlachetko, M. Szlachetko, and J. Hoszowska, Double K-shell photoionization of magnesium and aluminium, European Conference on X-Ray Spectrometry (EXRS-2006), Paris, France, July 19-23, 2006, book of abstr., **O1**-1: 4.

2) J. Hoszowska, J.-Cl. Dousse, M. Berset, W. Cao, K. Fennane, M. Kavčič, J. Szlachetko, and M. Szlachetko, Double 1s photoionization of Ca and V beyond maximum, European Conference on X-Ray Spectrometry EXRS-2006, Paris, France, July 19-23, 2006, book of abstr. **O1**-4: 7.

3) M. Kavčič, J.-Cl. Dousse, W. Cao, and J. Szlachetko, Chemical effects in the K x-ray emission of sulphur, European Conference on X-Ray Spectrometry EXRS-2006, Paris, France, July 19-23, 2006, book of abstr. **P1**-2: 114.

4) J. Szlachetko, J.-Cl. Dousse, J. Hoszowska, M. Kavčič, W. Cao, and M. Szlachetko, Relative detection efficiency of back- and front-illuminated CCD cameras for x-rays between 1 keV and 18 keV, 17th ESRF Users' Meeting, Feb. 7, 2007, ESRF, Grenoble, France.

5) M. Pajek, A. Kubala-Kukus, D. Banas, J.-Cl. Dousse, J. Hoszowska, J. Szlachetko, M. Szlachetko, and W. Cao, Application of grazing emission x-ray fluorescence for high-resolution detection of impurities in silicon, 12th Conference on Total Reflection X-Ray Fluorescence Analysis and Related Methods (TXRF 2007), June 18-22, 2007, Trento, Italy.

6) J. Hoszowska, J.-Cl. Dousse, M. Berset, W. Cao, K. Fennane, J. Szlachetko, and M. Szlachetko: Photon energy dependence of the ratio of double to single K-shell ionization for magnesium, aluminium and silicon, XXV International Conference on Photonic,

Electronic and Atomic Collisions (ICPEAC), July 25-31, 2007, Freiburg, Germany, book of abstr.: **We**-012.

7) A. Kubala-Kukus, M. Pajek, D. Banas, J.-Cl. Dousse, J. Hoszowska, J. Szlachetko, M. Szlachetko, and W. Cao, High-resolution grazing emission x-ray fluorescence studies of impurities in silicon, XXV International Conference on Photonic, Electronic and Atomic Collisions (ICPEAC), July 25-31, 2007, Freiburg, Germany, book of abstr.: **We**-048.

8) J. Szlachetko, M. Pajek, A. Kubala-Kukus, D. Banas, J.-Cl. Dousse, J. Hoszowska, M. Szlachetko, Y. Kayser, W. Cao, M. Kavčič, M. Salomé, and J. Susini, Application of high-resolution grazing emission x-ray fluorescence for material sciences, 18th ESRF Users' Meeting, Feb. 6, 2008, ESRF, Grenoble, France.

9) J. Hoszowska, J.-Cl. Dousse, M. Berset, W. Cao, K. Fennane, Y. Kayser, M. Kavčič, A. S. Kheifets, Y-P. Maillard, J. Szlachetko, and M. Szlachetko, Hollow magnesium, aluminium and silicon: photon energy dependence of double 1s ionization, Annual Meeting of the Swiss Physical Society, March 26-27, 2008, University of Geneva, booklet of abstr.: 88.

10) Y. Kayser, D. Banas, W. Cao, J.-Cl. Dousse, J. Hoszowska, A. Kubala-Kukus, M. Pajek, M. Salomé J. Susini, J. Szlachetko, and M. Szlachetko, Synchrotron radiation based high-resolution grazing emission x-ray fluorescence detection of Al-impurities on Si wafers, Annual Meeting of the Swiss Physical Society, March 26-27, 2008, University of Geneva, booklet of abstr.: 95.

11) W. Cao, M. Kavčič, K. Bucar, J.-Cl. Dousse, J. Hoszowska, Y. Kayser, A. Mihelic, J. Szlachetko and M. Zitnik, *L*-Shell Coster-Kronig coefficients of Palladium determined via high-resolution x-ray spectroscopy, International Workshop on Photoionization (IWP2008), June 15-19, 2008, Sätra Brunn/Uppsala, Sweden, book of abstr.

12) J. Hoszowska, M. Berset, W. Cao, J.-Cl. Dousse, K. Fennane, Y. Kayser, J.-L. Schenker, J. Szlachetko, M. Szlachetko and M. Kavčič, Double 1s ionization of Al and Si by photon and electron impact, European Conference on X-Ray Spectrometry (EXRS-2008), June 16-20, 2008, Cavtat/Dubrovnik, Croatia, booklet of abstr.: 93.

13) J. Szlachetko, M. Pajek, A. Kubala-Kukus, D. Banas, W. Cao, J.-Cl. Dousse, J. Hoszoska, M. Kavčič, Y. Kayser, M. Salomé, and J. Susini, Application of high-resolution

grazing emission x-ray fluorescence (GEXRF) spectroscopy for detection of low level impurities on Si-wafers, European Conference on X-Ray Spectrometry (EXRS-2008), June 16-20, 2008, Cavtat/Dubrovnik, Croatia, booklet of abstr.: 112.

14) Y. Kayser, J.-Cl. Dousse, J. Hoszowska, W. Cao, J.-L. Schenker, M. Pajek, A. Kubala-Kukus, P. Jagodzinski, M. Kavčič, and J. Szlachetko, Depth profiling of Al-implanted Si by means of synchrotron radiation based high resolution grazing emission x-ray fluorescence, European Conference on X-Ray Spectrometry (EXRS-2008), June 16-20, 2008, Cavtat/Dubrovnik, Croatia, booklet of abstr.: 268.

15) A. Kubala-Kukus, D. Banas, W. Cao, J.-Cl. Dousse, J. Hoszowska, Y. Kayser, M. Pajek, J. Szlachetko, M. Szlachetko; M. Salomé, and J. Susini, Application of high-resolution grazing emission x-ray fluorescence in material sciences, 9th International School and Symposium on Synchrotron Radiation in Natural Science (ISSRNS), June 15-20, 2008, Kielce, Poland. Synchr. Rad. Nat. Sci. **7**: L27 (2008).

16) J. Hoszowska, A. S. Kheifets, M. Berset, W. Cao, J.-Cl. Dousse, K. Fennane, M. Kavčič, Y. Kayser, J. Szlachetko and M. Szlachetko, Double K-shell photoionization of low-Z atoms and He-like ions, 21st International Conference on X-Ray and Inner-Shell Processes (X08), June 22-27, 2008, Paris, France, booklet of abstr.: 7.

17) M. Kavčič, M. Žitnik, K. Bučar, A. Mihelič, J. Szlachetko, and W. Cao, Near-thershold 1s2p and 1s3p double photoexcitation of Ar, 21st International Conference on X-Ray and Inner-Shell Processes (X08), June 22-27, 2008, Paris, France, booklet of abstr.: 130.

18) Y. Kayser, W. Cao, J.-Cl. Dousse, J. Hoszowska, , P. Jagodzinski, M. Kavčič, A. Kubala-Kukus, M. Pajek, P. Jagodzinski, J.-L. Schenker, J. Szlachetko, Characterization of Al-implanted Si wafers by using high resolution grazing emission x-ray fluorescence combined with synchrotron radiation, 19th ESRF Users' Meeting, Feb. 4, 2009, ESRF, Grenoble, France.

19) S. Nowak, Y. Kayser, L.T. Baczewski, D. Banas, W. Cao, J.-Cl. Dousse, J. Hoszowska, M. Pajek, A. Petroutchik, J. Szlachetko, and A. Wawro, SR-Based High-Resolution GEXRF Investigation of the Morphology of Surface Nanostructures. Hercules Specialized Courses

(HSC10), Synchrotron radiation techniques contribution to nanoscience, May 18-22, 2009, ESRF Grenoble, France.

20) Y. Kayser, W. Cao, J.-Cl. Dousse, J. Hoszowska, P. Jagodzinski, M. Kavčič, A. Kubala-Kukus, S. Nowak, M. Pajek, and J. Szlachetko, Depth profiles of Al impurities implanted in Si wafers determined by means of the high-resolution GEXRF technique, 13th Conference on Total Reflection X-Ray Fluorescence Analysis and Related Methods (TXRF 2009), June 15-19, 2009, Gothenburg, Sweden, booklet of abstr.: 12.

21) M. Pajek, D. Banas, W. Cao, J.-Cl. Dousse, J. Hoszowska, Y. Kayser, A. Kubala-Kukus, S. Nowak, J. Szlachetko, M. Salomé, and J. Susini, Synchrotron radiation based grazing emission x-ray fluorescence. 13th Conference on Total Reflection X-Ray Fluorescence Analysis and Related Methods (TXRF 2009), June 15-19, 2009, Gothenburg, Sweden, booklet of abstr.: 52.

22) S. Nowak, Y. Kayser, L.T. Baczewski, D. Banas, W. Cao, K. Deja, J.-Cl. Dousse, J. Hoszowska, M. Pajek, A. Petroutchik, J. Szlachetko, and A. Wawro, Investigation of the morphology of surface nanostructures by means of the synchrotron radiation based high-resolution GEXRF technique, XXXVIII International School and Conference on the Physics of Semiconductors Jaszowiec (ISCPS 2009), June 19-26, 2009, Krynica-Zdroj, Poland.

23) J. Hoszowska, A.K. Kheifets, J.-Cl. Dousse, M. Berset, J. Bray, W. Cao, K. Fennane, Y. Kayser, M. Kavčič, J. Szlachetko and M. Szlachetko, Double K-shell photoionization and universal scaling laws, XXVI International Conference on Photonic, Electronic and Atomic Collisions (ICPEAC), July 22-28, 2009, Kalamazoo, USA.

24) M. Pajek, D. Banas, W. Cao, J.-Cl. Dousse, J. Hoszowska, Y. Kayser, A. Kubala-Kukus, S. Nowak, J. Szlachetko, M. Salomé, and J. Susini, Synchrotron-radiation based high-resolution grazing emission x-ray fluorescence - Applications in nanoscience, 11th International Symposium on Radiation Physics (ISRP-11), Sept. 21-27, 2009, Melbourne, Australia.

25) M. Pajek, D. Banas, W. Cao, J.-Cl. Dousse, J. Hoszowska, Y. Kayser, A. Kubala-Kukus, S. Nowak, J. Szlachetko, M. Salomé, and J. Susini, Synchrotron radiation based grazing

emission x-ray fluorescence, 11th International Symposium on Radiation Physics (ISRP-11), Sept. 21-27, 2009, Melbourne, Australia.

26) S. Nowak, Y. Kayser, L. T. Baczewski, D. Banas, W. Cao, J.-Cl. Dousse, J. Hoszowska, M. Pajek, A. Petroutchik, J. Szlachetko, and A. Wawro, The synchrotron radiation based high-resolution grazing x-ray emission zechnique for surface morphology analysis, HERCULES XX Workshop, March 25-26, 2010, Grenoble, France.

27) Y. Kayser, D. Banas, W. Cao, J.-Cl. Dousse, J. Hoszowska, P. Jagodzinski, M. Kavčič, A. Kubala-Kukus, S. Nowak, M. Pajek, and J. Szlachetko, SR-based high-resolution GEXRF, a new technique to determine the depth distribution of dopants implanted in semiconductors, European Conference on X-Ray Spectrometry (EXRS2010), June 20-25, 2010, Figueira da Foz, Coimbra, Portugal.

28) S. Nowak, D. Banas, W. Cao, J.-Cl. Dousse, J. Hoszowska, Y. Kayser, A. Kubala-Kukus, M. Pajek and J. Szlachetko, Synchrotron radiation based high-resolution grazing emission x-ray fluorescence: a multipurpose surface characterization method, XXXIX International School and Conference on the Physics of Semiconductors Jaszowiec (ISCPS 2010), June 21-24, 2010, Krynica-Zdroj, Poland.

29) S. Nowak, Y. Kayser, L. T. Baczewski, D. Banas, W. Cao, K. Deja, J.-Cl. Dousse, J. Hoszowska, M. Pajek, A. Petroutchik, J. Szlachetko, and A. Wawro, Analysis of surface nanostructures via the SR-based high-resolution GEXRF technique, 10th European Conference on Atoms, Molecules and Photons (ECAMP 10), July 4-9, 2010, Salamanca, Spain.

30) J. Hoszowska, J.-Cl. Dousse, J. Szlachetko, W. Cao, P. Jagodzinski, Y. Kayser, S. Nowak, and M. Kavčič, First observation of two-electron one-photon transitions in single-photon impact, 37th International Conference on Vacuum UltraViolet and X-Ray Physics, July 11-16, 2010, Vancouver, Canada.

31) J. Hoszowska, W. Cao, J.-Cl. Dousse, K. Fennane, Y. Kayser, M. Kavčič, J. Szlachetko, and M. Szlachetko, Photoinduced K hypersatellite x-ray emission for $12 \leq Z \leq 23$ elements, 37th International Conference on Vacuum UltraViolet and X-Ray Physics, July 11-16, 2010, Vancouver, Canada.

32) Y. Kayser, D. Banas, W. Cao, J.-Cl. Dousse, J. Hoszowska, P. Jagodzinski, M. Kavčič, A. Kubala-Kukus, S. Nowak, M. Pajek, and J. Szlachetko, Depth profiling of dopants implanted in Si using the SR-based high-resolution grazing emission technique, 17th International Conference on Ion Beam Modification of Materials (IBMM 2010), August 21-27, 2010, Montréal, Canada.

33) J. Hoszowska, J.-Cl. Dousse, J. Szlachetko, W. Cao, P. Jagodzinski, Y. Kayser, S. Nowak, and M. Kavčič, Photon induced two-electron one-photon transitions 7th International Conference on Inelastic X-Ray Scattering (IXS 2010), Oct. 11-14, 2010, Grenoble, France.

III. OTHER NON-REFEREED ARTICLES

1) M. Kavčič, M. Žitnik, K. Bučar, A. Mihelič, M. Štuhec, J. Szlachetko, W. Cao, R. Alonso Mori, and P. Glatzel, Two-electron atomic processes induced with a single photon, ESRF Highlights: 16 (2009).

2) J. Hoszowska, A. K. Kheifets, J.-Cl. Dousse, M. Berset, I. Bray, W. Cao, K. Fennane, Y. Kayser, M. Kavčič, J. Szlachetko, and M. Szlachetko, Physical mechanisms and scaling laws of K-shell double photoionization, ESRF Highlights: 80 (2009).

3) W. Cao, Les traditions, piliers d'un monde en pleine mutation, Universitas, Le magazine de l'Université de Fribourg, Suisse, No. 4, Juin (2010).

IV. ARTICLES IN PROGRESS

1) W. Cao, J.-Cl. Dousse, J. Hoszowska, M. Kavčič, Y. Kayser, J.-L. Schenker, and M. Žitnik, Double L_3M ionization of Pd induced by impact with medium-energy electrons, submitted to Phys. Rev. A.

2) J. Hoszowska, J.-Cl. Dousse, W. Cao, K. Fennane, Y. Kayser, M. Szlachetko, J. Szlachetko and M. Kavčič, Double K-shell photoionization and hypersatellite x-ray transitions of $12 \leq Z \leq 23$ atoms, submitted to Phys. Rev. A.

3) Y Kayser, D. Banaś, W. Cao, J.-Cl. Dousse, J. Hoszowska, P. Jagodziński, M. Kavčič, A. Kubala-Kukuś, S. Nowak, M. Pajek M, and J. Szlachetko, Depth profiling of dopants

implanted in Si using the SR based high-resolution grazing emission technique, submitted to Nucl. Instrum. Methods Phys. Res. B.